FACULTY OF ENGINEERING AND ARCHITECTURE

Performance analysis of heat pumps in Carnot battery systems for grid balancing services

Jari De Craecker
Student number: 01700030

Supervisors: Prof. dr. ir. Steven Lecompte, Prof. dr. ir. Michel De Paepe
Counsellors: Ir. Robin Tassenoy, Dr. ir. Toon Demeester, Katarina Simic

Master's dissertation submitted in order to obtain the academic degree of
Master of Science in Electromechanical Engineering

Academic year 2021-2022

GHENT UNIVERSITY

Ghent, June 2022
Jari De Craecker

Preface

This master thesis marks the end of a five year long adventure. A great deal of thought, time and effort went into this work and it would not have been possible without the help and support of several people.

First, I would like to thank my supervisors Prof. dr. ir. Steven Lecompte and Prof. dr. ir. Michel De Paepe for offering me the opportunity to work on this subject and for all the useful feedback and advice.

My sincere gratitude also goes out to my counsellors ir. Robin Tassenoy, dr. ir. Toon Demeester and ir. Katarina Simic. Their insights, advice, feedback and continuous availability were of key importance in accomplishing this work.

Also special thanks to Hannes for the interesting discussions and the support. This cooperation definitely contributed to the work.

Furthermore, I would also like to thank all my friends for their kind words and support. It would be impossible to list everyone who contributed to this, but a special mention goes to François, Aaron, Thibaut, Victor and Laurent and everyone who was there for me in any way.

Last but definitely not least, I would like to thank my parents for their patience and constant support.

Performance analysis of heat pumps in Carnot battery systems for grid balancing services

Jari De Craecker

Supervisors: Prof. dr. ir. Steven Lecompte, Prof. dr. ir. Michel De Paepe
Counsellors: Ir. Robin Tassenoy, Dr. ir. Toon Demeester, ir. Katarina Simic

Master's dissertation submitted in order to obtain the academic degree of
Master of Science in Electromechanical Engineering

Departement of Electromechanical, Systems and Metal Engineering
Faculty of Engineering and Architecture
Ghent University
Academic year 2022–2023

Abstract

The growth of renewable energy requires flexible, low-cost and efficient electrical storage to balance the mismatch between energy supply and demand. The Carnot battery buffers electrical energy by storing thermal energy from a resistive heater or a heat pump system when the electricity production is higher than demand. When electricity demand is higher than the production, the Carnot battery generates power from the stored thermal energy. These heat pumps are also expected to support the power grid by providing balancing services.

This study aims to assess the performance of heat pumps in Carnot battery systems for grid balancing services. For this purpose, a dynamic model of a high-temperature heat pump with a variable speed compressor was implemented in Dymola.

The results showed that the system allowed sufficiently fast regulation of the compressor power to provide primary (FCR), secondary (aFRR) and even tertiary control reserve (mFRR). However, the capacity of the current model is still too low, so further up-scaling or the combination of multiple systems is required to provide the needed bid volumes.

Keywords
Carnot battery, heat pump, grid balancing, transient behaviour, dynamic model

MASTER THESIS 2021-2022
Research group Sustainable Thermo-Fluid Energy Systems
Department of Electromechanical, Systems and Metal Engineering – Ghent University, UGent

PERFORMANCE ANALYSIS OF HEAT PUMPS IN CARNOT BATTERY SYSTEMS FOR GRID BALANCING SERVICES

Jari De Craecker, Steven Lecompte, Michel De Paepe Robin Tassenoy, Toon Demeester, ir. Katarina Simic
Department of Electromechanical, Systems and Metal Engineering
Ghent University
Sint-Pietersnieuwstraat 41, B9000 Gent, Belgium
E-mail: jari.decraecker@ugent.be

I. Abstract

The growth of renewable energy requires flexible, low-cost and efficient electrical storage to balance the mismatch between energy supply and demand. The Carnot battery buffers electrical energy by storing thermal energy from a resistive heater or a heat pump system when the electricity production is higher than demand. When electricity demand is higher than the production, the Carnot battery generates power from the stored thermal energy. These heat pumps are also expected to support the power grid by providing balancing services.

This study aims to assess the performance of heat pumps in Carnot battery systems for grid balancing services. For this purpose, a dynamic model of a high-temperature heat pump with a variable speed compressor was implemented in Dymola.

The results showed that the system allowed sufficiently fast regulation of the compressor power to provide primary (FCR), secondary (aFRR) and even tertiary control reserve (mFRR). However, the capacity of the current model is still too low, so further up-scaling or the combination of multiple systems is required to provide the needed bid volumes.

II. Introduction

The power generation sector is projected to undergo profound restructuring toward the dominance of renewable energy (e.g., solar, wind, and biomass) [1]. However, due to the variations in weather, season and location, renewable energy is unstable and discontinuous. The integration of these variable renewable energy sources into the grid will increase the imbalance between production and consumption [2], [3].

For this reason, the need for flexibility in the power system grows. This flexibility in the grid can be achieved in four different ways, namely dispatchable power plants, demand-side management, connections with adjacent markets and electricity storage [4].

In this research, the focus is placed on the implementation of electricity storage systems. Electricity storage has two primary functions: levelling the demand curve and ensuring power quality and reliability by providing ancillary services. For load levelling, the electricity storage is used to level the load over various timescales, thereby reducing the peak/off-peak amplitude. Ancillary services on the other hand try to maintain the system's frequency and voltage within technical limits to avoid instability and blackouts. This could be achieved by using fast-response electricity storage to inject or withdraw power as an alternative to conventional reserves

NOMENCLATURE

Acronyms

aFRR	Automatic frequency restoration reserve
CAES	Compressed air energy storage
CB	Carnot battery
CSP	Concentrated solar power
FBES	Flow battery energy storage
FCR	Frequency containment reserve
GWP	Global warming potential
HE	Heat engine
HP	Heat pump
mFRR	Manual frequency restoration reserve
ODP	Ozone depletion potential
PHE	Plate heat exchanger
PHS	Pumped hydro storage
PTES	Pumped thermal energy storage
TES	Thermal energy storage

Symbols

a	[mm]	amplitude
t	[mm]	Plate thickness
T	[°C]	Temperature

Greek symbols

λ	[m]	Wavelength
ϕ	[°]	Pattern angle

Subscripts

meas	measured

[4].

Currently, the world energy storage capacity is dominated by Pumped Hydro Storage (PHS) [5], [6]. Examples of other technologies are compressed air energy storage (CAES), NaS battery energy storage system (BESS), molten salt thermal energy storage (TES), flow battery energy storage (FBES)... [7].

Thermal energy storage (TES) can be an interesting technology. It already exists in a wide spectrum of applications and uses materials that can be kept at high/low temperatures in insulated containers. Heat/cold can then be applied for electricity generation using heat engine cycles. Energy input can, in principle, be provided by electrical resistance heating or refrigeration/cryogenic procedures [8].

A. Carnot batteries

In the light of geographical independence and scalability, Carnot batteries (CB) can be a promising technology [9]. A Carnot battery is based on heat pumps (HP) or resistive heaters, which transform off-peak electricity into thermal energy. Next, the energy is stored inside man-made thermally isolated vessels [10]. During delivery, a heat engine (HE) is adopted to convert the stored thermal energy back into electrical energy [11]. If the heating is provided by a heat pump, this system is also called pumped thermal energy storage (PTES).

Hence, PTES consists of three main components: a HP, a TES and a HE. Several different types of HP, TES and HE are available and have to be selected depending on the intended operating conditions. Some of the most common implementations are the Brayton based and the Rankine-based PTES.

PTES finds wide applications in load levelling and electricity production by heat engines [4]. Hossain et al. [7] analysed and compared literature about the suitability of storage technologies for certain grid supporting services. Several studies showed a good match for PTES with load levelling applications like generation capacity reserves and transportation & distribution peak shaving. However, little to no studies were available where PTES was evaluated for the application in ancillary services. As mentioned before, these services ensure power quality and reliability and have time constants in the order of seconds or minutes [12].

B. Scope of this study

The aim of this study is to quantify the dynamic behaviour of a large scale heat pump and the limitations with regard to fast ramping. In particular, focus is laid on large-scale heat pumps, based on a subcritical Rankine cycle. A dynamic model is constructed, which allows evaluating the potential of such a system to deliver balancing services for the electricity grid.

III. Model development

A dynamic model of the heat pump was built in the object-oriented modelling language Modelica. It was implemented in the simulation software Dymola using the TIL library [13]. The model was based on component models of a compressor, an evaporator, a condenser and an expansion valve. Furthermore, the heat pump control was included. The fluid properties were calculated using the Refprop database [14]. In the following sections, the models of the separate components are presented, as well as the assumptions that are taken. A block diagram of the system is represented in Figure 1.

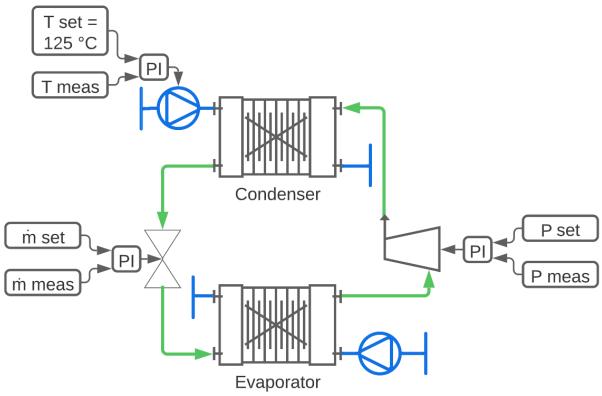

Fig. 1: Complete cycle

A. Operating conditions

For the selection of a refrigerant, first, the nominal operating conditions have to be determined. This consists of the supply and return temperatures of the heat source and heat sink, the mass flow rates, the intended power... A python script, available on Github [15], calculates basic thermodynamic cycles, taking into account these boundary conditions. The proposed values are summarized in Table I.

Based on these operating conditions the most suitable refrigerant R-1233zd(E) was selected. Furthermore, it is future proof, since it has a lower global warming potential (GWP) and ozone depletion potential (ODP) than the most implemented refrigerants currently [16].

TABLE I: Nominal operating conditions: input parameters

$T_{water,source,in}$ [°C]	65
$T_{water,sink,in}$ [°C]	95
T_{evap} [°C]	50
T_{cond} [°C]	130
ΔT_{SH} [°C]	9
ΔT_{SC} [°C]	4
Q_{cond} [MW]	2.8
ΔT_{evap} [°C]	5
ΔT_{cond} [°C]	5
η_s	0.8
Refrigerant	R-1233zd(E)

The system was sized to attain an electric compressor power in the order of magnitude of 1 MW. The pinch

point temperature of the evaporator and the condenser were both assumed to be 5K. Next, the amount of subcooling in the condenser was fixed to 4 °C, whereas the superheat in the evaporator was fixed to 9 °C in order to leave a sufficient margin for condensation.

Figure 2, shows the Ts-diagram of the calculated cycle. The blue and red lines represent the water temperatures in the heat exchangers and the green line represents the states of the refrigerant.

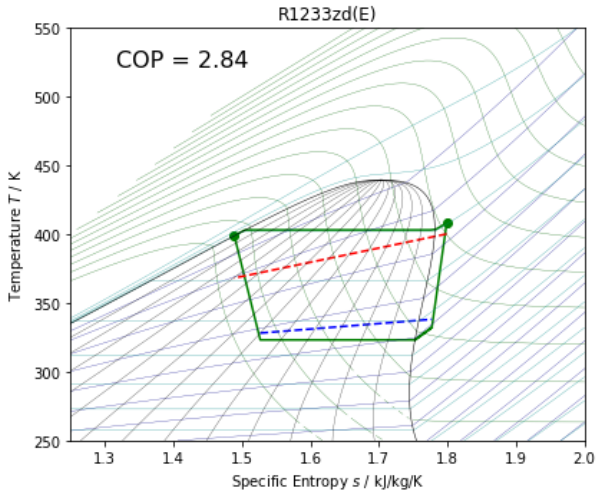

Fig. 2: Ts-diagram of the cycle in nominal operating conditions

The script calculates the pressures in the evaporator and condenser, the pressure ratio, the COP, the mass flow rates, the heat flows and the electrical power of the compressor. These values are presented in Table II and are later on used as a base for sizing the system components.

TABLE II: Nominal operating conditions

p_{low} [bar]	2.93
p_{high} [bar]	19.08
PR [-]	6.5
$\rho_{ref,comp,in}$ [kg/m³]	15.1
COP [-]	2.84
$\dot{m}_{water,source}$ [kg/s]	43.4
$\dot{m}_{water,sink}$ [kg/s]	20.7
$\dot{m}_{refr}$ [kg/s]	22.4
Q_{evap} [kW]	1814
Q_{cond} [kW]	2800
$P_{el,comp}$ [kW]	986

B. Component selection and modelling

1) Heat exchanger

For the condenser and the evaporator plate heat exchangers (PHE) are selected. The sizing was based on the SSPG8 software provided by SWEP [17]. The proposed heat exchangers are presented in Tables III and IV.

TABLE III: Evaporator sizing from SWEP software

Type	VH500TM
Area [m²]	454
Number of plates	5 · 306 = 1530
Total weight [kg]	1639
Hold-up volume (refr) [l]	87
Hold-up volume (water) [l]	87

TABLE IV: Condenser sizing from SWEP software

Type	B500TM
Area [m^2]	149
Number of plates	2 · 252 = 504
Total weight [kg]	488
Hold-up volume (refr) [l]	72
Hold up volume (water) [l]	72

In the evaporator, the following geometric parameters were selected: $\phi = 60°$, $t = 0.45$ mm, $a = 1.1$ mm and $\lambda = 8.8$ mm. The condenser used: $\phi = 30°$, $t = 0.41$ mm, $a = 1.1$ mm and $\lambda = 8.8$ mm [18], [19].

A finite volume approach was used for the heat exchangers and a quadratic mass flow dependence of the pressure drop was selected. For the heat transfer correlations: TIL [13] proposed the VDI Plate Alpha [20] on the water side, whereas on the refrigerant side the correlations by Shah Chen and Gnielinski Dittus Boelter are implemented [21]–[24].

2) Compressor

Considering the flow rate and the pressure ratio a screw compressor or a centrifugal compressor would be selected [25]. However, the available data for compressor characteristics was limited. A compressor map of an axial compressor was retrieved from GasTurb map collection [26] and was scaled to the correct operating conditions.

A quasi-steady-state model was constructed for the axial compressor, based on a volumetric compressor model in the TIL library [13]. It takes the compressor characteristics: mass flow rate and isentropic efficiency as a function of the pressure ratio for different rotational speeds.

3) Other components

Also, a valve model is included in the TIL library [13]. It calculates the mass flow rate using Equation 1

$$m_{flow} = A_{eff} \cdot \sqrt{(p_{input} - p_{output}) \cdot 2 \cdot \rho_{input}} \quad (1)$$

Finally, the connections with the thermal storage tank are represented by boundaries, where the temperature, mass flow rate and pressure can be specified.

4) Controls

The model is equipped with 3 controls. The first one is direct control of the compressor power since the compressor power has to react as quickly as possible in order to deliver balancing services to the grid. The second controller influences the through-flow area of the

valve. It measures the pressure ratio over the compressor and adapts the valve through-flow area accordingly to maximize the compressor efficiency. Finally, also the temperature of the water has to be maintained at a temperature close to 125 °C. This is indirectly established by adapting the water mass flow through the condenser. The values of the gain and the integration time constants are stated in Table V

TABLE V: Parameters of PI-controls

	k [-]	T_i [s]
Control of compressor power	8E-06	10
Control of expansion valve	8E-06	4
Control of water mass flow rate	5	7

C. Model calibration and validation

Literature suggests that the dynamic behaviour of heat pumps is dominated by heat exchangers. Hence, the inertia and the heat transfer coefficients in the heat exchangers are studied. The inertia and the heat transfer coefficients between the water and the wall showed satisfactory correspondence to literature. The heat transfer coefficient between the refrigerant and the wall, however, is lower than expected.

D. Steady-state behaviour

The steady-state operating conditions of the model are presented in Figure 3. These correspond quite well to the intended operating conditions proposed in the model development. The steady-state operation achieves a COP of 2.64.

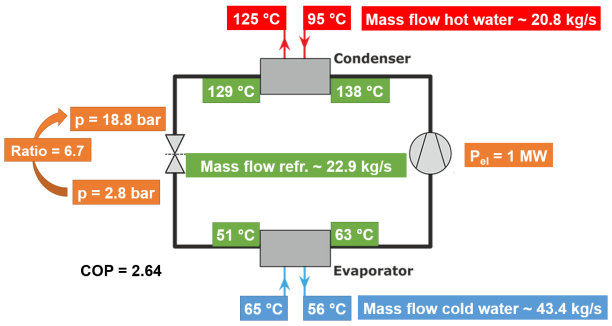

Fig. 3: Overview of steady-state operating conditions

E. Simulation approach

Once the complete cycle is modelled, the test profiles of transmission grid operators are imposed to verify if the system can be qualified as a primary (FCR), secondary (aFRR) or tertiary control reserve (mFRR). The frequency containment reserve (FCR) must be able to reach the required power within 30 s if necessary. Automatic frequency restoration reserve (aFRR) must be fully activated within 5 minutes and after activation, the system operator sends a new setpoint every 4 s. Manual frequency restoration reserve (mFRR) must be fully activated within 15 minutes [27]–[29].

For this research, the steady-state conditions are on the nominal compressor power of 1 MW. Up-regulation is provided by consuming less energy in the compressor. The capacity is defined by the difference between the nominal power and the lowest possible. For aFRR as well as mFRR a system can qualify for upward and/or downward regulation [27], [28]. However, the frequency containment reserve (FCR) is a symmetric product, meaning that upward and downward capacity are procured together [29]. This study focuses on the upward part of the regulation.

The maximum capacity is observed as 25 % of the nominal electric compressor power. Hence, the electric compressor power can decrease from 1 MW down to 750 kW. The main factor limiting the capacity is the operating curve of the compressor. Since it is controlled along its maximal efficiency line, decreasing power will also result in a decreasing pressure ratio and condenser temperature. As a consequence, the required water outlet temperature of 125 °C is not reached for compressor powers lower than 750 kW.

The minimum bid volume for the aFRR and mFRR is 1 MW, however, this capacity can also be provided by a pool of 'delivery points'.

IV. Results

A. Dynamic behaviour

In Figure 4 the results are shown of the prequalification test for the automatic frequency restoration reserve. The set compressor power can be followed with great accuracy by the direct control of the compressor.

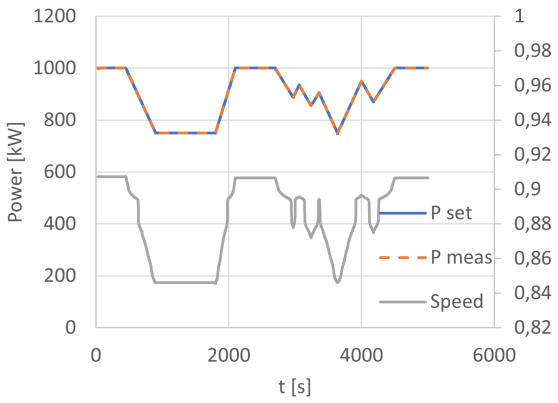

Fig. 4: Results of the prequalification test for automatic frequency restoration reserve (aFRR), it shows the set and measured compressor power ($P\ set$, $P\ meas$) and the normalized speed as a function of time

No significant issues were encountered for the aFRR, so also the prequalification profile for the frequency containment reserve was tested. The results are represented in Figure 6. The set compressor power profile decreases its power in 4 steps to the minimum

power, each taking a period of 8 s. Also here the profile is perfectly followed and the system is able to provide the up-regulation for the FCR.

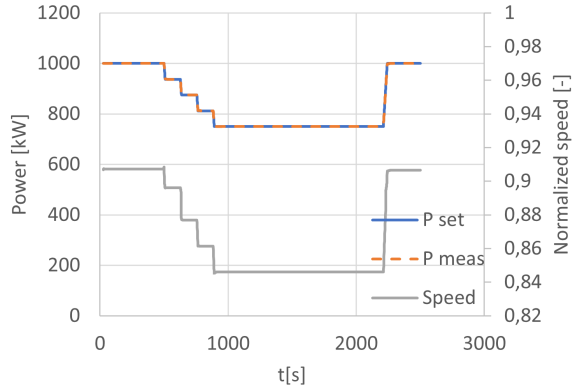

Fig. 5: Results of the prequalification test for the frequency containment reserve (FCR), it shows the set and measured compressor power ($P\ set$, $P\ meas$) and the normalized speed as a function of time

Besides following the compressor power, the heat pump is still required to deliver water to the thermal energy storage at 125 °C. Hence, the measured water outlet temperature in the heat sink is plotted together with the mass flow rate controlled by the PI controller of the water pump.

It clearly illustrates the decrease in mass flow rate during the period with a reduced compressor power in order to maintain the desired output temperature. For the imposed profile, the deviation of the set temperature remains $< \mp 0.3$ °C. The deviation decreases with a decreasing ramp rate of the compressor power.

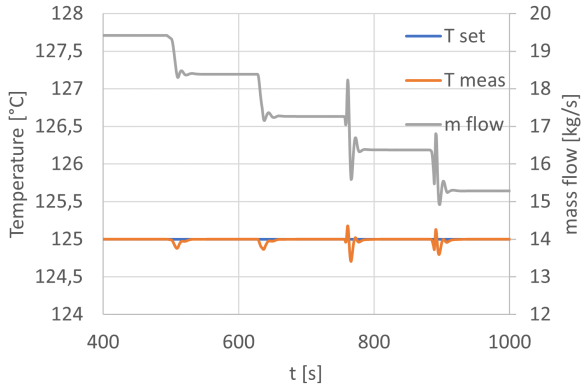

Fig. 6: Detailed view of the evolution of the set and measured water outlet temperature of the sink ($T\ set$, $T\ meas$), as well as the controlled mass flow rate of the water ($m\ flow$) as a function of time, for the frequency containment reserve

Finally, the evolution of the pressure is represented in Figure 7. It clearly represents the decreasing compression ratio for the decreasing compressor power. Also, the pressure follows neatly the system and no strong pressure overshoots.

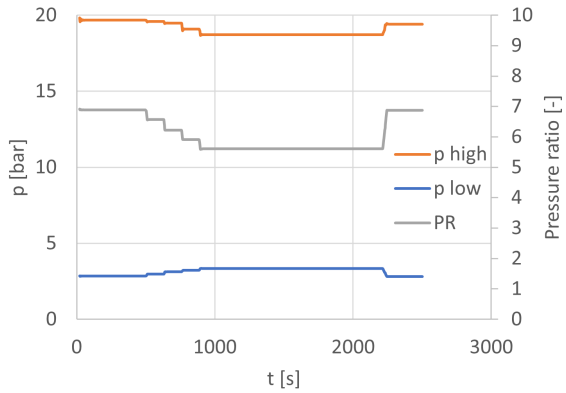

Fig. 7: The evolution of the condenser pressure ($p\ high$), the evaporator pressure, ($p\ low$) and the pressure ratio (PR) as a function of time, for the frequency containment reserve test

V. Conclusion

A. Conclusion

In this work, the transient behaviour and dynamic modelling of a high-temperature heat pump in a Carnot battery are studied. A dynamic heat pump model is developed in Dymola to achieve these objectives. A finite volume approach is used to model the plate heat exchangers in a dynamic way. The pumps and compressors on the other hand are modelled as quasi-steady-state components. Finally, a control structure was added to control the system in varying operating conditions.

First, the inertia and the heat transfer in the heat exchangers are studied, since literature suggests that the heat exchangers dominate the dynamic behaviour of heat pumps.

Furthermore, the maximum capacity of 250 kW is limited by the decreasing condenser temperature in part-load operation. As a consequence, the required outlet temperature of 125 °C is not reached for compressor powers lower than 750 kW.

Another point of attention is the risk of condensation in the suction line of the compressor during fast load transients. However, because of the counter-flow heat exchanger and the fact that the evaporator output is always superheated, no condensation is expected.

Next, a sensitivity analysis was performed on the proportional constants of the PI controller of the compressor and the heat sink water pump. Decreasing the proportional constant of the water pump increased

the deviations in the water outlet temperature. For the compressor, the main influence was the prolonged reaction time, decreasing the capabilities of accurately following an imposed compressor power profile.

Finally, the main objective of this work was studied, namely the performance of the heat pump for grid balancing services. To study the response of the system, prequalification profiles for different balancing services were imposed on the model. Literature suggests that heat exchangers typically have larger time constants compared to the other components in a heat pump. The experiments, however, showed that the inertia of the heat exchangers was rather low. The results even suggest that transients of the compressor power in the order of seconds are possible with this model. This gives confidence for the potential application of similar systems in balancing services. However, it also raises the question if the suggestion of literature to model the compressors and pumps as quasi-steady-state components is still valid.

The results of the test showed that such heat pumps show great potential for delivering mFRR, aFRR and even FCR. However, important to mention is that only up-regulation has been evaluated and the current capacity is also limited to 250 kW. For actual applications the model needs up-scaling to even higher powers.

B. Future research

Related to the dynamic modelling of heat pumps for balancing services, there are still some aspects which can be topics for further research.

A first point is to implement dynamic models of the compressor and the pumps, which include the inertia of the components and thus the maximum acceleration and deceleration rate. Also, the addition of the compressor's thermal inertia is interesting, to further study the risk of condensation on the compressor suction line and walls.

A second proposal is the implementation of a volumetric compressor since they are able to maintain high pressure ratios, also for lower compressor powers.

Another interesting topic to study is the dynamic interaction of the heat pump and the thermal energy storage, or even the interaction of all three components: heat pump, thermal energy storage and organic Rankine cycle. Moreover, a control strategy can be developed, optimizing the complete system for providing balancing services.

REFERENCES

[1] P. Capros, M. Kannavou, S. Evangelopoulou, A. Petropoulos, P. Siskos, N. Tasios, G. Zazias, and A. DeVita, "Outlook of the EU energy system up to 2050: The case of scenarios prepared for European Commission's "clean energy for all Europeans" package using the PRIMES model," *Energy Strategy Reviews*, vol. 22, pp. 255–263, nov 2018.

[2] C. Chang, Z. Wu, H. Navarro, C. Li, G. Leng, X. Li, M. Yang, Z. Wang, and Y. Ding, "Comparative study of the transient natural convection in an underground water pit thermal storage," *Applied Energy*, vol. 208, pp. 1162–1173, dec 2017.

[3] Y. Deng, D. Sun, M. Niu, B. Yu, and R. Bian, "Performance assessment of a novel diffuser for stratified thermal energy storage tanks – The nonequal-diameter radial diffuser," 2021.

[4] SBC Energy institute, "Electricity Storage," *Lecture Notes in Energy*, vol. 3, no. September, pp. 307–333, 2013.

[5] P. Medina, A. W. Bizuayehu, J. P. Catalão, E. M. Rodrigues, and J. Contreras, "Electrical energy storage systems: Technologies' state-of-the-art, techno-economic benefits and applications analysis," *Proceedings of the Annual Hawaii International Conference on System Sciences*, pp. 2295–2304, 2014.

[6] International Renewable Energy Agency, *Electricity storage and renewables: Costs and markets to 2030*. No. October, 2017.

[7] E. Hossain, H. M. R. Faruque, M. S. H. Sunny, N. Mohammad, and N. Nawar, "A comprehensive review on energy storage systems: Types, comparison, current scenario, applications, barriers, and potential solutions, policies, and future prospects," *Energies*, vol. 13, no. 14, pp. 1–127, 2020.

[8] H. Chen, T. N. Cong, W. Yang, C. Tan, Y. Li, and Y. Ding, "Progress in electrical energy storage system: A critical review," *Progress in Natural Science*, vol. 19, no. 3, pp. 291–312, 2009.

[9] M. Morandin, F. Maréchal, M. Mercangöz, and F. Buchter, "Conceptual design of a thermo-electrical energy storage system based on heat integration of thermodynamic cycles - Part A: Methodology and base case," *Energy*, vol. 45, no. 1, pp. 375–385, 2012.

[10] A. Benato, "Performance and cost evaluation of an innovative Pumped Thermal Electricity Storage power system," *Energy*, vol. 138, pp. 419–436, 2017.

[11] A. Benato and A. Stoppato, "Pumped Thermal Electricity Storage: A technology overview," *Thermal Science and Engineering Progress*, vol. 6, pp. 301–315, 2018.

[12] "Balancing Services: Definition, Background & why we need it." https://www.next-kraftwerke.com/knowledge/balancing-services.

[13] "Thermodynamic simulation with TIL I TLK Energy." https://tlk-energy.de/en/software/til-suite.

[14] "About REFPROP — REFPROP 10.0 documentation." https://refprop-docs.readthedocs.io/en/latest/GUI/GeneralInformation/aboutrefprop.html.

[15] "GitHub - squoilin/NextGenerationHeatPumps: Python toolbox to model advanced heat pump concepts (high temperature heat pumps, zeotropic, transcritical, ...)." https://github.com/squoilin/NextGenerationHeatPumps.

[16] A. Hassan, J.-M. Corberán, and V. Sanchez, "Detailed Design of the High Temperature Heat Pump Laboratory Prototype (CHESTER, D3.2)," no. 27, 2019.

[17] "Products - SWEP." https://www.swep.net/products/.

[18] "Alfa Laval - heat transfer, separation, fluid handling." https://www.alfalaval.com/.

[19] W. Meesenburg, W. B. Markussen, T. Ommen, and B. Elmegaard, "Optimizing control of two-stage ammonia heat pump for fast regulation of power uptake," *Applied Energy*, vol. 271, no. December 2019, p. 115126, 2020.

[20] M. Kind and H. Martin, *Verein Deutscher Ingenieure (VDI) - Heat Atlas*. 2010.

[21] M. M. Shah, "A general correlation for heat transfer during film condensation inside pipes," *International Journal of Heat and Mass Transfer*, vol. 22, no. 4, pp. 547–556, 1979.

[22] K. Baehr H.D., Stephan, "Wärme- und Stoffübertragung," 1996.

[23] J. C. Chen, "Correlation for boiling heat transfer to saturated fluids in convective flow," *Industrial and Engineering Chemistry Process Design and Development*, vol. 5, no. 3, pp. 322–329, 1966.

[24] C. C. Richter, "Proposal of New Object-Oriented Equation-Based Model Libraries for Thermodynamic Systems. PhD Thesis.," *PhD Thesis*, pp. 1–157, 2008.

[25] K. Hoopes, T. C. Allison, and R. Kurz, "Oil and gas compressor basics," *Compression Machinery for Oil and Gas*, pp. 3–11, jan 2018.

[26] "GasTurb - Download." https://www.gasturb.com/download.html.

[27] "aFRR." https://www.elia.be/nl/elektriciteitsmarkt-en-systeem/systeemdiensten/het-evenwicht-behouden/afrr.

[28] "mFRR." https://www.elia.be/nl/elektriciteitsmarkt-en-systeem/systeemdiensten/het-evenwicht-behouden/mfrr.

[29] "Frequency Containment Reserves (FCR)." https://www.entsoe.eu/network_codes/eb/fcr/.

Contents

List of Figures

List of Tables

Nomenclature

Acronyms

aFRR	Automatic frequency restoration reserve
BESS	Battery energy storage system
BSP	Balancing service provider
CAES	Compressed air energy storage
CAPEX	Capital expenditures
CB	Carnot battery
CCS	Carbon capture and storage
CHEST	Compressed heat energy storage
COP	Coefficient of performance
CSP	Concentrated solar power
ENTSO-E	European Network of Transmission System Operators for Electricity
FBES	Flow battery energy storage
FCR	Frequency containment reserve
FCR	Fequency containment reserve
GCI	Grid convergence index
GWP	Global warming potential
HE	Heat engine
HP	Heat pump
HS	High stage
HT	High temperature
LCOE	Levelised cost of energy
LCOS	Levelised cost of storage
LS	Low stage
LT	Low temperature
mFRR	Manual frequency restoration reserve
Mtoe	Megatons of oil equivalent
NBP	Normal boiling point
ODP	Ozone depletion potential
ORC	Organic Rankine cycle
PCM	Phase change materials
PHE	Plate heat exchanger
PHES	Pumped heat energy storage
PHS	Pumped hydro storage
PTES	Pumped thermal energy storage
RES	Renewable energy storage
SH	Superheat
STHE	Shell and tube heat exchanger
TES	Thermal energy storage
TI	Thermal integration
TSO	Transmission system operator
VHC	Volumetric heating capacity
VRF	Vanadium redox flow

Symbols

a	mm	amplitude
A	m^2	Area
BO	-	Boiling coefficient
C	J/K	Heat capacity
D	-	Dry
d	mm	Diameter
E	J	Energy
effIsEff	-	Effective isentropic efficiency
Fr	-	Froude
g	N/kg	Gravitational constant
h	J/kg	Specific enthalpy
isEFF	-	Isentropic efficiency
k	-	Gain of PI controller
L	-	Length
m	kg/s	Mass flow rate
m	kg	Mass
n	rpm	Rotational speed
Nu	-	Nusselt number
p	Pa	Pressure
PR	-	Prandtl
PR	-	Pressure ratio
q	W	Heat transfer
Q	J	Heat
Re	-	Reynolds
r	-	Grid refinement ratio
s	J/K	Entropy
S	-	isentropic
t	mm	Plate thickness
T	°C	Temperature
T_i	s	Integrator time constant
V	m^3	Volume
volEFF	-	Volumetric efficiency
W	-	Wet
w_a	W/K	Thermal capacity rate
z	-	Dimensionless time

Greek symbols

α	W/(m^2K)	Heat transfer coefficient
Δ	-	Difference
η	-	Efficiency
λ	m, W/(mK)	Wavelength, thermal conductivity
ϕ	°	Pattern angle
ρ	kg/m^3	Density

Subscripts

c	cold
comp	compressor
cond	condensation, condensor
crit	critical
disp	displacement
eff	effective
el	electric
evap	evaporation, evaporator
exp	expansion valve
ext	external
h	hot
hydr	hydraulic
in	inlet
meas	measured
out	outlet
refr	refrigerant
rt	round trip
sat	saturation
st	storage
th	thermal

Chapter 1

Introduction

1.1 Context

The world's energy consumption has risen to a level never reached before, releasing in the same process large quantities of CO_2 into the atmosphere. In 2019 the world's energy consumption was approximately 14 000 Mtoe (Megatons of oil equivalent) or 162 820 TWh. This corresponded to CO_2 emissions of 32 500 MtCO_2 per year [1].

To address these ever-increasing emissions, the European Union puts in major efforts to reduce greenhouse gas emissions by at least 80 % below 1990 levels by 2050 [2]. 3 key objectives were listed: first of all, an increase of the energy efficiency by 2% per year. Secondly, achieving nearly full decarbonization of the power sector by the implementation of renewables, nuclear energy and carbon capture & storage (CCS) and finally, a full replacement of fossil fuels by decarbonized electricity in buildings and in the transport sector [3].

Hence, the power generation sector is projected to undergo profound restructuring toward the dominance of renewable energy (e.g., solar energy, wind energy, and biomass) [4]. However, due to the variations in weather, season and location, renewable energy is unstable and discontinuous. The integration of variable renewable energy into the grid will increase the imbalance between the production and consumption of electricity, resulting in the abandonment phenomenon of renewable energy [5, 6]. This means that certain energy sources deliberately reduce the power output below what could have been produced in order to balance the energy supply and demand [7].

For this reason, the need for flexibility in the power system grows. This flexibility in the grid can be achieved in four different ways, namely dispatchable power plants, demand-side management, connections with adjacent markets and electricity storage [8]. Up to a certain penetration rate, the integration of wind and solar into the power mix can usually be managed using existing flexibility sources. The threshold depends on the system's location and characteristics and ranges roughly between 15% and 25%. As the penetration of wind and solar within energy systems increases, interest in electricity storage will grow [8].

Electricity storage has two primary functions: levelling the demand curve and ensuring power quality and reliability by providing ancillary services. For load levelling, the electricity storage is used to level the load over various timescales, thereby reducing the peak/off-peak amplitude (daily, weekly and seasonal demand). This can also occur over shorter timescales (hourly) to smooth the load and avoid activating peak plants. Ancillary services on the other hand try to maintain the system's frequency and voltage within technical limits to avoid instability and blackouts. This could be achieved by using fast-response electricity storage to inject or withdraw

power as an alternative to conventional reserves [8].

The requirements for the application of electricity storage largely depend on discharge time and power ratings, which determine cycling time and the importance of efficiency. The power rating rates the storage device's instantaneous ability to withdraw/inject energy from/into the grid. The discharge time indicates how long the storage can discharge at nominal power. It corresponds to the energy capacity of the storage divided by the power rating. Another important parameter is the power-to-energy ratio, it determines the typical storage cycling time of the system and provides an indication of the cycle frequency. Some applications require a long duration of output, while others require only short injections of high power. Finally, round trip efficiency defines the efficiency of the system. It is measured by the energy injected compared with the energy withdrawn. The importance of having a highly efficient system increases with increasing cycling frequency (e.g. ancillary service versus black start services) [8].

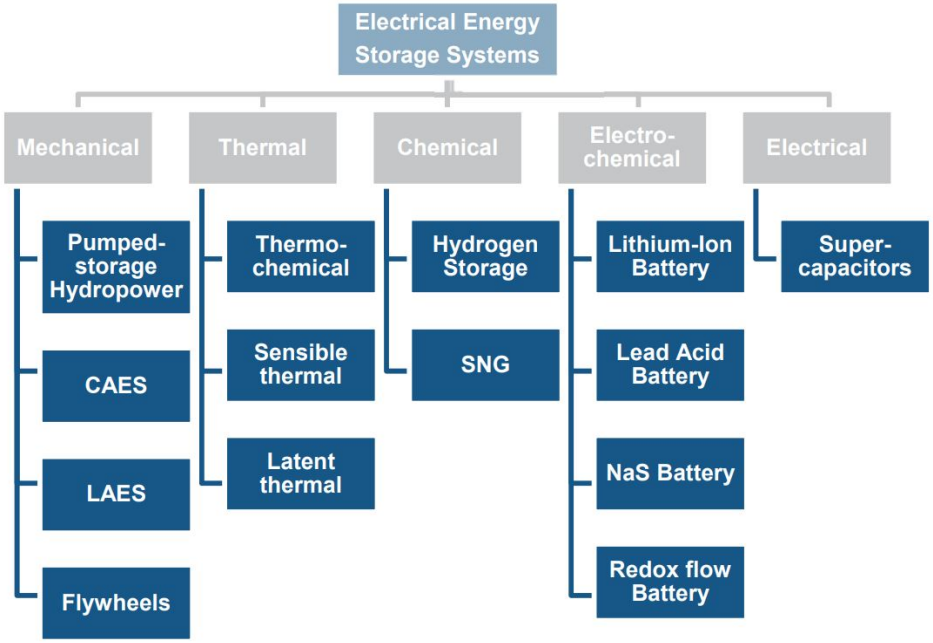

Figure 1.1: Scientific categorisation of storage [9]

Figure 1.1 divides storage technologies into five categories, which distinguish from each other by the form in which the energy is stored. The five categories are mechanical, thermal, chemical, electrochemical and electrical storage systems. Currently, the world energy storage capacity is dominated by Pumped Hydro Storage (PHS) [10], with a total installed storage power capacity of 96% of the total 176 GW (in 2017) [11]. Unfortunately, the easily-exploitable locations available for economically viable PHS are nearly exhausted [12]. So other ways of storing energy will have to be developed even further.

Examples of other possible technologies are compressed air energy storage (CAES), NaS battery energy storage system (BESS), molten salt Thermal Energy Storage (TES), flow battery energy storage (FBES)... [13] Each of the aforementioned storage systems has its own strengths and weaknesses, making them more suitable for a certain type of application. This mainly depends on technical characteristics like daily self-discharge, lifetime, cycling times, cycle efficiency and response time.

Table 1.1: Comparison of the technical parameters of different energy storage systems [13, 14]

Technology	Daily Self-Discharge (%)	Lifetime (Years)	Cycling Times (Cycles)	Discharge Efficiency (%)	Cycle Efficiency (%)	Response Time
PHS	Very small	40–60	10,000–30,000	87	70–87	Minutes
Large Scale CAES	Very small	20–40	8000–12,000	70–79	42–54; AA-CAES: 70	Minutes
Overground Small CAES	Very small	23+	30,000	75–90	-	Seconds–Minutes
Flywheel	>20% per hour	15–20	20,000	90–93	90–95	Seconds
Lead Acid	>0.3	5–15	21,000	85	63–90	Milli-seconds
Li-ion	>1	14–16	200–1800	85	75–97	Milli-seconds
Na-S	Almost zero	10–20	2500–4500	85	75–90	Milli-seconds
NiCd	>0.6	15–20	2000–3500	85	60–83	Milli-seconds
VRB	Very small	10–20	12,000	75–82	65–85	>1/4 cycle
ZnBr	Small	5–10	1500–2000	60–70	65–80	>1/4 cycle
PSB	Almost zero	10–15	-	-	60–75	20 Milliseconds
Capacitor	~50 in 15 min	1–10	5–50,000	75–90	60–70	Milliseconds
Supercapacitor	~20–30	10–30	100,000+	95–98	84–97	Milliseconds
SMES	10–15	20–30	100,000	95	95–98	Milliseconds
Solar fuel	Almost zero	-	-	-	20–50	-
Hydrogen Fuel Cell	Almost zero	~20	20,000	59	20–66	Seconds
TES	>1	20–30	-	-	30–60	Minutes
Liquid Air Storage	Small	25+	-	-	55–80	Minutes

Table 1.1 shows a comparison of the most important technical parameters for several relevant energy storage systems. As mentioned before, PHS is by far the most implemented type of energy storage and it is also the most mature technology [8]. It is capable of producing high powers and has a long lifetime of 40-60 years. A major downside of PHS, however, is the limited use due to geographical and environmental restrictions. Also, its response time is much higher compared to batteries for example. On the other hand, electrochemical storage accounts for about 1.1% of the total installed storage power capacity [11]. Examples are Lithium-Ion battery energy storage systems (BESS), Na-S, Lead Acid BESS... Compared to the mechanical types of storages, BESS have a really low response time. The major strength is their high range of available sizes and powers. On the other hand, they struggle with recycling and the usage of hazardous chemicals like Lead, Cadmium, Sulfur, etc. Also compressed air energy storage (CAES) is sometimes implemented, although its installed capacity is only 0.4% of the total grid-connected capacity in 2017. CAES has similar technical characteristics as the PHS. Unfortunately here as well the technology struggles with very specific geological restrictions, e.g. the heavy dependence on large enclosed air volumes like caves and mines.

Finally, thermal energy storage (TES) can be an interesting technology. TES already exists in a wide spectrum of applications. It uses materials that can be kept at high/low temperatures in

insulated containers. Heat/cold can then be applied for electricity generation using heat engine cycles. Energy input can, in principle, be provided by electrical resistance heating or refrigeration/cryogenic procedures [15]. TES covered 1.9 % of the total installed storage power capacity in 2017, making it the largest category after PHS [11]. Currently, molten salt TES combined with concentrated solar power (CSP) is the most implemented technology for the storage. In this case, salt in a high-temperature container (up to 570 °C) is heated by concentrated solar power. Its main assets are the high thermal energy storage capacity, a high electrical power rating, and the scalability (e.g., Crescent Dunes Solar Energy Project 110 MW_{el} installed power and 1.1 GWh electrical energy storage) [16]. Although TES combined with CSP is quite mature, it is still a niche application and is very dependent on the climate for its economical viability.

In the light of geographical independence and scalability, Carnot batteries (CB) can be a promising technology [17]. Since, CB is quite a broad term a more elaborate definition will be provided in Section 2.1. One of the significant subgroups that can be identified within the group of Carnot batteries is pumped thermal electricity storage (PTES). PTES is based on a high-temperature heat pumps (HP), which transforms the off-peak electricity into thermal energy and stores it inside man-made thermally isolated vessels (charging cycle mode) [18]. During delivery, a heat engine (HE) is adopted to convert the stored thermal energy back into electrical energy (power cycle mode) [19]. Hence, most PTES consist of three main components: a HP, a TES and a HE. Several different types of HP, TES and HE are available and have to be selected depending on the intended operating conditions. Some of the most common implementations will be discussed in section 2.3.

PTES find wide applications in load leveling and electricity production by heat engines [8]. Hossain et al. [13] studied a number of different storage technologies and reviewed the available literature. The authors analysed and compared the suitability of storage technologies for certain grid supporting services. Several studies showed a good match for PTES with load leveling applications like generation capacity reserves and transportation & distribution peak shaving. However, little to no studies were available where PTES are evaluated for the application in these ancillary services. As mentioned before, these services ensure power quality and reliability and have time constants in the order of seconds or minutes [20]. These ancillary services can be devised in different categories in which frequency balancing service is the most renowned. An overview of the categories is provided in Figure 1.2. Balancing service providers (BSPs) such as generators, demand response facilities and storage operators can offer balancing services (capacity and/or energy) to the transmission system operators, who in turn use these services to balance the frequency of the grid [21].

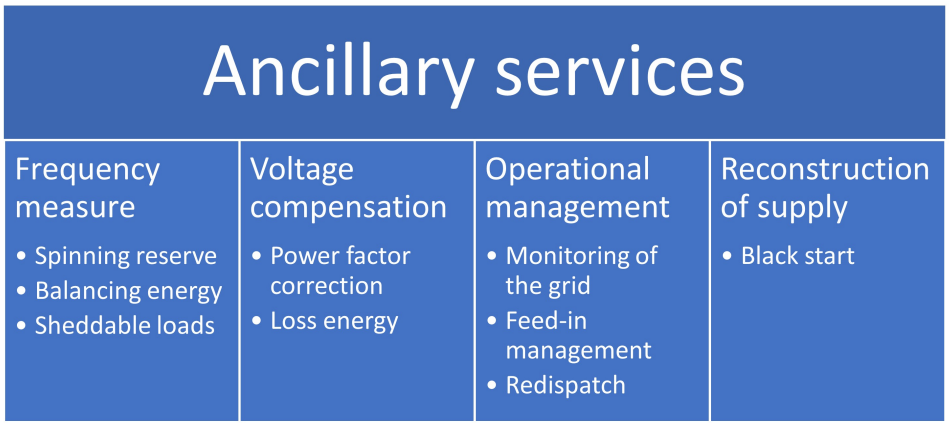

Figure 1.2: Overview ancillary services [22]

1.2 Goal

The goal of this thesis is to evaluate the performance of high-temperature heat pumps in Carnot batteries for grid balancing services. To be able to perform this evaluation, a dynamical model will be developed in Dymola. Next pre-qualification tests for balancing services in Europe will be applied to simulate its performance. This research also tries to improve the insight and understanding in the limitations of fast dynamics in high-temperature heat pumps.

1.3 Outline

To determine the scope of this thesis, certain limitations are imposed. First of all, only the heat pump part of the Carnot battery will be studied. Secondly, the heat pumps are limited to the use of subcritical Rankine-cycle heat pumps.

Chapter 2

Literature study

2.1 Definition

Carnot batteries (CB) include several technologies. Due to the complexity of these systems, it becomes difficult to provide a single definition including all the different systems. Dumont et al. [23] proposed a definition for Carnot batteries: A Carnot battery is a system primarily used to store electric energy. In a Carnot battery, the electric energy (input) is used to establish a temperature difference between two environments, namely the low temperature (LT) and high temperature (HT) reservoirs. In this way, the storage is charged, and the electric energy is stored as thermal exergy. As the heat flows against the thermal gradient, work is spent to charge the storage. In the discharge phase, the thermal exergy is discharged by allowing the heat to flow from the HT to the LT reservoir. The heat flow powers a heat engine (HE) which converts it into work and discharges the residual heat into the LT reservoir. In this way, a fraction of the electric input is recovered. The different energy flows are illustrated in Figure 2.1

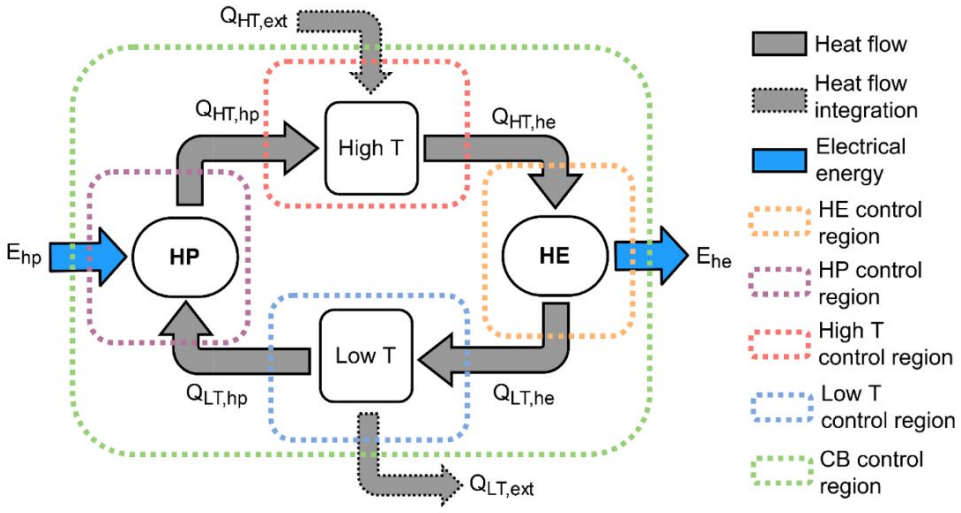

Figure 2.1: Illustration of the energy flow of a Carnot battery [23]

2.2 Advantages and drawbacks of Carnot batteries

Carnot batteries have some major advantages compared to other storage technologies. First of all, the geographical independence: as opposed to PHS, CB are not bound to specific geographical requirements like caves and pre-existing reservoirs, hence they can be installed everywhere [24]. Secondly, CB are made up of pumps, compressors, expanders, turbines and heat

exchangers, which are all components that may easily be scaled up [23]. Moreover, these components are usually available on the shelf, facilitating the development [23]. Furthermore, it is possible to valorize waste heat that would otherwise be dumped into the atmosphere [25]. A final advantage is their potential to become cheaper when scaled to larger capacities.

However, a major drawback is the rather low round trip efficiency (i.e. the electricity output divided by the electricity input). For now, the round trip efficiencies are usually rather low (30 % - 70 % [23]) compared to for instance PHS and CAES. However, CB with a heat pump and Rankine cycle have an estimated technology readiness level of 7 [23], meaning it is still in the phase where system prototypes are implemented in an operational environment. Hence many aspects still have to be studied in detail. Further research will push the boundaries of the achievable round trip efficiencies and will expose its true potential. Besides the low round trip efficiency, a Carnot battery also has a lower specific energy (Wh/kg) compared to e.g. electrochemical batteries and flywheels. Furthermore it has an energy density (Wh/l) similar or lower then Li-ion batteries, but this mainly depends on the implemented temperature differences of the thermal storage tanks. The higher the temperatue differences, the higher the energy density. Furthermore the reaction time is in the order of minutes, which is in the same order of magnitude as PHS and CAES. However, the response time is much larger compared to for instance electrochemical batteries (milliseconds) [13].

2.3 Different types of Carnot batteries

For charging, electric energy is used to transport heat from the LT to the HT reservoir. This may be done with a heat pump (HP), an electric heater, or any other technology. Likewise, during discharge, any heat engine technology may be used, ranging from Rankine, Brayton, or different thermodynamic cycles, to thermoelectric generators [23]. Consequently, many different Carnot battery configurations are possible, with the most common being: Brayton-based, Rankine-based, reversible cycles and finally with an electric heater as heat source.

2.3.1 Brayton

A Brayton Carnot battery usually consists of a Brayton heat pump and a Brayton heat engine. In general two variants of the Brayton CB can be distinguished, namely, Brayton CB with dynamic [26] or volumetric machines [27]. Both the heat pump and the heat engine are based on the Brayton cycle which is mostly connected with two sensible heat thermal reservoirs (HT and LT).

In Figure 2.2 a Brayton refrigeration cycle is represented. The ideal cycle, denoted by 1-2s-3-4s-1, assumes isentropic compression and expansion, whereas the cycle denoted by 1-2-3-4-1, shows the effects of irreversibilities during adiabatic compression and expansion. The cycle consists of 4 processes. **Process 1-2:** Compression from state 1 to the pressure at state 2. **Process 2-3:** Heat input it flows at constant pressure through the heat exchanger. **Process 3-4:** Expansion process from state 3 to state 4. **Process 4-1:** Heat output at constant pressure through the low temperature heat exchanger to complete the cycle [28].

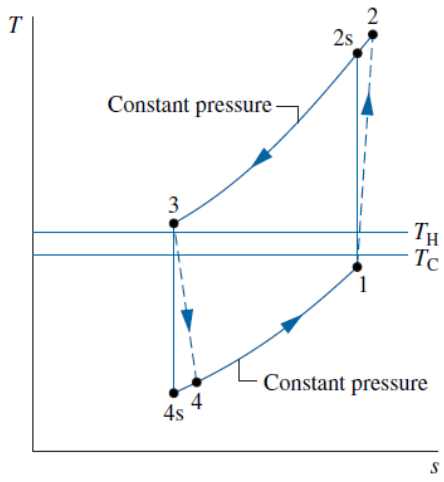

Figure 2.2: Ts diagram of a Brayton refrigeration cycle [28]

An example of a Brayton CB layout equipped with dynamic compressors and expanders is discussed by Desrues et al. [26]. It reaches a maximum temperature of 1000 °C, while the minimum temperature is around -70 °C. Due to the high temperatures, a high energy density is achievable. However, the maximum temperature is held back by the technical limitations for compressors. The pressure ratio is rather low, around 4.6 and the round trip efficiency is in the range of 60% to 70%. The authors assumed a polytropic efficiency of the dynamic machines of 90 % for a system of 100 MW/600 MWh [26].

The system proposed by Howes et al. [27] is also based on a Brayton cycle with Argon as a working fluid, but now volumetric machines are used. It consists of only 2 volumetric machines since they can operate both as compressor and expander. The temperatures of the hot and cold reservoirs were respectively 500 °C and -166 °C. This system was further studied by White et al. [29] and McTigue et al. [30]. The authors found with an optimistic set of parameters (polytropic efficiency of 99 % and no mechanical or electrical losses included), the round trip efficiency could exceed 85 %. However, when taking into account electrical and mechanical losses in the cycle (for instance pressure drop in the valves and heat losses to the environment), the estimated round trip efficiency drops just below 70 %. Finally, the authors investigate the performance when dynamic compressors and expanders would be implemented with an assumed polytropic efficiency of 90 %. According to the authors, the estimated round trip efficiency is in this case unlikely to exceed 50 %.

2.3.2 Rankine-based systems

HP/RC technology based on Rankine cycles typically works at much lower temperatures, which is beneficial for the thermal losses of the pipes and the reservoir [23]. Moreover, they are more suited for the use of phase change materials (PCM) as a storage medium, since the refrigerant also changes phase in the heat exchangers. [23].

In Figure 2.3 a vapor-compression cycle is represented. It consists of 4 processes. **Process 1-2:** Compression of the refrigerant from state 1 to the condenser pressure at state 2. **Process 2-3:** Heat transfer from the refrigerant as it flows at constant pressure through the condenser. The refrigerant exits as a liquid at state 3. **Process 3-4:** Throttling process from state 3 to a two-phase liquid-vapor mixture at 4. **Process 4-1:** Heat transfer to the refrigerant as it flows at constant pressure through the evaporator to complete the cycle [28].

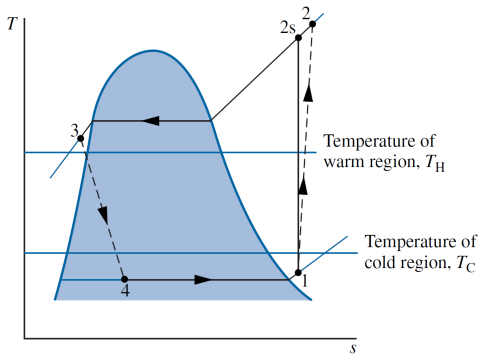

Figure 2.3: Ts diagram of an actual vapor-compression cycle [28]

Maximum efficiencies achieved by Brayton and Rankine systems are in the same range, around 60% [17]. However, these round trip efficiencies are strongly affected by the assumed compressor and turbine efficiencies and the assumption of thermal integration. Morandin et al. [17] assumed a turbine isentropic efficiency of 88 %, a compressor isentropic efficiency of 86 % and thermal integration.

Thermal integration (TI) is a technology where available waste heat is employed to boost the performance of the system. Compared to a PTES without TI, there are two different options to operate a thermally integrated pumped thermal energy storages (TIPTES). On the one hand, the hot storage configuration uses a heating system to increase the waste heat temperature. This allows the power cycle to increase its performance by working with a higher temperature difference compared to the heating system. On the other hand, the cold storage configuration stores thermal energy at temperatures lower than the ambient. Then the waste heat is the heat source for the power cycle. Once again, it allows the power cycle to work efficiently with a higher temperature difference [31].

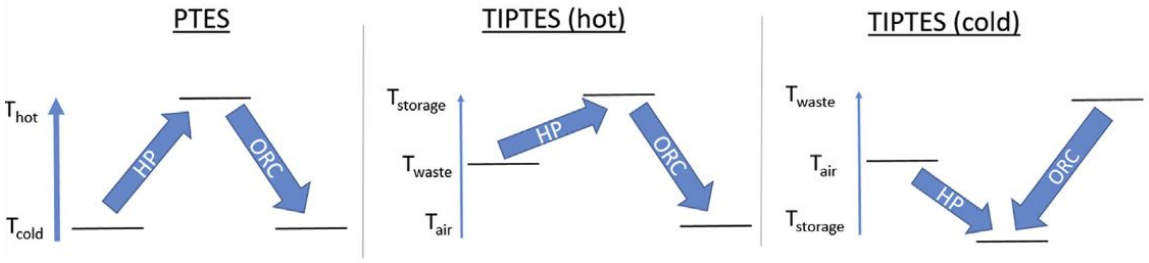

Figure 2.4: Thermally integrated hot and cold storage [31]

Frate et al. [32] performed a multicriteria analysis of a rankine pumped thermal electricity storage system with low-grade thermal energy. The system is composed of an ORC for the discharging and a high-temperature heat pump for the charging phase. The results showed that by exploiting a thermal energy source at 80 °C, a round trip efficiency of 55 % can be achieved. This result is based on a compressor isentropic efficiency of 80 % and an expander isentropic efficiency of 85 %.

Another example of a Rankine-based cycle is presented by Henchoz et al. [33]. As cold storage, it implemented a latent storage tank at sub-ambient temperatures of 0 to -50 °C. The system sizing is 50 MW, 400 MWh and it is thermally integrated by solar collectors. The assumed isentropic turbine, compressor and pump efficiency are 90 %, 88 % and 85 % respectively. All together the selected system has a round trip efficiency of 57%.

A major advantage of this HP/RC technology is that it is made up of less complex compressors, turbines and heat exchangers, which are all components that are commercially available. Hence, large scale system development may potentially be facilitated compared to other emerging technologies. For larger applications, multiple HP and ORC could be used in parallel, making the design more modular [23].

2.3.3 Electric heater as a heat source

Besides heat pumps, also electrical heaters can be used to convert the electrical power to heat. This makes the Carnot battery more simple and compact, but typically achieves lower round trip efficiencies of 12% to 55% [23]. An example of research performed on this topic is presented by Henchoz et al. [33], also commercial applications are for example provided by a company named 247Solar Inc. [34]. Both projects implement electric heaters to convert electric power to heat. However, for discharging, [34] uses a Brayton Cycle, while [33] uses a steam Rankine Cycle. Regarding the power output, electrically heated systems are well scalable by placing many blocks in parallel. Novotny et al. [35] stated that in order for the electricity heated Brayton cycle to be efficient, very high storage temperatures need to be reached, namely exceeding 1000 °C. However, the need of reaching such a high temperature to increase round trip efficiency also leads to material constraints.

2.3.4 Reversible

Reversible CB power systems, work in a similar way as a system with the HP and HE separated. This technology can be based on a Brayton cycle using reciprocating reversible piston machines capable of working as both compressor and expander [35]. Dumont et al. [36] also studied the concept of Heat Pump/organic Rankine cycle power systems. There, the authors stated that it can significantly reduce the required investments since only a single machine is required rather than the combination of a heat pump and heat engine.

2.4 Performance indicators

Basically, a heat pump uses mechanical energy to transfer thermal energy from a source at a lower temperature to a sink at a higher temperature. A heat engine on the other hand, generates work using a heat source. In a heat engine the high temperature heat source provides the heat input to get the energy output in a form of work. However, there is also an amount of heat that is discarded at the sink [37].

Every component, in a Carnot battery, is characterized by a coefficient of performance (COP) or an efficiency [25]. For the HP, the COP is represented by equation 2.1

$$COP = \frac{Q_{HT,hp}}{E_{hp}} \tag{2.1}$$

where E_{hp} is the electrical energy consumed by the HP, and $Q_{HT,hp}$ is the heat provided by the HP to the TES tank.

For the HE the efficiency can be defined by:

$$\eta_{he} = \frac{E_{he}}{Q_{HT,he}} \tag{2.2}$$

where E_{he} is the electric energy generated by the HE and and $Q_{HT,he}$ is the heat extracted by the HE from the TES.

Finally the TES efficiency can be calculated by:

$$\eta_{st} = \frac{Q_{HT,he}}{Q_{HT,hp}} \tag{2.3}$$

where $Q_{HT,he}$ and $Q_{HT,hp}$ are respectively the heat extracted from the TES and the heat provided to the TES.

The HP, the TES and the HE are arranged in series, hence the combined efficiency is the multiplication of the individual efficiencies. As such the combined efficiency is the ratio of the absorbed and returned electric energy:

$$\eta_{rt} = \frac{E_{he}}{E_{hp}} = COP \cdot \eta_{st} \cdot \eta_{he} \tag{2.4}$$

In the rest of the manuscript, the combined efficiency of the system including the HP, TES and HE will be called the round trip efficiency (η_{rt}).

If the temperature difference over the ORC and the HP is equal the round trip efficiency cannot be higher than 1. It is, however, possible to develop a PTES system that takes advantage of an available waste heat source to provide heat at a temperature higher than the ambient temperature. Thermal integration (TI) can be implemented either with a cold or a hot storage tank as illustrated in Figure 2.4. In both cases the thermal integration results in a larger temperature difference over the ORC compared to the temperature difference over the HP. This allows more energy to be extracted by the ORC. Since the definition of round trip efficiency only takes into account the amount of electric energy, the achievable round trip efficiency can be higher than one, as stated by Frate et al. [25].

The aforementioned parameters will allow to evaluate the performance of the modelled CB and compare it with different technologies.

2.5 Selection of Carnot battery type and boundary conditions

The following part of the literature study and the rest of this thesis research focuses on the HP side of the CB based on a vapor compression cycle. Emphasis is placed on the dynamic behaviour of the heat pumps, to test its capabilities of delivering balancing services to the grid. Hence, fast dynamics are of great importance when designing the cycle and selecting components. Also for the remainder of this literature study focus is placed on finding relevant studies about the dynamics of (high temperature) heat pumps (HTHP) and its components. Also the requirements for a power system to qualify for delivering balancing services are discussed in more detail in section 2.10. However, first the intended operating conditions are discussed to form a base for the selection of the components and the refrigerant.

First of all, the boundary conditions (temperatures) should be determined. As explained before in section 2.3.2 the concept of thermal integration, where low-temperature heat sources are implemented, can be very interesting since it decreases the temperature lift of the heat pump in the Carnot battery. Hence, the required compression work during the charging of the storage system is reduced [38], while the work during discharge remains the same.

Marina et al. [39] presents an estimation of the European industrial heat pump market potential in terms of magnitude, sizing and number of units. The authors also looked into the available waste heat that could potentially be used as a low-temperature source for thermal integration. The data can be found in Figure 2.5.

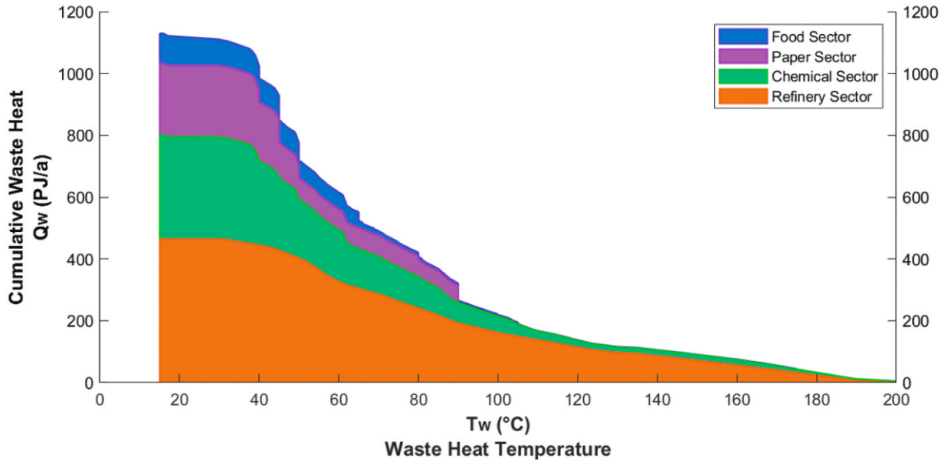

Figure 2.5: Cumulative waste heat <200 °C in EU28 identified in processes that make up the heat pump market study [39]

From Figure 2.5 a waste heat temperature can be proposed. Two important factors have to be taken into account for this decision. First of all, the availability, since more heat is available at lower temperatures. Secondly, the influence on the efficiency of the lower temperature lift of the heat pump cycle.

Balancing out both the availability and the efficiency, a waste heat temperature in the range of 50 to 80 °C is proposed for this thesis research. This waste heat temperature can correspond with an evaporation temperature of about 35 °C to 65 °C in the evaporator. According to studies like [40] and [41], typical temperature lifts ($\Delta T_{lift} = T_{cond} - T_{evap}$) are between 40 and 80 °C. Hence, condenser temperatures between 75 °C and 145 °C are possible, depending on the other assumptions. Therefore, the expected temperatures of the refrigerant for this thesis are estimated to be in the range of 35 °C to 145 °C. This temperature interval can be used as a base for the selection of the refrigerant in section 2.6.

Concerning the power of the system, relatively large powers are anticipated. Definitely in future versions where these Carnot batteries could be large scale storage applications. For this research the compressor power will be fixed to 1 MW electric. Looking at examples of industrial HTHP in Arpagaus et al. [42] or the ones manufactured by Johnson Controls [43], a system of 1 MW seems well within the possibilities of current technology.

2.6 Refrigerant selection

Since the operating temperatures determined within a certain interval, also the optimal refrigerant has to be determined to fit these boundary conditions. For the selection of a proper refrigerant, an important parameter is the required degree of superheat (SH) after evaporation. Low SH values could result in wet compression, while high values could decrease the evaporation temperature and affect significantly the system performance. The refrigerants could be classified into three groups based on the slope of the saturated vapour curve on Ts diagram (dT/ds) . The negative slope refrigerants are called "wet fluids", the positive slope ones are called "dry fluids", and semi-vertical slope refrigerants are called "isentropic fluids" [44]. Figure 2.6 presents a comparison of the three types of curves showing one representative refrigerant for each case.

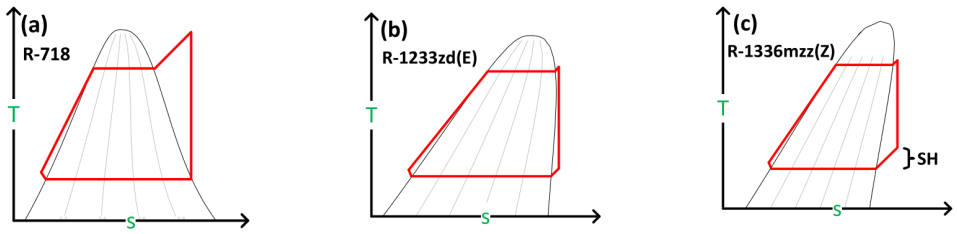

Figure 2.6: T-s diagram for: (a) R-718 (wet fluid), (b) R-1233zd(E) (isentropic fluid), and (c) R-1336mzz(Z) (dry fluid) [45]

As it can be seen from the previous figure, wet fluids will not necessarily require superheating at the evaporator's outlet port, while dry fluids need a very high degree of SH to prevent wet compression operation. On the other hand, the isentropic fluids need a moderate degree of SH that can be done inside the evaporator without side effects on the system performance.

Other desirable criteria of the refrigerants used especially in the HTHP applications are zero ozone depletion potential (ODP = 0), very low global warming potential (GWP < 10), non-toxic, no or low flammability, high critical temperature ($T_{crit} > 145$ °C) allowing for subcritical applications and low critical pressure ($p_{crit} < 3MPa$) [45]. The performance on these criteria for several refrigerants is summarized in Table 2.1:

Table 2.1: Properties of selected refrigerants for HTHPs [45] [40] [46]

Group	Refrigerant	Type	T_{crit} (°C)	P_{crit} (MPa)	NBP[a] (°C)	ODP (-)	GWP (-)	SG[b]
Wet (W)	R-718 (water)	Natural	373.95	2.206	100.0	0	0	A1
	Acetone	HC[c]	235.0	4.7	56.0	0	<10	n.a.
Dry (D)	R-1336mzz(Z)	HFO[d]	171.3	2.9	33.4	0	2	A1
	R-365mfc	HFC[e]	186.85	3.266	40.2	0	804	A2
Isentropic (S)	**R-1233zd(E)**	**HCFO[f]**	**166.5**	**3.62**	**18.7**	**0.0003**	**<1**	**A1**
	R-245fa	HFC	154.01	3.65	15.1	0	858	B1
	Butene	HC	146.15	4.0	-6.3	0	<10	n.a.

In Table 2.1: NBP: the normal boiling point at 0.1013 MPa; SG: safety group; HC: Hydrocarbons, HFO: hydrofloroolefins; HFC: hydroflorocarbons; HCFO: hydrochlorofluoroolefins.

Figure 2.7 shows the work ranges for refrigerants listed in Table 2.1. The working range is defined as the interval between the critical temperature (T_{crit}) and the normal boiling point (NBP). This gives an idea of the ability of the refrigerant to reach a certain condensation temperature (T_{cond}).

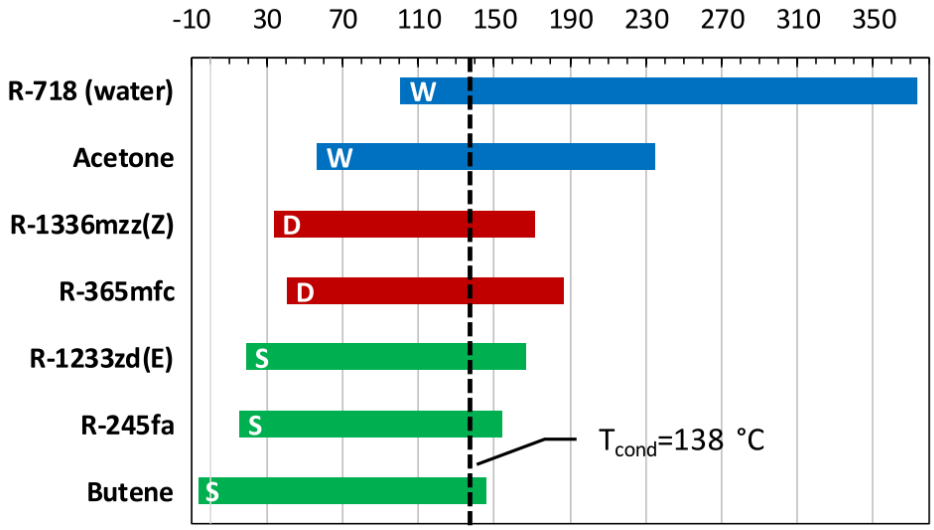

Figure 2.7: Work ranges for selected refrigerants and condensation temperature (T_{cond}) (W = wet, D = dry, S = isentropic) [45]

According to Arpagaus et al. [40], for subcritical HTHPs, the difference between T_{crit} and T_{cond} should be between 10 and 15 K to ensure reasonable performance [41]. The wet fluids, Water and Acetone, have many desirable properties, such as very high latent heat and T_{crit}. However, because of its lower vapour density, it requires complicated multi-stage compression cycles with intercooling to cope with the high values of the pressure ratio and discharge temperature. Also, they have very high NBP values which means that the HTHP's evaporator could work under negative pressure, especially for source temperatures lower than 60 °C. As a consequence, the air can infiltrate easily into the cycle in the presence of any leakage. Therefore, Water and Acetone are typically not used for HTHP with condenser temperatures lower than 150 °C.

Also, the dry fluids, R-1336mzz(Z) and R-365mfc require high SH values to prevent the wet compression. This significantly decreases the evaporation temperature and, consequently the system performance. Moreover, it requires an external superheater to prevent this performance degradation, which drives up the cost of the system [45].

Considering the previous analysis and the intended temperature range of the Compressed Heat Energy Storage for Energy from Renewable sources project, or in short CHESTER [47], the selected working fluid was R-1233zd(E). This decision was mainly based on the very desirable features, such as the high volumetric heating capacity (VHC), low discharge temperatures, low pressure ratios, and they require low values of SH, compared to dry fluids. Moreover, it is non-flammable, non-toxic and has a very low GWP [45].

Eppinger et al. [48] also studied pumped thermal energy storage with heat pump-ORC systems. The goal of the research was to compare latent and sensible thermal storages for various fluids. Also, this research showed that for most cases R-1233zd(E) appeared to be the best choice, based on efficiency, environment, sustainability and safety.

Another research paper that studied the suitability ranges of high-temperature heat pump working fluids is [42]. Starting from 122 fluids and restricting the analysis to many of the parameters mentioned before (critical temperature, boiling point, GWP, ODP, flammability, toxicity...) the selection was narrowed down to a more concise collection of refrigerants. The authors first stated that the use of toxic and flammable fluids can be justified in terms of economic advantages when

efficiency gain is important. In this category were fluids like acetone, benzene, cyclopentane, dichloroethane... However, if less efficient fluids are preferred due to higher VHC and lack of toxicity or flammability, synthetic refrigerants (namely R-1336mzz(Z), R-1234ze(Z), R-1233zd(E) and R-1224yd(Z)) provided a very effective alternative. Based on a final comparison and a consideration of the VHC and the COP, the refrigerant R-1233zd(E) was again recommended. Since legislation tries to restrict the use of toxic and flammable fluids that are bad for the environment [49], the refrigerants like acetone, benzene, cyclopentane... are not further considered in this thesis research.

According to Frate et al. [49], who reviewed Rankine Carnot batteries with the integration of thermal energy sources, CFC and HCFC are forbidden in Europe and they were replaced by HFCs like R-134a. However now HFOs and HCFOs or natural hydrocarbons are preferred due to the minimal environmental impact. Hence, to be future proof, it might be interesting to also avoid the HFCs.

According to Meesenburg et al. [50], the most common type of heat pump supplying district heating in Denmark is the two-stage ammonia heat pump. However, studies as [42], make comments about the health-hazard grade 3 of ammonia and the incompatibility with copper and brass, thus forcing the use of steel for thermal equipment. They also typically deliver max temperatures of about 90-95 °C [43], due to the rather low critical temperature. These arguments also discard the use of ammonia for the intended application.

To conclude, it appears that most literature agrees to use R-1233zd(E) for HTHP with operating temperatures between 35 °C and 145 °C.

2.7 Compressor selection

The compressor is the heart and driving force of the heat pump and the selection can have major influences on the performance of the system. Apart from the operating conditions, some basic factors to consider are the capital cost, operating efficiency, field serviceability, availability of spares and maintenance [51]. Many different compressor types exist and each of them uses a different approach to pressure the refrigerant. Consequently, every technology has its own limitations for the achievable volume flow rates and pressure ratios.

The graph in Figure 2.8 can be a guideline to determine what types of compressors are applicable to certain operating conditions. Later, in the model development in Chapter 3, the nominal operating temperatures, pressures and mass flow rates will be determined more specifically. This will allow to select the most suited compressor type.

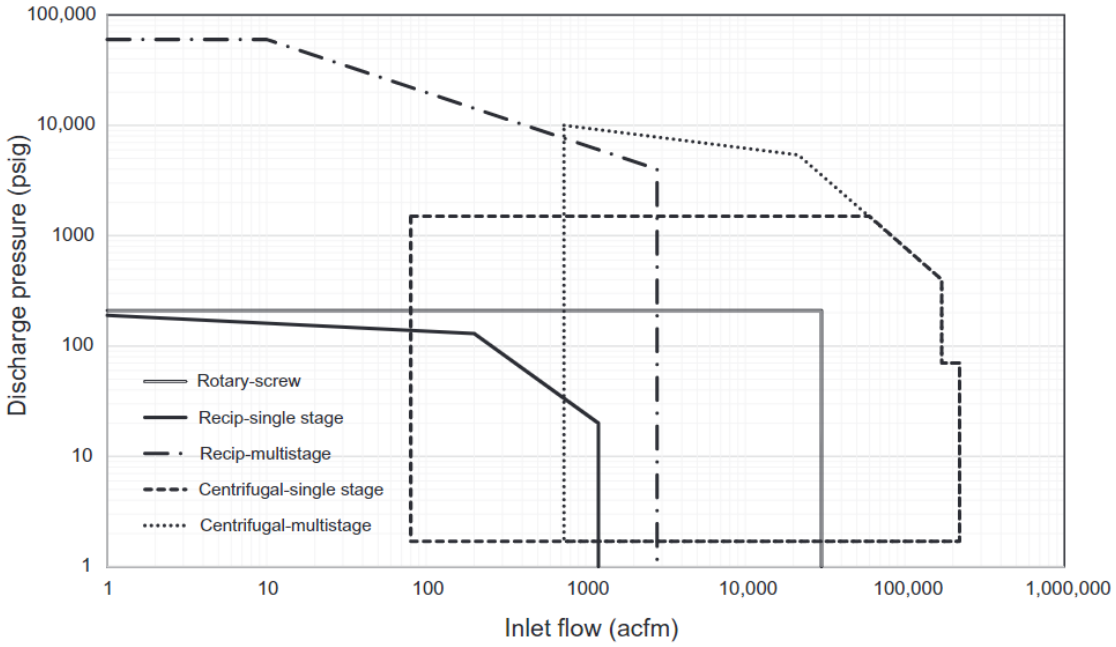

Figure 2.8: Compressor coverage chart [52]

Practical examples

In this section, an overview will be presented of several practical applications or state of the art research of high temperature heat pumps. Focus will be on the implemented compressor technology.

Sabroe, which is a product brand by Johnson Controls manufactures high power heat pumps. They are divided into 3 categories: the HeatPAC, the DualPAC and the Screw heat pumps. The heat pumps all use ammonia as the refrigerant and provide a hot water supply at up to 90 °C. The Sabroe HeatPAC heat pump implements a reciprocating compressor and requires a maximum shaft power of 444 kW. The Sabroe DualPAC heat pumps consist of a two-stage ammonia-based cycle and require a maximum shaft power of 608 kW. In the final and largest type, a screw compressor is implemented and has a nominal power consumption of about 1200 kW for the single-stage heat pump and 2375 kW for the two-stage variant [43].

In [45], the design of the CHESTER project is explained. The project aims to develop an innovative compressed heat energy storage (CHEST) system that allows the managing, storing and discharging of energy using different renewable energy sources (RES) through the combination of electricity and heat sectors. The selected refrigerant was R-1233zd(E), the source temperature will be $T_{source,HTHP} = 55 - 100$ °C and the sink temperature is $T_{sink,HTHP} = 133$ °C. In this project the intended capacity of the full CHEST system is in the order of several MW and larger. According to the authors, the best compressor technology will be a radial compressor. However, for the smaller prototype (10 kW_{el}), a piston compressor was chosen.

Frate et al. [49] reviewed Rankine Carnot batteries with the integration of thermal energy sources. The authors state that both for the heat pumps and for ORCs the compressor technology varies in the volumetric flow rates, which in turn is affected by the electrical and thermal sizes of the system and by the operating fluid. For low-power input thermally integrated pumped thermal energy storages (TIPTES) (1 - 100 kW_{el}) piston, scroll and screw compressors are typically used. However, for larger applications (100 - 1000 kW_{el}) screw, twin-screw or centrifugal compressors are used and commercially available [42].

According to Frate et al. [42] multistage and single-stage centrifugal compressors are likely to be the most suited for high-temperature heat pumps with a thermal power of 500 - 2000 kW_{th} at the evaporator. Even if in some cases screw compressors could handle the resulting volumetric flows. Their research also demonstrated that the refrigerant R-1233zd(E) can give a good compromise between COP and Volumetric Heating Capacity (VHC).

The range of heat pump models on the market with high heat capacities and sink temperatures has grown steadily in recent years. Over 20 heat pumps models from 13 manufacturers have been identified worldwide, which are able to supply at least 90 °C heat. The authors of [40] summarized a selection of these HTHP in Table 2.2

Table 2.2: Selection of industrial HTHPs with heat sink temperatures above 90 °C [40]

Manufacturer	Product	Refrigerant	Max. heat sink temperature	Heating capacity	Compressor type
Kobe Steel (Kobelco steam grow heat pump)	SGH 165 SGH 120 HEM-HR90,-90A	R134a/R245fa R245fa R134a/R245fa	165 °C 120 °C 90 °C	70 to 660 kW 70 to 370 kW 70 to 230 kW	Twin screw
Vicking Heating Engines AS	HeatBooster S4	R1336mzz(Z) R245fa	150 °C	28 to 188 kW	Piston
Ochsner	IWWDSS R2R3b IWWDS ER3b IWWHS ER3b	R134a/ÖKO1 ÖKO (R245fa) ÖKO (R245fa)	130 °C 130 °C 95 °C	170 to 750 kW 170 to 750 kW 60 to 850 kW	Screw
Hybrid Energy	Hybrid Heat Pump	R717/R718 (NH_3/H_2O)	120 °C	0.25 to 2.5 MW	Piston
Mayekawa	Eco Sirocco Eco Cute Unimo	R744 (CO_2) R744 (CO_2)	120 °C 90 °C	65 to 90 kW 45 to 110 kW	Screw
Combitherm	HWW 245fa HWW R1234ze	R245fa R1234ze(E)	120 °C 95 °C	62 to 252 kW 85 to 1301 kW	Piston
Dürr thermea	thermeco$_2$	R744 (CO_2)	110 °C	51 to 2'200 kW	Piston (up to 6 in parallel)
Friotherm	Unitop 22 Unitop 50	R1234ze(E) R134a	95 °C 90 °C	0.6 to 3.6 MW 9 to 20 MW	Turbo (two-stage)
Star Refrigeration	Neatpump	R717 (NH_3)	90 °C	0.35 to 15 MW	Screw (Vilter VSSH 76 bar)
GEA Refrigeration	GEA Grasso FX P 63 bar	R717 (NH_3)	90 °C	2 to 4.5 MW	Twin screw (63 bar)
Johnson Controls	HeatPAC HPX HeatPAC Screw Titan OM	R717 (NH_3) R717 (NH_3) R134a	90 °C 90 °C 90 °C	326 to 1'324 kW 230 to 1'315 kW 5 to 20 MW	Piston (60 bar) Screw Turbo
Mitsubishi	ETW-L	R134a	90 °C	340 to 600 kW	Turbo (two-stage)
Viessmann	Vitocal 350-HT Pro	R1234ze(E)	90 °C	148 to 390 kW	Piston (2−3 in parallel)

As was stated in section 2.5, the proposed size for this thesis research is 1 MW electric power for the compressor. Based on the examples [43], [45], [49] and [42], it appears that piston, twin-screw as well as (radial) dynamic compressors are the most implemented types for these high-temperature heat pump applications. Depending on emphasis in the design, like efficiency, compactness, volumetric flow rate..., a well-founded decision can be made.

2.8 Heat exchanger selection

In this section, literature is compared to find the most suitable type of heat exchanger for industrial heat pump applications.

According to [53] both for HPs and ORCs, Chevron plate heat exchangers may be used. The authors state that such heat exchanger technology is especially suited for very small systems (1 - 10 kW_{el}), due to the reasonable cost and compactness, but it can also be used in much larger applications (hundreds of kW_{el}), due to their modular nature, as investigated in [40]. For larger

applications, in the order of 1000 kW_{el} or higher, shell and tube heat exchangers should be used, as recommended by [54] for ORCs.

A second study, conducted by Walraven et al. [53], compared shell-and-tube with plate heat exchangers for use in low-temperature organic Rankine cycles. ORC are different from heat pumps, however they also contain an evaporator and condenser and they work with similar cycles and working fluids. Hence, this study is assumed to be representative for heat pumps as well. The authors concluded that ORCs with plate heat exchangers perform mostly better than with shell-and-tube heat exchangers. They also mentioned one disadvantage of plate heat exchangers, that the geometry of both sides is the same, which can result in an inefficient heat exchanger.

ORCs are often designed based on experience, but this experience will not always lead to the most optimal configuration [53]. According to literature, plate heat exchangers and shell-and-tube heat exchangers are both applicable. Depending on if more emphasis is placed on compactness, price, efficiency... a certain type can be selected.

In [55] a general comparison has been made between a plate heat exchanger and a shell and tube heat exchanger. The book states that in many applications, the plate heat exchanger (PHE) has replaced the shell and tube heat exchanger (STHE). The merits of the PHE over the STHE are: the ability to handle multiple duties and future expansion, the high heat transfer ratio, the low operating weight ratio, the low hold-up volume, no welds, no flow-induced vibrations, access for inspection is easy and less time consuming, true countercurrent is achieved, very close approach temperature can be achieved, high turbulence, less fouling, leakage is easily detected and finally it is easy to replace plates and/or gasket.

For this dynamic research, the lower hold-up volume and the lower operating weight ratio can have a positive influence on the dynamic behaviour, as it can decrease the time constant of the slowest component in the heat pump cycle.

2.9 Storage tank topologies

In the context of Carnot batteries, one can find different approaches for the storage tank topology. Thermal energy storages can be divided into three categories: sensible, latent and thermochemical. With the proposed range of condenser temperature between 75 °C and 145 °C, pressurized water is the most cost-effective storage material for liquid sensible heat storage [49]. Liquid sensible heat storage can either use a two-tank solution or a one tank with thermoclines. The choice between the two is a trade-off between cost and performance: by using two tanks, the TES volume is doubled, and a constant discharge profile is guaranteed [49]. Besides pressurized water, also solid materials like rocks can be used as a solid sensible heat storage [56]. Latent thermal storage, on the other hand, is based on the absorption or release of heat during the phase change of a material, e.g. melting or solidifying of water or certain paraffin waxes. Finally, thermochemical storages are storing and releasing heat through chemical reaction mechanisms [23].

In the Compressed Heat Energy Storage for Energy from Renewable sources project [47], a hybrid type of thermal energy storage is researched. This is a combination of both latent and sensible thermal storage, filled with water. The latent storage tank is very well suited for the combination with subcritical ORC as evaporation and condensation happen isothermal [48]. In the sensible storage, 2 tanks are used: one hot tank and one cold tank. During charging, water is taken from the cold tank, heated by the heatsink from the HP and pumped to the hot tank. Opposite, during discharging, the water from the hot tank is pumped over the heat source of the

ORC, to the cold tank. To compensate for volume changes due to the varying water levels, both tanks are equipped with a nitrogen pressure control system, to keep the tank pressure above the saturation pressure. A schematic of this layout is shown in Figure 2.9

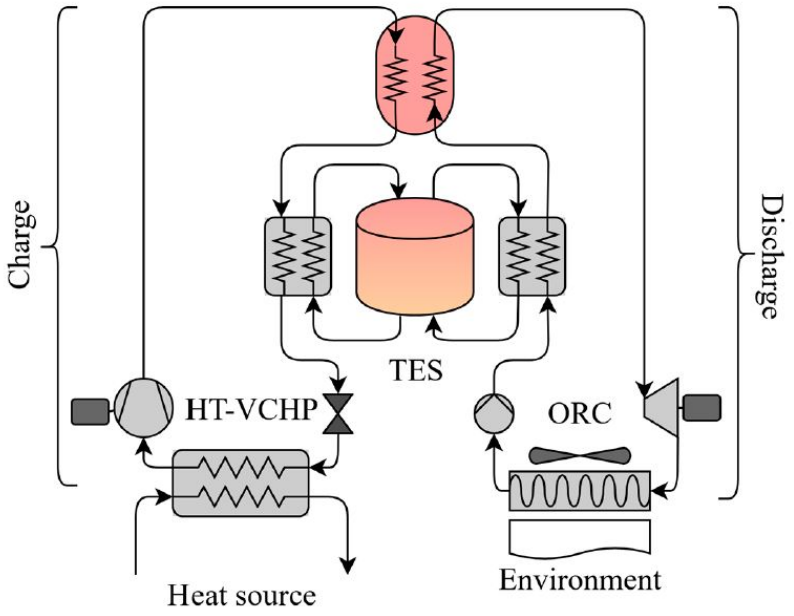

Figure 2.9: Hybrid latent (on top) and sensible (in the middle) TES, studied in [57], [58] and [24], (picture: [49])

However, in most cases, no latent storage is added to the system, only a sensible storage tank. Sometimes, the cold tank is even absent, this is often applied when the HP works between a low-grade heat source and the hot reservoir, so the cold reservoir cannot be "charged", and its role is then performed by the environment itself [32]. These tanks are often equipped with diffusers on the top and bottom, avoiding mixing and keeping the thermocline thickness as low as possible [6].

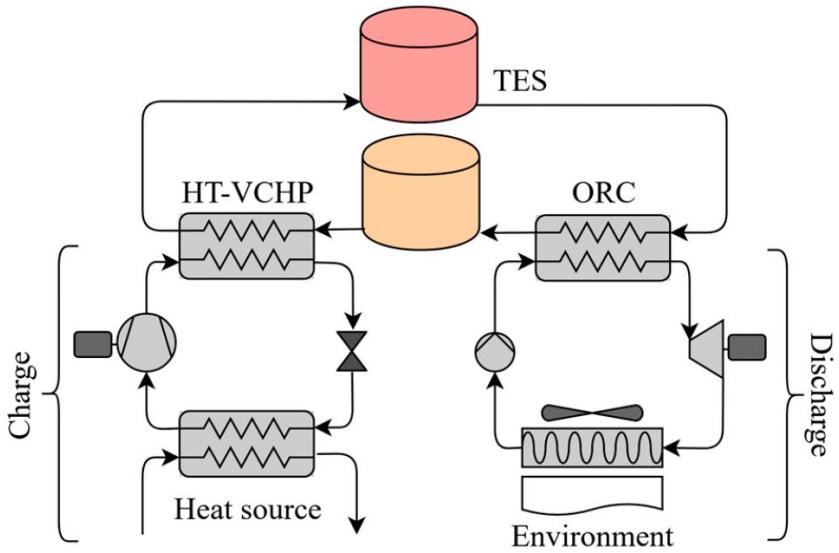

Figure 2.10: Topology with 2 sensible thermal energy storage tanks, studied in [25] and [32], (picture: [49])

2.10 Balancing services

In order to work properly, a power grid has to maintain a certain frequency (50 Hz or 60 Hz). How much the frequency deviates from the needed value depends on the correlation of power feed-in and consumption. If too much power is produced (or not enough consumed), the frequency rises. If not enough power is produced (or too many consumers need too much power), the frequency drops. Beyond a certain threshold (+/- 0.2 Hz), a blackout is imminent [20]. To avoid such a scenario, Transmission grid operators (TSO) deploy balancing energy. This balancing energy is a power-consuming or producing capacity that is added to or taken off the grid in case the frequency steers too far away from the stable level.

In the European Network of Transmission System Operators for Electricity (ENTSO-E) this balancing energy is often divided into different products, depending on how fast they have to react. They are called the Frequency Containment Reserve (FCR, R1, or primary control reserve), Automatic Frequency Restoration Reserve (aFRR, R2, or secondary control reserve), Manual Frequency Restoration Reserve (mFRR, R3, or tertiary control reserve) and Replacement Reserve (RR) [20].

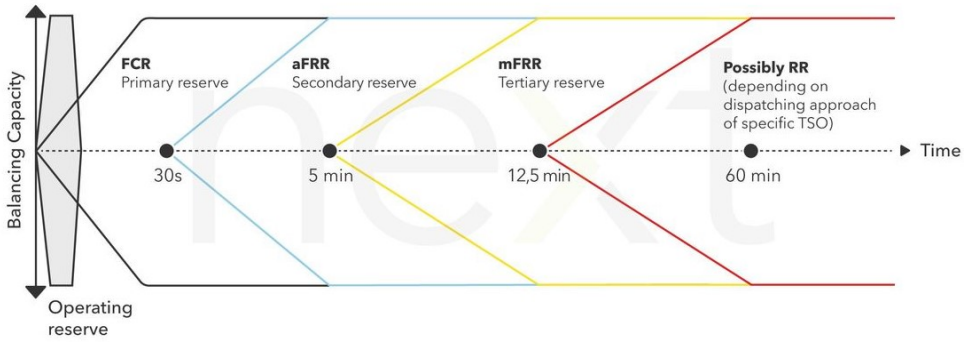

Figure 2.11: Balancing services according to the system envisaged by ENTSO-E [20]

As can be seen in Figure 2.11, FCR instantaneously balances out frequency deviations. Assets that provide FCR need to fully react within 30 seconds to the steering signals and cover a period of 15 minutes. In this case, it is not the TSO's signal that activates this product, but it correlates directly to the grid frequency, which is measured by the provider [20]. AFRR on the other hand is controlled centrally by the TSO and must be able to fully activate within 5 minutes (7.5 minutes according to Elia). After activation, the system operators send a new setpoint every 4 seconds, which must be followed within a strict accuracy band. This enables the grid operator to adjust the balance in a precise manner. Finally, mFRR must be able to be fully activated within 12.5 minutes (15 minutes according to Elia) and has a minimum duration period of 5 minutes. In case of larger imbalances, these reserves can support the frequency for minutes to hours [20].

In most countries, these balancing services are remunerated in two ways. The first one is the capacity availability remuneration: this is the fee to keep the capacity available to make adjustments when needed. The second one is the energy or activation remuneration: this is the compensation for the actual activation of the product by Elia and it is only paid for aFRR and mFRR.

In this thesis, the dynamic behaviour of heat pumps in Carnot battery systems will be researched. Depending on the dynamic performance, these heat pumps might be able to deliver balancing services to the grid. The capability of a system to deliver these balancing services can be tested

by standardized test profiles provided by Elia.

2.11 Dynamic behaviour

Delivering balancing services requires fast adaptation of the heat pump power uptake. However, most large-scale heat pumps that have been installed (e.g. for district heating), have been designed for baseload operation [50]. This section will focus on the dynamic behaviour of heat pumps (with thermal energy storage). Furthermore, the current limitations of heat pumps for balancing service applications will be discussed.

2.11.1 Limiting factors

According to experiences from Stockholm [59] and Gothenburg [60] in Sweden, it is technically feasible to use large-scale heat pumps for intra-day regulation, but the intermittent operation of heat pumps can be constrained by mechanical wear of the components, as well as several minutes start-up time and low COP during start-up [61]. However, large-scale heat pumps have not been optimised to react quickly to signals from the electricity grid. Accordingly, there is a lack of knowledge about the flexible operation of heat pumps as pointed out by [62].

Meesenburg et al. [50] optimized the control of a two-stage ammonia heat pump for fast regulation of power uptake. The authors stated that the compressors and valves have lower time constants than the rest of the system and can be modelled as steady-state components. This is due to the negligible mass and thermal inertia in comparison with those of the heat exchanger and tanks. The larger mass of the heat exchangers translates into noticeable inertia in the system. The steady-state model for the compression and expansion can be described either with performance curves given by the manufacturer or with algebraic correlations derived empirically [63]. Performance curves of the compressors are however often proprietary information of the manufacturers [64].

2.11.2 Dynamics and control

Usually, large-scale heat pumps are equipped with a control structure designed for high COPs in both full load and part load. They are not optimised for the flexible operation of the heat pump [50]. For instance, Hu et al. [65] focused on the control of heat pumps. The system was based on a transcritical CO_2 heat pump water heater and the control aimed to maximize the COP during changing operating conditions or water temperatures. This study however did not directly control the compressor power. So it does not provide much added value for balancing service applications.

Meesenburg et al. [50] is a study that focuses on fast dynamic control of heat pumps for the application in balancing services. The authors examined the control of a two-stage ammonia heat pump for fast regulation of power uptake. For this purpose, a dynamic model of this heat pump type with a variable speed piston compressor was implemented and validated against experimental data. This model was built in Dymola, using the TIL library [66]. Dymola is a simulation environment that enables the use of the modelling language Modelica [67]. It allows to write, compile and simulate physical models [66]. The study shows great similarities with the topic of this research and will be a major source of information for the development of the model for this research. It discusses the model development, the controls and discusses the exposed limitations.

The base system consisted of multiple controls of which a schematic overview can be found in Figure 2.12. The mass flow rate of the source was fixed, while the low-stage compressor (LS

comp.) controlled the evaporator outlet temperature on the source side and thereby indirectly the heat output and load of the heat pump. Secondly, the high-stage compressor (HS comp.) was set to control the intermediate pressure. This setup allows the compressors to change the load in line with each other. Next, the water mass flow rate through the condenser is controlled and thereby indirectly also the outlet temperature is controlled. Finally, the high-stage valve (HS valve) controlled the quality at the condenser outlet and the low-stage valve (LS valve) controlled the liquid level in the open intercooler.

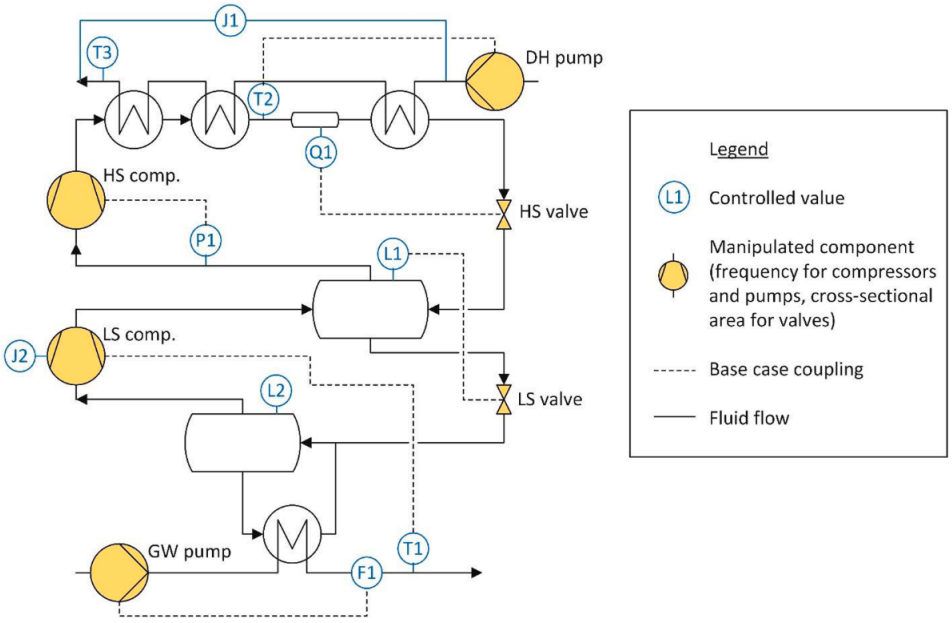

Figure 2.12: Sketch of the controllable values, the components that can be manipulated and the coupling of manipulated and controlled parameters for the base case scenario, with F - flow, P - pressure, T - temperature, L - liquid level, Q - vapour quality, J - Energy flow rate [50]

For the base case scenario, two limitations were identified that hinder the fast regulation of the heat pump. Firstly, the indirect control of the heat flow rate and thereby the power uptake, makes it more difficult to control the power uptake precisely. Moreover it induces a dead time in the load control, corresponding to the time until a change in compressor speed results in a temperature change at the evaporator outlet. Secondly, the condensation in the suction line during fast ramp down needs to be safely avoided in order to allow for fast ramping.

As a solution, a slightly adapted control was proposed, which would both minimise the risk for condensation in the suction line and allow for faster regulation of the heat pump. The new control proposed direct control of the compressor power uptake, instead of controlling the water outlet temperature of the evaporator. It was also shown that by controlling the low pressure via the source mass flow rate, the peak in evaporation pressure may be considerably reduced, which helps reduce the risk of condensation in the suction line. Even these measures could not completely ensure that no condensation would happen. Regardless of the reduced peak in evaporation pressure, the saturation temperature still increased suddenly, while the suction line walls are colder and therefore the risk of condensation could not be excluded.

To be sure that no condensation may occur, a preheating of the suction line is proposed. This may be done electrically or by means of another heat source. Altogether these measures avoided condensation and allowed regulation time of the heat pump power input from 250 kW to 175 kW in 85 s or from 250 kW to 100 kW in 140 s.

In a study by Dumont et al. [68], a model is made of a passive house with a solar absorber and a horizontal ground heat exchanger coupled with a HP/ORC unit. It also implements storage for excess heat from the solar roof. The paper studies among other topics, the time constants of the reversible HP/ORC unit, the solar roof, the storage and the house. This showed that the inertia of the unit could be neglected compared to the inertia of the house and the storage.

The previously mentioned studies show that it is important to consider all the time constants of a system that is being researched. Depending on the largest time constants, it might or might not be interesting to include the dynamics of the faster components. Since this thesis focuses more on the dynamics of the heat pump rather than the dynamics of the storage tank, the main interest goes towards the time constants in the heat pump. As mentioned before the time constants of the heat exchangers are significantly larger than those of the other components (e.g. valve and compressor), hence it should be a good approximation to approximate the dynamic behaviour of the heat pump with steady-state models for the compressor and the valve.

2.11.3 Dynamics of heat exchangers

Since heat exchangers are the components with the largest inertia in the system, it is of great importance to understand how they behave under variations in the flow. Most of the studies about plate heat exchangers focus on the steady state behaviour. The few papers that were available where with different liquids, different flow rates of different sizes. However, they can give an indication in the order of magnitude of the reaction time.

Dawery et al. [69] looked into the dynamic modeling and control of plate heat exchangers. The authors developed a general model and validated it with experimental data. The reaction of this model, to a step in the hot mass flow rate, showed that the final temperature was achieved after about 45 s. The size of this heat exchanger, however, is much smaller ($A = 0.627m^2$) compared to the intended size for this thesis research 3.4.2.

A more specific study about plate heat exchanger dynamics is presented by Shrihari et al. [70]. The authors provide a method to calculate a dimensionless time, based on Equation 2.5.

$$z = \frac{\tau}{\tau_{ra}} \tag{2.5}$$

where z is the dimensionless time [-], τ the time [s] and τ_{ra} the residence time in case of a uniform distribution [s], which is calculated using Equation 2.6.

$$\tau_{ra} = \frac{C}{\dot{w}_a} \tag{2.6}$$

In this equation, C represents the heat capacity of the resident fluid [J/K] and $\dot{w}_a$ is the thermal capacity rate of the fluid in the channel [W/K]. In the research, the outlet temperature typically reaches steady state when the dimensionless time is 7. As soon as the operating conditions of this research are further defined, these equations provide a way to verify the reaction time of the heat exchanger models developed in this research.

Furthermore some general conclusions about heat exchangers were found. In an older study by Aminan et al. [71], the authors stated that plate heat exchangers weigh 95 % less than comparable conventional shell-and-tube heat exchangers. This indicates that the lower thermal mass could result in faster transients compared to shell-and-tube heat exchangers. Research by Ghanim [72] also showed that the time constant of a plate heat exchanger is inversely proportional to the flow rate.

2.11.4 Static compressor and valve models

As explained before, only a static model is required for the compressor and the valve. The steady-state model for the compression and expansion can be described either with performance curves given by the manufacturer or with algebraic correlations derived empirically [63].

Liu et al. [73] build a dynamic model of a CO_2 heat pump coupled with hot and cold thermal storage using the TIL library in Dymola. This model was then used to test different dynamic optimal control strategies to optimize the charging of the hot and cold storage. In the paper, the authors state that the compressor is the critical component of the heat pump, as its performance has the largest impact on energy efficiency. Hence a compressor model was used, where the volumetric, isentropic and mechanical efficiency could be represented by an equation as a function of the pressure ratio. These relations were determined using previously found test data.

For the valve isenthalpic expansion is assumed, meaning that the specific enthalpy of the refrigerant remains the same through the expansion valve because of energy conservation: $h_{exp,in} = h_{exp,out}$. With: $h_{exp,in}$ and $h_{exp,out}$ the enthalpy at the valve inlet and outlet, respectively. From Bernoulli's law, Equation 2.7 can be derived. It calculates the mass flow rate as a function of the mass flow rate coefficient C_v, the pressure difference $p_{input} - p_{output}$, the through flow area of the orifice A and the density at the inlet ρ_{input} [74, 75]. The mass flow rate coefficient C_v is a function of the expansion valve's thermodynamic properties. The study of Wang et al. [76] shows an example of a correlation to calculate the flow coefficient.

$$m_{flow} = C_v A \cdot \sqrt{(p_{input} - p_{output}) \cdot 2 \cdot \rho_{input}} \tag{2.7}$$

2.12 Problem and goal statement

2.12.1 Research gap

Performing this literature study, revealed the knowledge gap concerning the dynamics of high temperature heat pumps. Most studies are focused on optimizing the heat exchangers, compressor, cycle topology, refrigerant, operating point, etc., to achieve the highest possible COP. To the author's best knowledge, only one study specifically tested and optimized a heat pump for balancing services. This research however only studied a two-stage ammonia heat pump. Moreover, the heat pump was not studied in the context of a Carnot battery. No other studies are observed that cover Rankine-based heat pumps with organic refrigerants, implemented in Carnot batteries, for the application in balancing services.

2.12.2 Conclusion

In this literature study, the ongoing research about Carnot batteries, high temperature heat pumps and its dynamic modelling has been discussed. It is clear that Carnot batteries might provide a part of the solution for large scale energy storage. Furthermore, it has exposed the possibility for high temperature heat pumps to deliver balancing services in the future.

Every aspect and component of the Carnot Battery has been discussed in this literature review. Starting with the heat exchangers, the compressor, the refrigerants and the storage tanks. Additionally, also the control and the sizing was discussed. Finally, an analysis was done about the available knowledge for the dynamics and the requirements to qualify systems as a provider for balancing services.

The entire model development of every heat pump component and the cycle model will be discussed thoroughly in the next chapter. Some questions still remain about the transient behaviour and dynamic modelling of heat pumps. Considering these questions, the objectives of the work are:

- Build a simple cycle dynamic model of a high temperature heat pump in Dymola
- Apply direct control of compressor power to the system
- Analyse its performance when varying the power demand
- Assess the performance of the dynamic model on test profile provided by Elia

Chapter 3

Model development

3.1 Approach

In this section, the approach of this analysis is presented. The research mainly focused on evaluating the dynamic performance of the heat pump in the Carnot battery system. The dynamics of the organic Rankine cycle on the other hand has been studied by Van De Velde et al. [77].

The steps that had to be taken to achieve the final goal are summed up below. First of all, based on the literature review the nominal operating point and an optimal refrigerant had to be selected. Secondly, the components of a basic heat pump (e.g. heat exchangers, compressor and valve) had to be selected to optimally fit the nominal operating conditions. This included the selection of the type, but also the sizing. Next, these components had to be modelled in Dymola. First, a static model was built and thereafter a dynamic model was constructed.

Once having a fully operational dynamic model, the control strategy was developed and tuned according to the dynamics of the system. Finally, the dynamic behaviour of the system was tested with the different prequalification tests from Elia. In Chapter 4, the results of these tests are evaluated to assess the performance of the system and to propose possible improvements for further research.

3.2 Nominal operating conditions and refrigerant selection

For the selection of a refrigerant, first, the nominal operating conditions have to be determined. This consists of the supply and return temperatures of the heat source and heat sink, the mass flow rates, the intended power...

A python script available on Github [78] was used to calculate this basic thermodynamic cycle, taking into account several input parameters. The required inputs are the condenser temperature, the evaporator temperature, the sink and source water input temperatures, the intended heat load, the pinch point temperature, the superheat in the evaporator, the subcool in the condenser, the isentropic efficiency of the compressor and the selected refrigerant. With these input values, the script calculates the pressure, temperature, quality and entropy of every point in the cycle. Furthermore, a visualisation of the cycle is shown in a Ts-diagram.

The assumed values are summarized in Table 3.1. Based on literature (balance between availability and higher COP), the water temperature of the waste heat was assumed to be 65 °C. The evaporator temperature, which is the temperature during evaporation of the refrigerant, was fixed on 50 °C. On the condenser side, the condensing temperature is fixed on 130 °C and the water temperature of the 'cold' water returning from the storage tank is fixed to 95 °C. Based

on the literature in section 2.6, the refrigerant R-1233zd(E) was suitable for these operating conditions. Furthermore, it is future proof, since it has a lower GWP and ODP than the most implemented refrigerants currently. The property data was imported from REFPROP [79].

Table 3.1: Nominal operating conditions: input python script

$T_{water,source,in}$ [°C]	65
$T_{water,sink,in}$ [°C]	95
T_{evap} [°C]	50
T_{cond} [°C]	130
ΔT_{SH} [°C]	9
ΔT_{SC} [°C]	4
Q_{cond} [MW]	2.8
ΔT_{evap} [°C]	5
ΔT_{cond} [°C]	5
η_s	0.8
Refrigerant	R-1233zd(E)

Also, the heat flow from the condenser to the water in the sink was fixed to 2.8 MW. This value was determined by trial-and-error to get an electric compressor power in the order of magnitude of 1 MW. The pinch point temperature of the evaporator and the condenser were both assumed to be 5K. Next, the amount of subcooling in the condenser was fixed to 4 °C. Whereas the superheat in the evaporator was fixed to 9 °C. In the first iteration, this superheat was chosen to be 4 °C. However, in the actual model, condensation occurred during compression. This can be explained by the relatively high isentropic efficiency and the overhanging bell curve in the Ts-diagram of the refrigerant, see section 2.6. Hence, the superheat had to be increased to 9 °C, leaving sufficient margin to avoid condensation. The subcooling is mainly required to avoid undesirable evaporation by pressure losses in the pipe following the condenser [80].

Figure 3.1, shows the Ts-diagram of the cycle calculated by the python script. The blue and red lines represent the water temperatures in the heat exchangers and the green line represents the states of the refrigerant.

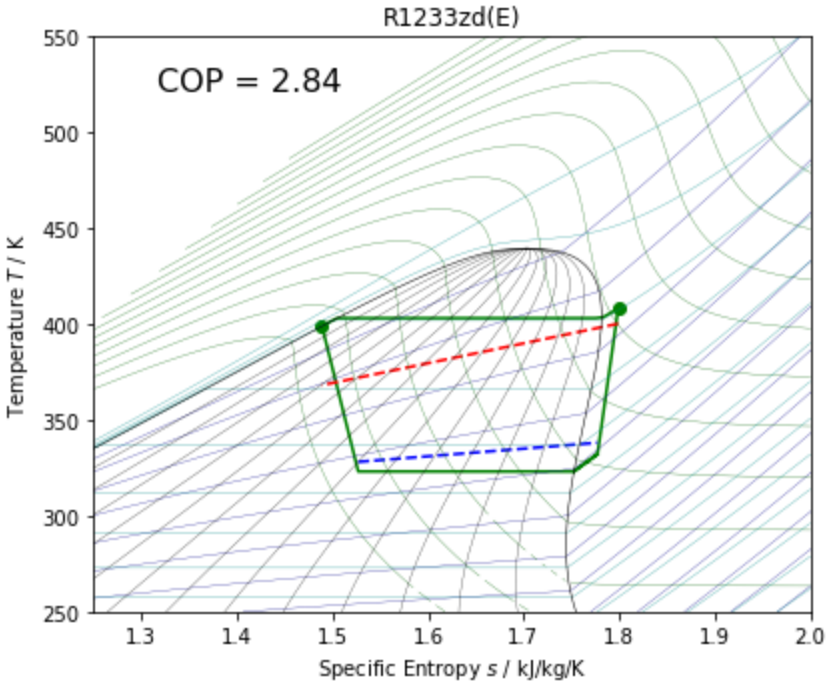

Figure 3.1: Ts-diagram of the cycle in nominal operating conditions

Running the script calculates the pressures in the evaporator and condenser, the pressure ratio, the COP, the mass flow rates, the heat flows and the electrical power of the compressor. These values are later on used as a base for sizing the actual heat exchangers, valve and compressor.

Table 3.2: Nominal operating conditions

p_{low} [bar]	2.93
p_{high} [bar]	19.08
PR [-]	6.5
$\rho_{refr,comp,in}$ [kg/m^3]	15.1
COP [-]	2.84
$\dot{m}_{water,source}$ [kg/s]	43.4
$\dot{m}_{watersink}$ [kg/s]	20.7
$\dot{m}_{refr}$ [kg/s]	22.4
Q_{evap} [kW]	1814
Q_{cond} [kW]	2800
$P_{el,comp}$ [kW]	986

3.3 System layout

Here I will shortly introduce the cycle and the components, as an introduction for the next sections.

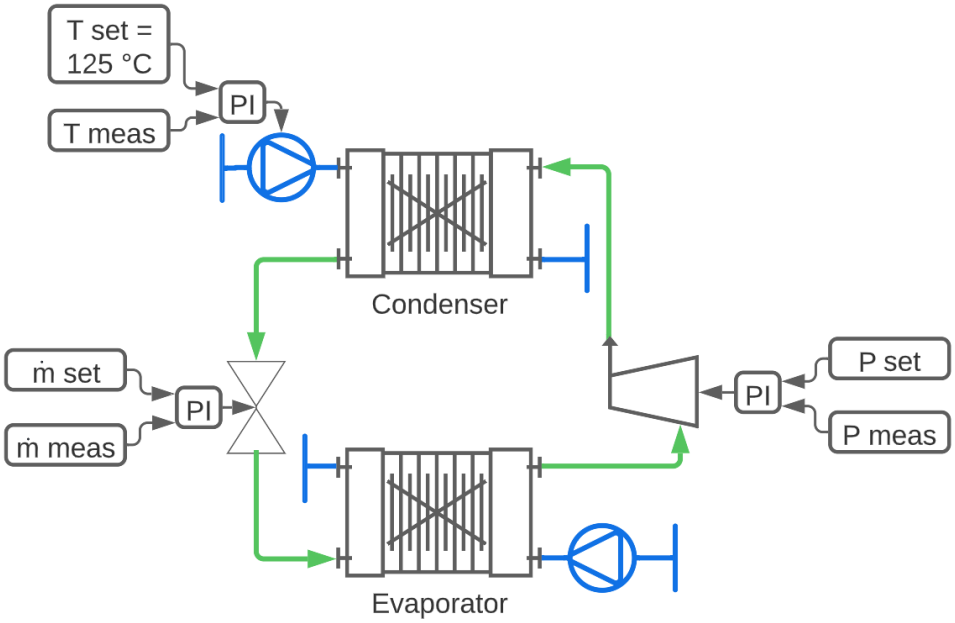

Figure 3.2: Schematic representation of complete cycle

3.4 Heat exchangers

3.4.1 Introduction

For a simple cycle heat pump, two heat exchangers are required. One condenser and one evaporator. Both heat exchangers are conducting heat between the refrigerant and water. The temperatures, mass flows, pressures and qualities required for the heat exchanger selection are based on the calculations in python. For clarity, these parameters are summarized in the tables below 3.3:

Table 3.3: Input parameters for heat exchanger selection

$T_{water,source,in}$ [°C]	65
$T_{water,source,out}$ [°C]	55
$T_{refr,in}$ [°C]	50
$T_{refr,out}$ [°C]	59
$q_{evap,in}$ [-]	0.36
$q_{evap,out}$ [-]	1
Q_{evap} [kW]	1814
$\dot{m}_{water}$ [kg/s]	43.4
$\dot{m}_{refr}$ [kg/s]	22.4

(a) Evaporator

$T_{water,sink,in}$ [°C]	95
$T_{water,sink,out}$ [°C]	127
$T_{refr,in}$ [°C]	135
$T_{refr,out}$ [°C]	126
$q_{cond,in}$ [-]	1
$q_{cond,out}$ [-]	0
Q_{cond} [kW]	2800
$\dot{m}_{water}$ [kg/s]	20.7
$\dot{m}_{refr}$ [kg/s]	22.4

(b) Condenser

The TIL library in Dymola includes heat exchanger models of several different types: fin-and-tube, multiport extruded tubes, plate, shell-and-tube and tube-and-tube. Based on the literature review in section 2.8 the shell-and-tube and the plate heat exchangers are the two most suited types for these large scale industrial heat pumps.

Both the shell-and-tube heat exchanger (STHE) and the plate heat exchanger (PHE) model in Dymola contain fully customizable geometries, such that the model can be adapted to the desired sizing. In every model, different types of heat transfer and pressure drop correlations can be

selected. However, the heat transfer correlations in the STHE were only based on constant heat transfer coefficients, while the heat transfer correlations in the PHE were more elaborate. Due to the more accurate heat transfer correlations, the faster dynamics and various other arguments mentioned in section 2.8, the PHE was selected for this high-temperature heat pump application. In Section 3.4.2 the sizing of the heat exchangers according to the operating conditions in Table 3.3 are presented.

3.4.2 Sizing

High-level sizing of a PHE can be performed using basic analytical expressions, however, specialized manufacturers provide online software that facilitates this process. Examples of these manufacturers are SWEP [81] and AlfaLaval [82].

The sizing was based on the SSPG8 software provided by SWEP [81], it takes the input of all operation variables and matches it with the best fitting PHE. It is also possible to incorporate a certain percentage of oversizing. The proposed/default safety factor of 20% was selected.

The software proposed the following heat exchangers:

Table 3.4: Heat exchanger sizing from SWEP software

Type	VH500TM
Heat transfer area [m^2]	454
Number of plates	$5 \cdot 306 = 1530$
Mass [kg]	1639
Hold-up volume (refr) [l]	$5 \cdot 87 = 435$
Hold-up volume (water) [l]	$5 \cdot 87 = 435$

(a) Evaporator

Type	B500TM
Heat transfer area [m^2]	149
Number of plates	$2 \cdot 252 = 504$
Mass [kg]	488
Hold-up volume (refr) [l]	$5 \cdot 72 = 360$
Hold-up volume (water) [l]	$5 \cdot 72 = 360$

(b) Condenser

Also, the basic dimensions are returned by the software:

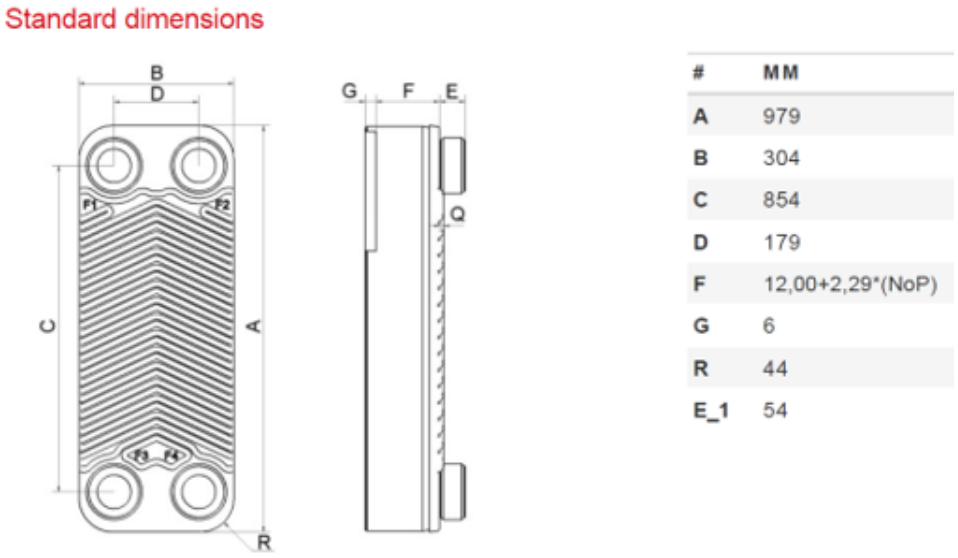

#	MM
A	979
B	304
C	854
D	179
F	12,00+2,29*(NoP)
G	6
R	44
E_1	54

Figure 3.3: SWEP software: evaporator and condenser with the same basic dimensions

Besides the dimensions in Figure 3.3, the models in Dymola require more geometric parameters like the wall Thickness (t), the pattern angle (ϕ), the pattern amplitude (a) and the pattern

wavelength (λ), as shown in Figure 3.4. These parameters were not provided by the manufacturer, so an initial guess was based on the paper from Meesenburg et al. [50]. Afterwards, these values have been adjusted to match the weight, the total heat transfer area and the internal volume of the Dymola model and the heat exchanger dimensioned in the SWEP software. In the evaporator, the following values were chosen $\phi = 60°$, $t = 0.45$ mm, $a = 1.1$ mm and $\lambda = 8.8$ mm. The condenser used: $\phi = 30°$, $t = 0.41$ mm, $a = 1.1$ mm and $\lambda = 8.8$ mm [50, 82]. With these values implemented in Dymola, the resulting mass, volume and heat transfer area are compared in Table 3.5. The good correspondence increases the confidence in the modelled geometry compared to the actual geometry of both the evaporator and the condenser.

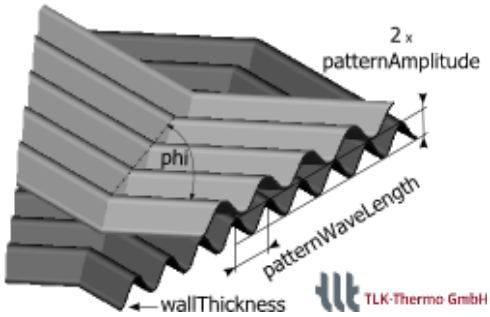

Figure 3.4: Plate heat exchanger geometry of waves [66]

Table 3.5: Comparison of mass, volume and heat transfer area of the Dymola model and the proposed sizing by the software from SWEP

	Evaporator SWEP	**Evaporator Dymola**
Mass [kg]	1639	1631
Volume [l]	$5 \cdot 87 = 435$	437
Heat transfer area [m^2]	454	453

(a) Evaporator

	Condenser SWEP	**Condenser Dymola**
Mass [kg]	488	490
Volume [l]	$2 \cdot 72 = 144$	144
Heat transfer area [m^2]	149	149

(b) Condenser

3.4.3 Dynamic model

In the TIL library, some dynamic models are already included for plate heat exchangers. These models are based on the finite volume method or the moving boundary method. Wei et al. [83] compares the two modelling techniques in terms of accuracy, complexity and simulation speed to simplify the decision in future research. The authors studied the evaporator and condenser in an ORC. In the following paragraphs, the modelling techniques are shortly introduced.

Both the evaporator and condenser can be described as composed of three zones characterized by sub-cooled liquid, saturated mixture and superheated vapour (Figure 3.5). The length of every zone in the evaporator or condenser depends on the operating conditions of the heat exchangers, hence the name moving boundary model. For each zone, appropriate one-dimensional governing equations can be derived. These zones can be observed in an evaporator since the refrigerant, in the sub-cooled liquid phase, evaporates and exits as superheated vapour. Conversely, the

condenser is characterized by entering superheated vapour and either leaving saturated liquid or a mixture of vapour and liquid with a small quality [83].

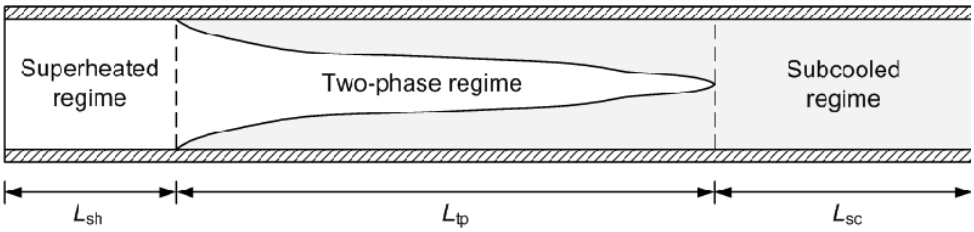

Figure 3.5: Moving boundary model

In the case of a discretized model, the heat exchanger and the governing equations for mass, momentum and energy are spatially discretized along the fluid flow direction and this discretization is constant over time [83]. The discretization can be executed using either a finite volume or a finite difference method. The governing equations are then solved for each discretized cell [63]. Both models correctly simulate the behaviour of the system during transients, without showing numerical oscillations.

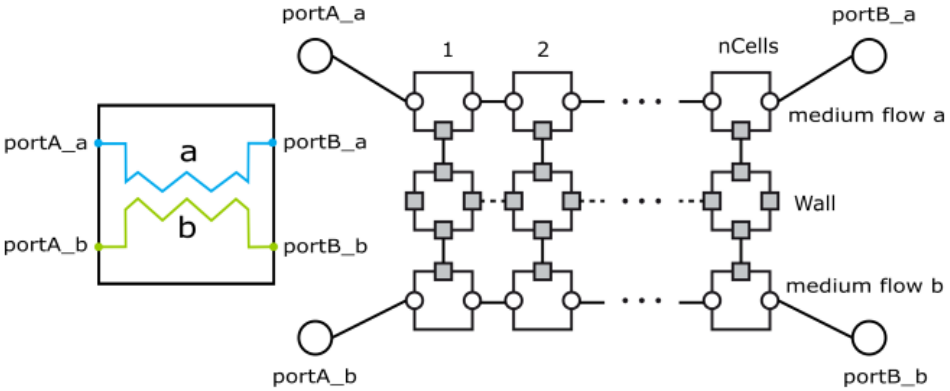

Figure 3.6: Discretized model [66]

According to Wei et al. [83], the discretized model as well as the moving boundary model show good accuracy of the ouputs compared to experimental data. Moreover, the moving boundary model is faster and therefore more suitable for control design applications. Examples of studies where the discretization methods have been used to dynamically model heat exchangers are [50], [68], [84] and [85]. Moving boundary models on the other hand have been implemented in [63] and [86].

In this research, a discretized model is selected in Dymola. It appeared to have several advantages compared to the moving boundary model. First of all, it was easier to include a pressure drop model. Secondly, it was less sensitive to the initialization values. Finally, the additional computation time was limited for heat exchangers with 10 cells. A more thorough motivation for the number of cells is provided in the sensitivity analysis in section 3.10.

3.4.4 Pressure drop

As mentioned before, pressure drop models are available in the TIL library for the heat exchanger. In this research the '*QuadraticMassFlowDependent*' pressure drop is selected [66].

The model requires a nominal pressure drop at a nominal mass flow rate. Other pressure drops are calculated starting from this nominal point, while following a quadratic curve. As a consequence, the accuracy of the calculated pressure might decrease for larger deviations of the mass flow rate, compared to the nominal operating point. The nominal pressure drop and mass flow rate are provided by the SWEP software and are summarized in Table 3.6.

Table 3.6: Pressure drop at nominal conditions

	Evaporator	**Condenser**
Δp_{water} [bar]	0.03	0.05
Δp_{refr} [bar]	0.25	0.28

Since a quadratic dependence is estimated, this model is valid for turbulent flow states, described by Reynolds numbers higher than 2300. This conditions is satisfied for the refrigerant. However, on the water side, $Re_{evaporator}$ is 801 and $Re_{condenser}$ is 2156. In the evaporator this is not a problem, since the mass flow rate is assumed to be constant, hence the pressure drop is also constant. In the condenser the condition is indeed not satisfied and the calculated pressure drop can be inaccurate. Even though the condition is not met, the effect on the results is expected to be very limited since water is an incompressible fluid. This final statement is verified in section 4.2

3.4.5 Heat transfer correlations

Heat transfer between the fluids can be defined using different correlations. The TIL library already provides the numerically optimized models, to calculate the heat transfer for a variety of different transport tasks. The heat transfer is divided into two main categories. First is the constant fluid transport phenomena, which are based on a fixed value for the heat transfer coefficient. In this case, the heat flow is only influenced by the geometry and the related temperature difference: $Q_{dot} = \alpha \cdot A \cdot (T_1 - T_2)$. On the other hand, more advanced correlations are available, optimized for more specific cases. For the liquid side in a PHE, TIL proposes the VDI Plate Alpha, based on the equations presented in the VDI Heat Atlas [87]. For the refrigerant side, Shah Chen and Gnielinski Dittus Boelter are proposed.

VDI plate alpha

The VDI plate alpha correlation is only for one phase fluids. This model uses a friction factor in order to calculate the coefficient of heat transfer of chevron plate heat exchangers. The friction factor is considered in the (ζ) value, whose basic equations are listed in the pressure drop model by the approach of the "VDI Heat Atlas". The parameters of the geometry, which are used for the calculation, are illustrated in Figure 3.4.

$$Nu = 0.122 Pr \cdot \left(\frac{1}{3}\right) \cdot \left(\frac{\eta_{fluid}}{\eta_{wall}}\right)^{1/6} \cdot (\zeta \cdot Re^2 sin(2\phi))^{0.374} \tag{3.1}$$

With η_{fluid} and η_{wall} the dynamic viscosity of the bulk fluid or of the fluid at the wall, Re the Reynolds number, ϕ the angle of the pattern and Pr the Prandtl number.
The validity of this correlation is restricted to:

- Plate heat exchangers with wavy pattern geometries
- Geometries with a ratio of the pattern wavelength/pattern amplitude between 4 and 8
- A change of the heat transfer coefficient due to evaporation or condensation is neglected
- Reynolds number between 90 and 30 000

The model that is being built in Dymola indeed is within the restrictions of the correlations. The geometry is wavy, the ratio of the wavelength and the pattern amplitude will also be kept within the boundaries and the heat transfer will all be in the liquid phase. Finally, the Reynolds numbers on the liquid side are estimated in the software from SWEP. The estimated values are 801 in the evaporator and 2156 in the condenser.
Further information about the correlations can be found at [87].

Shah Chen and Gnielinski Dittus Boelter

In order to describe the heat transfer of a VLEfluid during evaporation, condensation and in a single-phase state the Shah Chen and Dittus Boelter correlations can be used. This model uses three different correlations, as shown in Table 3.7, which are merged using linear transition.

Table 3.7: Heat transfer correlations for the refrigerants

One phase	**Two phase**	
Gnielinski Dittus Boelter	**Evaporation**	**Condensation**
	Shah Chen	Shah

Gnielinski Dittus Boelter is the implementation of the correlation by Gnielinski, Dittus and Boelter, describing the heat transfer of a one-phase medium, for a variety of tube-like geometries. Corresponding to the properties of the fluid flow, represented by the Reynolds number (Re), three different equations are distinguished. One for laminar flow, one for the transition area and the third one for turbulent flow. A smooth transition between the equations is achieved by the usage of a transition function.

$$Nusselt = \begin{cases} 3.6568 & Re < 2300 \ (Laminar) \\ \frac{\left(\frac{\zeta}{8}\right)(Re-1000)Pr}{1+12.7\cdot\sqrt{\frac{\zeta}{8}}\left(Pr_3^2-1\right)} & 2300 < Re < 100000 \ (Gnielinski) \\ 0.023\cdot max(Re, 1E-12)^{\frac{4}{5}} Pr^{\frac{1}{3}} & Re > 100000 \ (DittusBoelter) \end{cases} \tag{3.2}$$

$$\zeta = (0.79\cdot ln(max(Re, 1E-12)) - 1.64)^{-2} \tag{3.3}$$

The correlations of Gnielinski Dittus Boelter are restricted to:

- One-phase mediums
- Inner diameter of the tube (d) $\leq$ length (l)
- $0.1 \leq$ Pr ≤ 1000 for the transition area

The Prandtl number can be calculated by:

$$Pr = \frac{\mu \cdot c_p}{k} \tag{3.4}$$

With:

Table 3.8: Check for Prandtl number restriction

		Evaporator	**Condenser**
μ [Pa s]	Dynamic viscosity	2.18E-04	9.42E-05
c_p [kJ/(kgK)]	Specific heat	1.268	1.646
k [W/(mK)]	Thermal conductivity	0.0745	0.0546
Pr [-]	Prandtl number	3.7	2.8

Indeed the values for the Prandtl number are within the restrictions.

Baehr et al. [88], provides further information about the correlations. Important to notice is that the Gnielinski Dittus Boelter, as well as the Shah and the Shah Chen correlations, are designed for tubular structures. However, plate heat exchangers have corrugated plates, rather than tubular structures. The TIL library does propose these correlations for plate heat exchangers and the other requirements are met. Therefore, it is assumed that these correlations also provide representative results for plate heat exchangers. In section 4.2 the resulting heat transfer coefficients are verified.

Next, the Shah Chen heat transfer correlation describes the heat transfer during convective boiling and evaporation of refrigerants. Since the Froude number compares the inertial and gravitational forces, its value is used to rate the influence of the gravitation and therefore distinguishes between the two approaches. For small Froude numbers (<0.04), the approach from Shah is used, whereas for larger Froude numbers (>0.04) the approach of Chen is used. The Froude number is defined by Equation 3.5.

$$Fr = \frac{m_{flow}^2}{A^2 \rho^2 g d_{hyd}} \tag{3.5}$$

with m_{flow} the mass flow in $\frac{kg}{s}$, A the through flow area m^2, ρ the density of the fluid in $\frac{kg}{m^3}$, g the gravitational constant $\frac{N}{kg}$, and d_{hyd} the hydraulic diameter in m.

The correlation by Chen uses a coefficient for both convective boiling (α_k) and for bulk boiling (α_B), to calculate the coefficient of heat transfer corresponding to the state of the fluid. This approach is only valid for flows in vertical tubes.

Chen (Fr>0.04):

$$\alpha = S \cdot \alpha_B + F \cdot \alpha_k \tag{3.6}$$

with

$$\begin{aligned} \alpha_b &= F(\frac{p}{p_{crit}}, q_{dot}) \\ \alpha_k &= \frac{\lambda_{liquid}}{h_{hyd}} \cdot 0.023 \cdot Re^{0.8} Pr^{0.4} \end{aligned} \tag{3.7}$$

The correlation of Shah for evaporation uses different equations to calculate the bulk boiling coefficient, based on the boiling coefficient (BO), the value of N (as defined in [89]), the Froude number and the properties of the vapour and liquid phase. The overall heat transfer coefficient is set by the larger one of the two coefficients. This correlation is adapted for both vertical and horizontal geometries [90].

Shah (Fr<0.04):

$$\alpha = max(\alpha_b, \alpha_k) \tag{3.8}$$

with

$$\begin{aligned} \alpha_b &= F(Bo, N, \alpha_{liquid}) \\ \alpha_k &= \frac{1.8}{N^{0.8}} \cdot \frac{\lambda_{liquid}}{h_{hyd}} \cdot 0.023 \cdot Re^{0.8} Pr^{0.4} \end{aligned} \tag{3.9}$$

More information about the used correlations can be found in [91].

Finally, the heat transfer correlations for condensation by Shah will be discussed. The resulting equations are as follows:

$$\begin{aligned} \alpha &= \alpha_{liquid}\left((1-x)^{0.8} + \frac{3.8x^{0.76}(1-x)^{0.04}}{p_{reduced}^{0.38}}\right) \\ \alpha_{liquid} &= \frac{0.023 \cdot Re^{0.8} Pr^{0.4} \lambda_l}{d_{hyd}} \\ p_{reduced} &= \frac{p}{p_{crit}} \end{aligned} \tag{3.10}$$

Shah, the author of [92] stated a range in which the use of the Shah correlation is recommended. Some of the requirements can be checked immediately. For others, some assumptions have to be made. The requirements are shown in Table 3.9.

Table 3.9: Requirements for Shah heat transfer correlations [92]

Parameter	**Recommended range**	**Evaporator**	**Condenser**
Flow channel	Pipes, annuli	Plate channels	Plate channels
Flow direction	All directions	✓	✓
Pipe inner diameter [mm]	7 - 40	/	/
T_{sat} [°C]	21 - 310	50	130
Quality [–]	0 - 100%	✓	✓
Heat transfer [W/mˆ2]	All values	✓	✓
Mass flux [kg/m²h]	39 000 – 5 758 400	157 543	478 254
p [MPa]	0.07 – 9.8	0.29	1.9
$p_{reduced}$[–]	0.002 – 0.44	0.081	0.526
Re_L in pipes	350 and higher	773 in channel	5426 in channel
w of vapour [m/s]	3 – 300	3.13	1.31
Pr_l	>0.5	3.7	2.8
Flow patterns	All	✓	✓

Most variables fall within the recommended range stated by the authors, but not all. The velocity of the refrigerant in the condenser is lower than the minimum value. In the condenser, the reduced pressure also turned out to be slightly larger than the recommended range.

The calculation of Re_L is clarified below. Re_L is the Reynolds number if all mass is flowing as a liquid. Since the tube diameter cannot be used as the characteristic length, a different definition for the Reynolds number is used. The definitions can be found in [53] and is based on the hydraulic diameter as the characteristic length.

The required equations to calculate the Reynolds number are represented below:

$$\begin{aligned} Re &= \frac{d_h \cdot w}{\nu} \\ d_h &= \frac{4a}{\phi} \\ \phi &= \frac{1}{6}(1 + \sqrt{1+X^2} + 4\sqrt{1+X^2/2}) \\ X &= \frac{2\pi a}{\lambda} \end{aligned} \tag{3.11}$$

where ν is the kinematic viscosity, w is the velocity in the channels, d_h is the hydraulic diameter, a is the amplitude of the corrugations, ϕ is the area enlargement factor, X is the dimensionless

corrugation parameter and λ is the wavelength of the corrugation pattern. Since Re_L is required, the velocity is calculated for the refrigerant in a liquid state. The equations yield 773 and 5426 respectively for the evaporator and condenser. These values are both larger than 350, so the requirement is met.

3.5 Compressor

3.5.1 Introduction

In this section, the selection of the compressor type and the development of the compressor model in Dymola is discussed. Figure 3.7 shows an overview of different compressor technologies that are currently available.

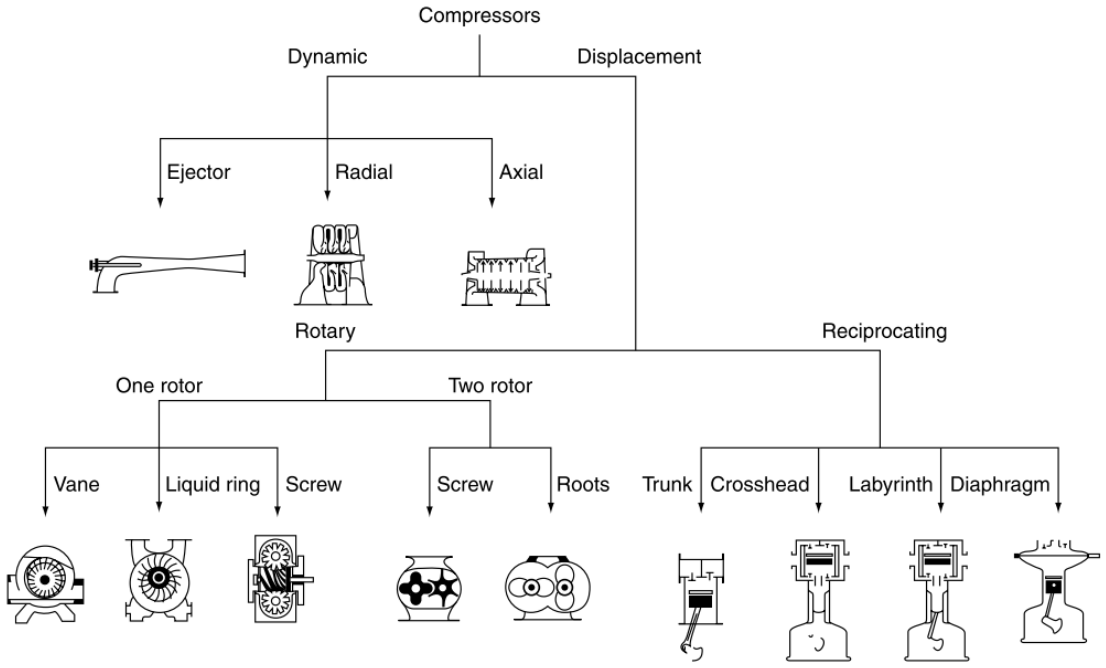

Figure 3.7: Overview of compressor types [93]

As mentioned before, the compressor technology can now be selected based on the calculated nominal operating conditions. According to the calculations of the intended operating conditions, a volume flow rate of 1.48 $m^3/s \approx 89\ m^3/min \approx 3142\ acfm$ (actual cubic feet per minute) is found. Projecting this value on Figure 2.8 shows that rotary-screw and centrifugal single or multi-stage compressors are suitable. Multi-stage reciprocating compressors fall just short of this proposed volume flow rate, however, multiple compressors can be placed in parallel to increase the achievable volume flow rate. Axial compressors are not presented on the chart, however, literature presents typical volume flow rates in the order of 2000 m^3/min up to 20 000 m^3/min [94]. Compared to the intended flow rate of 89 m^3/min, these axial compressors provide too high volume flow rates. Next, some of the most suitable compressor types, based on Figure 2.8 and based on practical examples are discussed.

Screw compressor

A screw compressor is a rotary compressor which works on the positive displacement principle. It will continue to move the same volume of gas per rotation, regardless of gas density and downstream pressure. They come in different variations, namely oil-free (dry) or oil-injected

(flooded or wet) [95]. An advantage of screw compressors is that they maintain high efficiency across a broad range of conditions. Screw compressors also do not have any valves, which allows operation at high speeds with large flow rates and a small footprint, while also reducing vibrations [96]. According to Figure 2.8 these flow rates can be up to 850 m^3/min. One downside is the efficiency, which can be slightly lower than for instance radial compressors. According to [97] the overall compressor efficiencies of a screw compressor are 0.65 - 0.75.

Reciprocating compressor

In reciprocating compressors flow rates up to 85 m^3/min are achievable (Figure 2.8). In the past, these were also used in applications with very low cooling capacities due to their low costs. However, they have progressively been replaced by rotary compressors. This is mainly due to their high maintenance, noise, vibrations and low efficiency compared to other compressors [98, 99].

Axial compressor

The axial compressor is a type of dynamic compressor, where the gas flows in the axial direction. It typically consists of multiple stages, where each stage is formed by a row of stator and rotor vanes. They are typically used for applications where compactness and very high flow rates are needed. According to Fioravanti et al. [94] the flow rates are in the order of 2 000 m^3/min to 20 000 m^3/min.

Centrifugal or radial compressor

Centrifugal compressors pressurize a refrigerant by forcing the flow through a rotating impeller. Unlike axial compressors, the flow leaves the rotor in a radial direction, after which it is guided through a diffuser. They are well suited for compressing large volumes of refrigerant. According to Figure 2.8 the inlet flow rate can reach up to about 200 000 actual cubic feet per minute (acfm) or 5663 m^3/min. Similar to axial compressors, centrifugal compressors can be set up in multi-stage configurations to further compress the refrigerant to a higher pressure and temperature, based on the application requirements [98]. Typical overall efficiencies are 0.70 - 0.85, according to [97].

In conclusion, a screw compressor seems to be the most interesting option for several reasons. First of all, it is a volumetric compressor, hence in part load, similar pressure ratios can be achieved for lower mass flow rates by decreasing the rotational speed. Furthermore, it has the capability to increase the scale to high flow rates up to 850 m^3/min. However, if more emphasis is on efficiency in nominal conditions, also a radial compressor can be selected.

3.5.2 TIL models

In the TIL library, two compressor models of reciprocating compressors are already available. The 'EffCompressor' is defined by the rotational speed (n), the displacement volume (V_{disp}) and three fixed efficiencies ($volEFF$, $isEFF$, $effIsEff$). This model is widely applicable due to its simplicity. The second model 'ReciprocatingCompressor' is more elaborate and takes into account many different physical losses. For instance, it takes into account friction losses (quadratic with the rotational speed), the reexpansion of the dead space volume and a discharge delay, regarding the delayed valve closing at high speeds. Furthermore, a heat flow rate from the discharge chamber is calculated, considering ambient heat losses. This model requires more specific input parameters like the relative dead space, the discharge valve delay, the friction coefficient and the areas of the suction valve and the discharge valve. These values are however often proprietary information of the manufacturers. Hence this model is not usable for this research

unless a complete set of data is retrieved for a compressor suited for the intended operating conditions.

The 'EffCompressor' could be used to model a reciprocating compressor and even a screw compressor. It can also be extended by implementing curves that describe the efficiency as a function of the pressure ratio. This allows modelling the decreased efficiency when operating in part-load.

Besides volumetric compressors, also dynamic compressors have shown to be interesting for this large-scale high-temperature heat pump. Dynamic compressor models are however not included in the TIL library. Therefore, a model still has to be developed if a dynamic compressor is desirable.

3.5.3 Performance map

In this research, the compressor often runs in part-load. Hence, the compressor model definitely has to include the changing efficiencies when changing the operating point. Considering the size analysis based on Figure 2.8, a screw compressor, reciprocating compressor or centrifugal compressor would be selected. However, the model in Dymola requires sufficient data points to construct proper performance curves. Since data for compressor performance maps are often proprietary information of the manufacturers, few applicable curves were found to model the compressor. Certainly, for refrigerant compressors data was scarce. The most complete set of data was found for an axial turbine. Although this was not the selected compressor, it does allow for the creation of a quasi steady-state compressor model of a dynamic compressor. The model will be constructed such that different performance curves can be implemented when other data is available.

The compressor map was retrieved from the GasTurb map collection [100]. GasTurb is a gas turbine performance calculation and optimization program. It simulates most of the gas turbine configurations in use for propulsion or for power generation. Part of the software is the Smooth C program, which can be used to quickly generate high-quality compressor maps from measured or published data. This software also comprises a series of 58 compressor maps, however, only a small selection is available in the trial version. Based on the design parameters in Table 3.2, the compressor map with a mass flow rate and pressure ratio closest to the intended operating conditions was selected from the software (Figure 3.8).

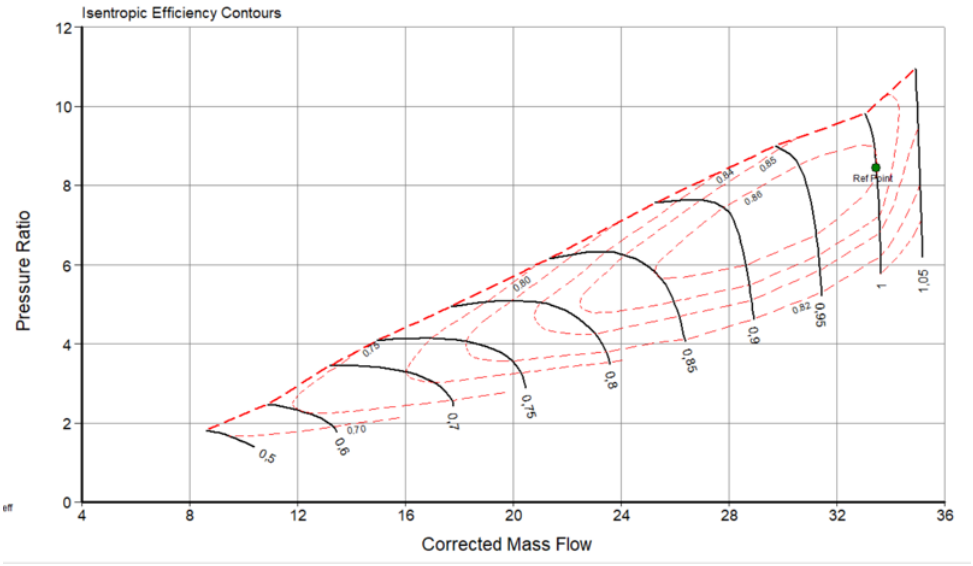

Figure 3.8: Compressor map Gasturb [100]

The compressor has a nominal mass flow rate of 33.5 kg/s and a nominal pressure ratio of about 8.5. Whereas the intended operating conditions with the refrigerant (Table 3.2) are a mass flow rate of 22.4 kg/s and a pressure ratio of 6.5.

Given the map and the limited available data, some assumptions had to be made. First of all, it is assumed that the curves of an air compressor are also representative for a refrigerant compressors. Secondly, it is assumed that the compressor map can be scaled to lower mass flow rate and pressure ratio, by multiplying both axes with a certain factor. Normally these assumptions do not hold, since refrigerants have a different heat capacity ratio. They can, however, provide an indication of how a refrigerant compressor would behave.

3.5.4 Model development

Since no model of a dynamic compressor is included in the TIL library, a new model had to be constructed. This model was based on the 'EffCompressor' model in Dymola, which is a reciprocating compressor. The new model includes data tables for the implementation of the efficiency and mass flow map of the compressor. Also the equations were adapted to implement the values retrieved from the tables instead of the efficiencies that are normally inputted by the user interface. These data tables, however, had to be entered in a different shape than how it was provided by the GasTurb software. Hence some adaptations had to be done to the given data.

Mass flow rate

The data was converted to the required shape and some adjustments were made to avoid inconsistencies during the simulations in Dymola. In Figure 3.9, a comparison is shown between the original and the final compressor map.

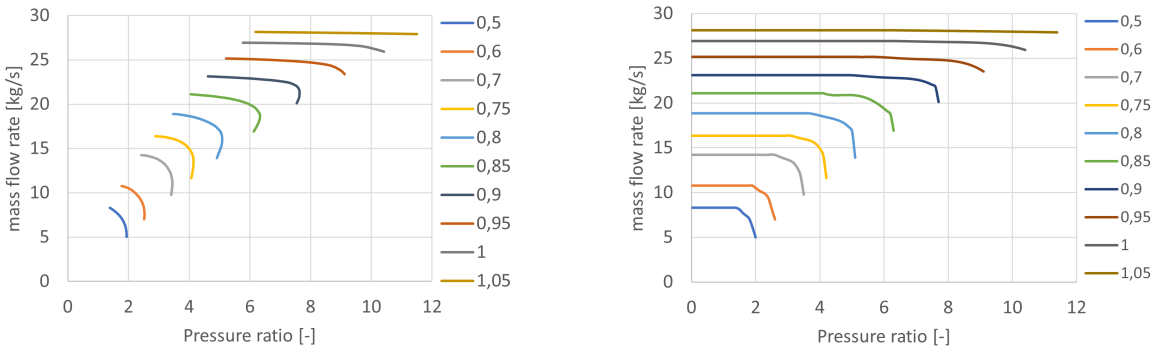

(a) Original (b) Adapted

Figure 3.9: Comparison of original and adapted compressor map

Efficiency

Also, the efficiency was provided in a form that cannot be implemented in Dymola. Hence, similar modifications are performed as for the mass flow maps. In order to make the solving process more redundant, zeros are avoided in the table by extending the efficiency curves horizontally. Finally, the modified data in Figure 3.10 is obtained. It is clear that having these high efficiencies outside the operating curves is not physical. However, this is only implemented for stability during initialisation and the model should never be working outside the intended operating curves.

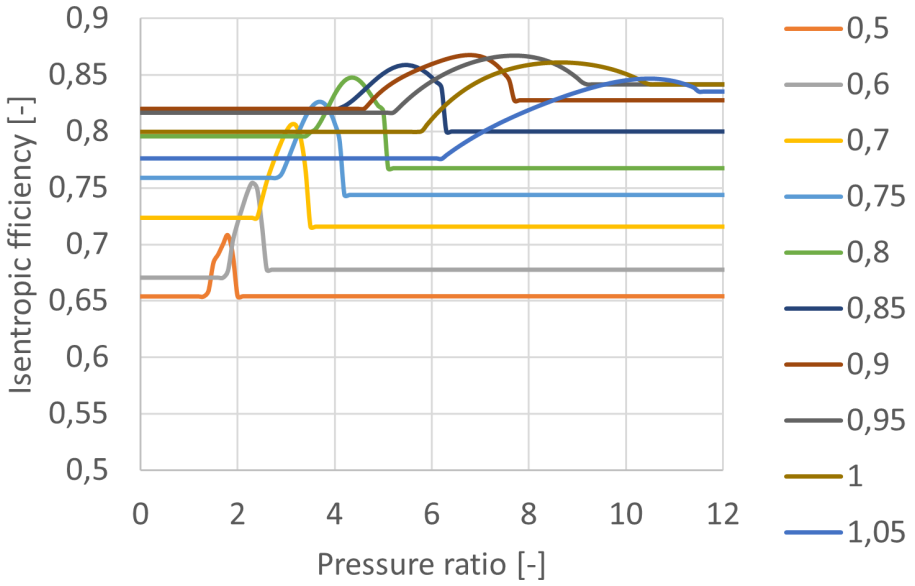

Figure 3.10: Modified compressor efficiency map

3.6 Valve

Another component required in the heat pump cycle is the expansion valve. In the TIL library, a model of an orifice valve is already included. It calculates the mass flow rate as a function of the pressure drop using the equation of Bernoulli, which is shown in Equation 3.12. The A_{eff} is the smallest constriction in the valve and can be set as time-dependent input from outside.

Later on, this will allow to dynamically control the operating point of the compressor.

$$m_{flow} = A_{eff} \cdot \sqrt{(p_{input} - p_{output}) \cdot 2 \cdot \rho_{input}} \tag{3.12}$$

3.7 Separator

Separators are often placed before the compressor in a heat pump cycle, to avoid liquid refrigerant entering the compressor [65]. This works for wet refrigerants with a negative slope in the Ts diagram (Figure 2.6), since the superheat increases during compression. However, for isentropic or dry-fluids, a certain superheat is required before the compression to avoid condensation during the compression itself. Since R-1233zd(E) is an isentropic refrigerant it always requires superheated vapour at the inlet of the compressor. In the situation where superheated vapour passes through the separator, the liquid present in the separator will start evaporating, until the filling level has decreased to zero. When the filling level of the evaporator reaches zero, it actually is not in use anymore and can be discarded.

3.8 Thermal energy storage tanks

In this research, the focus was mainly placed on the dynamic model of the heat pump. Therefore, the TES was simplified by representing the inputs and outputs of the heat pump as boundaries. In future research, these boundaries can be replaced by actual connections to a TES model to study the dynamics of the interaction between the storage tank and the heat pump.

3.9 Controls

3.9.1 Introduction

In this section, the control strategy for the heat pump model is discussed. The goal of the control is to allow fast adaptation of the compressor power according to a certain power consumption profile. During this fast control, obviously safe operation has to be maintained and condensation in the suction line of the compressor should be avoided. Moreover, the operating conditions of the compressor should be maintained within its stable operating range, close to its maximum efficiency. Finally, the water outlet temperature of the heat sink should remain close to 125 °C even when the power consumption of the compressor varies.

3.9.2 Control of compressor power

According to Meesenburg et al. [50], the best-suited control structure for fast regulation was to control the compressor power directly. As shown in Figure 3.11, the PI controller compares the power setpoint with the power consumption of the compressor and varies the rotational speed accordingly. The total gain of the controller (k) and the time constant of the integrator (T_i) were initially based on the values proposed in [50]. Afterwards, by trial and error, they have been adjusted to fit the desirable behaviour. The final values are summarized in Table 3.10.

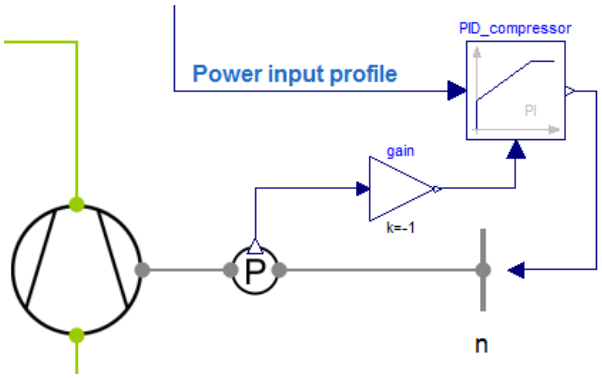

Figure 3.11: Pi control of compressor power

3.9.3 Control of valve flow area

The operating point of the cycle is determined by the intersection of the compressor and the valve characteristic. Therefore it is important to control the valve through-flow area. The desired operating point is determined by connecting the points on the compressor map with the highest efficiencies as shown by the 'Max efficiency' line in Figure 3.12. This curve was approximated by a 4th degree polynomial to obtain an optimal relation between the pressure ratio and the mass flow rate.

$$\dot{m}_{optimal} = -0.0143PR^4 + 0.3511PR^3 - 3.1371PR^2 + 14.567PR - 11.006 \tag{3.13}$$

with PR the pressure ratio measured over the compressor.

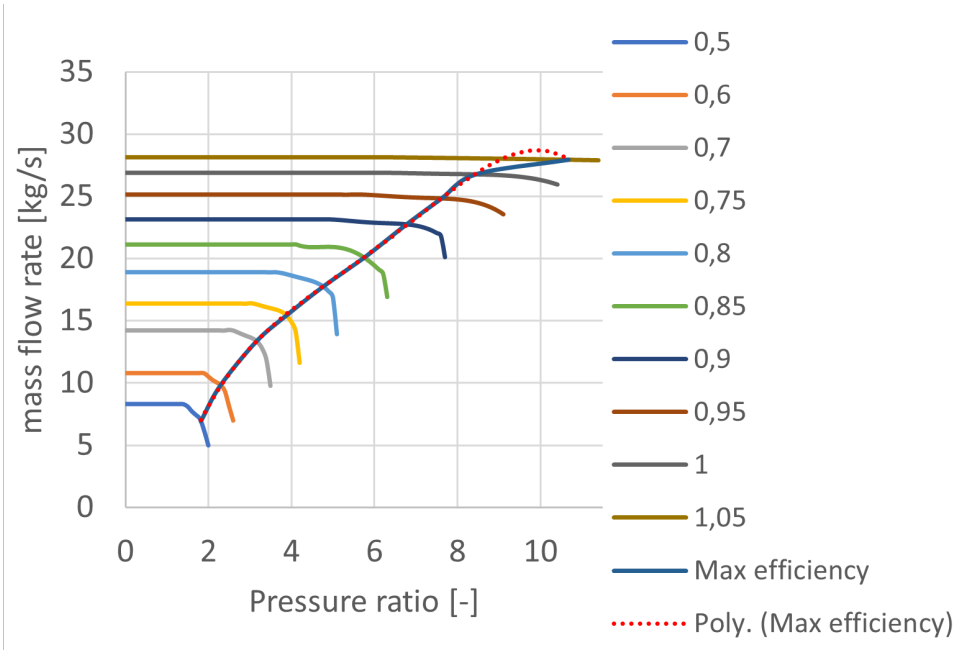

Figure 3.12: Maximum efficiency curve of the compressor

The PI-controller reads the measurement from the mass flow sensor, and receives the mass flow rate setpoint by the block 'Polynomial evaluator'. This 'polynomial evaluator' gets the measured pressure ratio over the compressor and evaluates the polynomial in Equation 3.13.

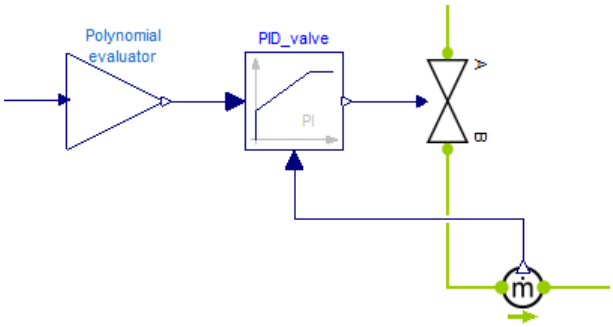

Figure 3.13: Pi control of expansion valve

Once more, the gain and the integrator time constant are based on values from [50] and adapted to fit this particular system as well as possible. The values are again summarized in Table 3.10.

To improve the understanding of the valve area control, the compressor map was plotted, in combination with the valve characteristics for different valve positions in Figure 3.14. A first observation is that the valve characteristic and the max efficiency lines are almost parallel for the larger part of the graph. Hence, the required change of area for the expansion valve will be limited. This behaviour is the result of two opposing effects that are almost balancing out. Decreasing the mass flow rate while keeping the pressure drop constant, corresponds to a restriction of the valve area, whereas a drop in pressure ratio while keeping the mass flow rate constant corresponds to an increase of the valve area. Since the intended nominal operating point is at a PR of 6.5 bar and the PR decreases when decreasing the compressor power, the valve through-flow area is expected to decrease slightly when going to part-load operation.

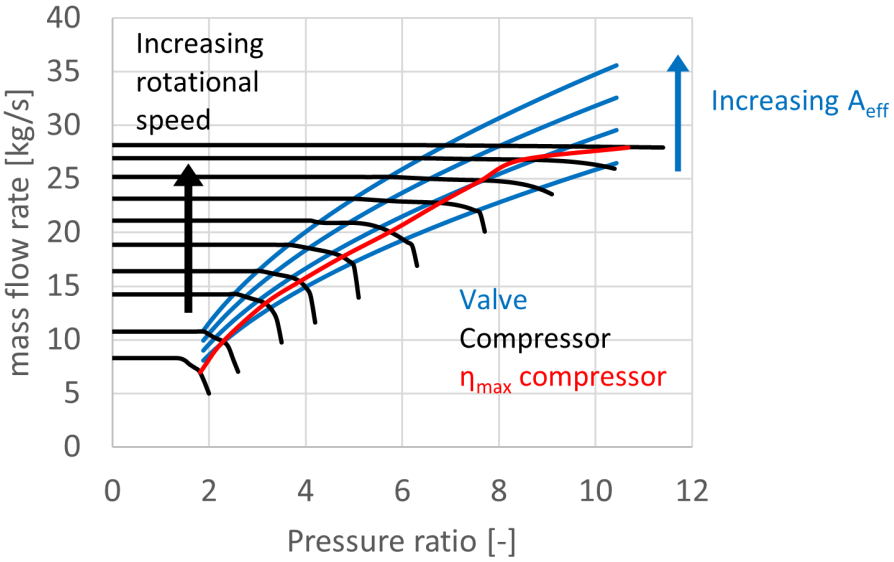

Figure 3.14: Operating curves of compressor and valve

3.9.4 Control of water outlet temperature

Finally, the temperature of the water at the outlet of the heat sink is controlled indirectly, by controlling the mass flow rate of the water. Increasing the mass flow rate decreases the temperature and vice versa. The control is shown in Figure 3.15 and consists of a controller

that receives a temperature setpoint of 125 °C and a temperature measurement. The mass flow rate of the water is then adapted accordingly. As in the previous cases, the values of the gain and the integration time constant are stated in Table 3.10.

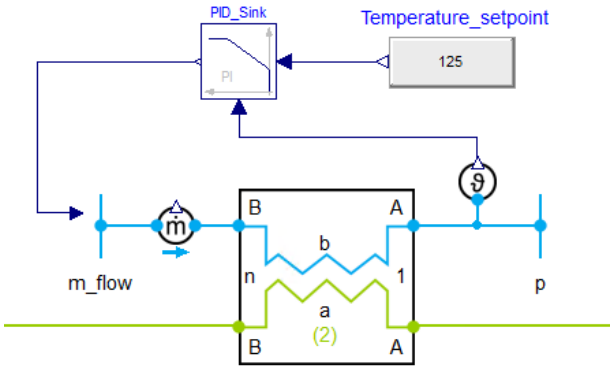

Figure 3.15: Pi control of water outlet temperature

Table 3.10: Parameters of PI-controls

	k [-]	T_i [s]
Control of compressor power	8E-06	10
Control of expansion valve	8E-05	4
Control of water mass flow rate	5	7

3.10 Sensitivity analysis

In this section, the behaviour of the system to several parameters is evaluated. More specifically the proportional constant of the PI controller of the compressor and the heat sink water pump are varied. Furthermore, the influence of the number of cells of the heat exchangers on the dynamics is studied.

Based on literature, the pumps, compressors and valves were represented as quasi-steady-state models, whereas the heat exchangers are modelled dynamically. Hence, the inertia in the system is caused by the heat exchangers. In theory the PI controls of the compressor, pump and valve can be made extremely fast by using very large proportional factors. In reality, however, this factor is limited because accelerating and decelerating a machine takes a finite period of time. Decreasing the proportional constants of the controllers of these quasi-steady-state models can possibly also decrease the maximum acceleration and deceleration encountered during these ramps. Hence, it can give an indication of the response of the system if it is equipped with a dynamic compressor model.

For the proportional constants (k), two cases are tested. In the first case, the k of the compressor controller is decreased. Whereas, in the second case, the proportional constant of the water pump in the heat sink is decreased. The imposed compressor power profile is a ramp from 1000 kW to 750 kW in 25 s. This 250 kW reduction of power corresponds to the capacity, which will be further explained in section 4.3.1.

In the first case, the proportional constant is decreased from k = 8e-6 to k = 3e-7. As can be seen in Figure 3.16, the actual ramp of the compressor is spread out over a longer period of time. The compressor takes more than 60 s to reach the set power. This is mainly caused by

the slow approach to the set power at the second half of the ramp. Decreasing the k value is clearly detrimental to the capability of following the imposed transients. Apart from that, the system still delivers hot water at the heat sink within ± 0.3 °C of its set temperature and the quality before and after the compressor never drops below one.

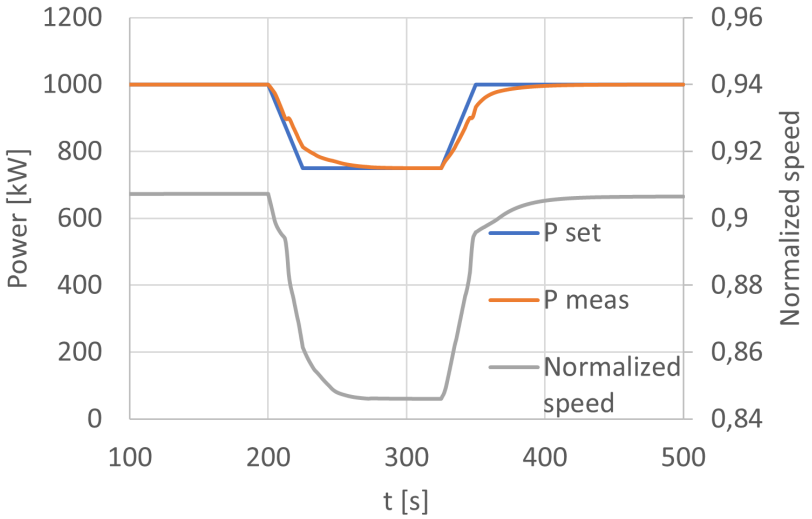

Figure 3.16: Imposed compressor power profile (*P set*), the measured compressor power (*P meas*) and the normalized speed of the compressor (*Normalized speed*) as a function of time, with a lower proportional constant $k = 3e - 7$ in the PI controller of the compressor

Secondly, the proportional constant of the water pump in the heat sink is decreased to 0.5. Similar to case one, the imposed compressor power profile is a ramp down from 1 MW to 750 kW in 25 s and a ramp up, back to 1 MW in 25 s. The response of the system is plotted in Figure 3.17. As expected, the reaction of the output is much smoother compared to case a. A smoother input signal for the pump is beneficial for the wear and tear of its components. The downside, however, is the larger deviations of the water outlet temperature in the heat sink + 2 °C and - 1.6 °C compared to the set temperature of 125 °C. Depending on the imposed limitations for the water outlet temperature, the proportional factor of the controller is restricted. Hence, indirectly, the imposed limitations for the water temperature deviations establish a requirement for the ability of the pump to quickly vary its flow rate.

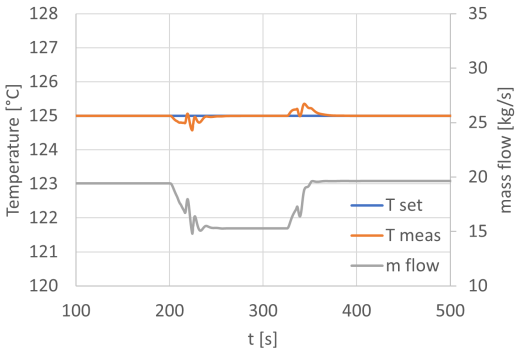

(a) Original proportional constant k = 5

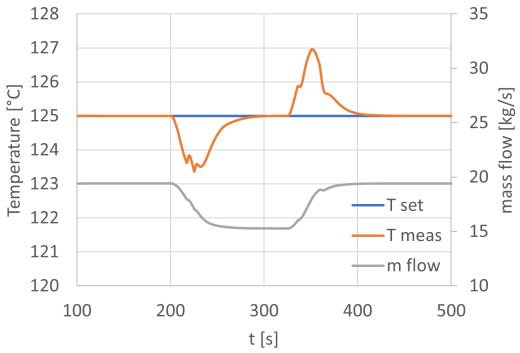

(b) Lower proportional constant k = 0.5

Figure 3.17: Evolution of the set and measured water outlet temperature of the sink ($T\ set$, $T\ meas$), as well as the controlled mass flow rate of the water ($mass\ flow$) as a function of time, for a low ($k = 0.5$) and a high ($k = 5$) value of the proportional constant in the PI controller of the pump in the heat sink

Next, the influence of the number of cells on the heat flow in the heat exchangers is looked into. Roache [101] suggests a grid convergence index (GCI), which is a measure of the percentage the computed value is away from the asymptotic numerical value. It indicates an error band on how far the solution is from the asymptotic value. The GCI is defined by Equation 3.14.

$$GCI = \frac{F_s|\epsilon|}{(r^p - 1)} \tag{3.14}$$

where F_s is the safety factor. In this calculation, 3 grid levels will be used, so a safety factor of 1.25 is recommended. r is the grid refinement ratio and is defined by Equation 3.15.

$$r = \frac{h_2}{h_1} \tag{3.15}$$

where h_1 and h_2 represent the spacing of the cells in two different grids, with h_1 being the finer (smaller) spacing. Furthermore, the order of convergence (p) can be obtained from Equation 3.16.

$$p = \frac{ln(\frac{f_3 - f_2}{f_2 - f_1})}{ln(r)} \tag{3.16}$$

with r the grid refinement ratio and f_1, f_2, f_3 the values of interest for the calculations of the GCI. With the lowest index representing the finest grid.
Also, the relative error can be calculated using Equation 3.17.

$$\epsilon = \frac{f_2 - f_1}{f_1} \tag{3.17}$$

Assessing the accuracy of the calculations requires that the grid is sufficiently refined, such that the solution is in the asymptotic range of convergence. This can be checked by observing two GCI values, computed over three grids:

$$GCI_{23} \approx r^p \cdot GCI_{12} \tag{3.18}$$

These calculations are performed for the heat flow in the evaporator in nominal conditions. The evaporator is divided into 5, 10 or 20 cells, hence the grid refinement ratio is 2. The calculations of the order of convergence yield 1.185. Finally, the values 1.95 % and 0.85% are retrieved for respectively the GCI_{23} and GCI_{12}. Performing the test in Equation 3.18 indeed suggests that

the solution is in the asymptotic range of convergence. Thus, the asymptotic numerical value is within 1.95 % of the current solution for the discretization of 10 cells and within 0.85 % for the discretization of 20 cells. For accuracy, the largest number of cells should be selected. However, increasing the number of cells from 10 to 20 in both heat exchangers, increased the calculation time of the model by a factor of 8. Therefore, 10 cells were selected for the simulations in Chapter 4 to have satisfactory accuracy while still limiting the calculation time.

3.11 Test conditions

In Chapter 4 the complete model will be tested for its performance. This includes the COP, the inertia of the components, the performance of the controls and finally the performance when imposing the test profiles to qualify the system for different types of balancing services. To test the capability of the heat pump to deliver balancing services, standardized tests are available [102–104]. The heat pump can be tested for the frequency containment reserve (FCR), the automatic frequency restoration reserve (aFRR) and the manual frequency restoration reserve.

For a pool of systems to qualify for the mFRR three types of qualification tests are available: standard, flex and standard + flex, as shown in Figures 3.18, 3.19 and 3.20. The first quarter-hour of each activation is considered as the ramp-up.

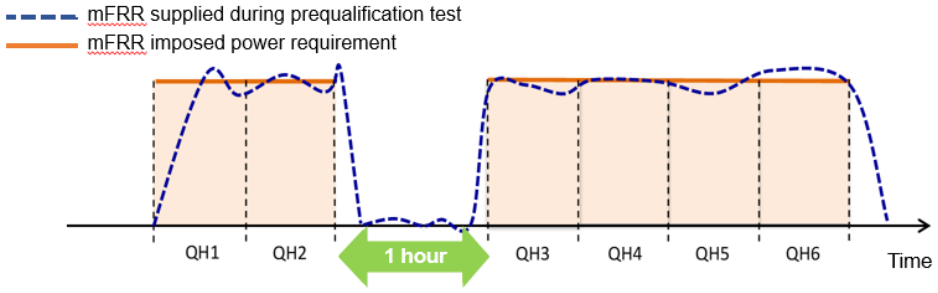

Figure 3.18: Required pattern to pre-qualify a pool for the mFRR Standard [102]

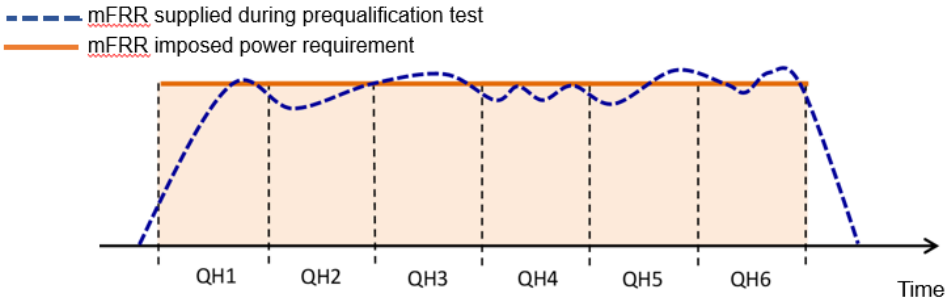

Figure 3.19: Required pattern to pre-qualify a pool for the mFRR Flex [102]

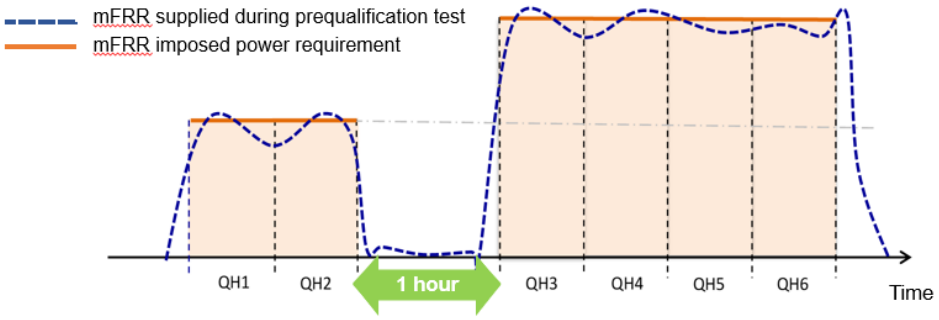

Figure 3.20: Required pattern to pre-qualify a pool for the mFRR Standard + Flex [102]

Figure 3.21 shows the prequalification profile for the aFRR with a max permitted deviation of 7.5% from the demanded aFRR power.

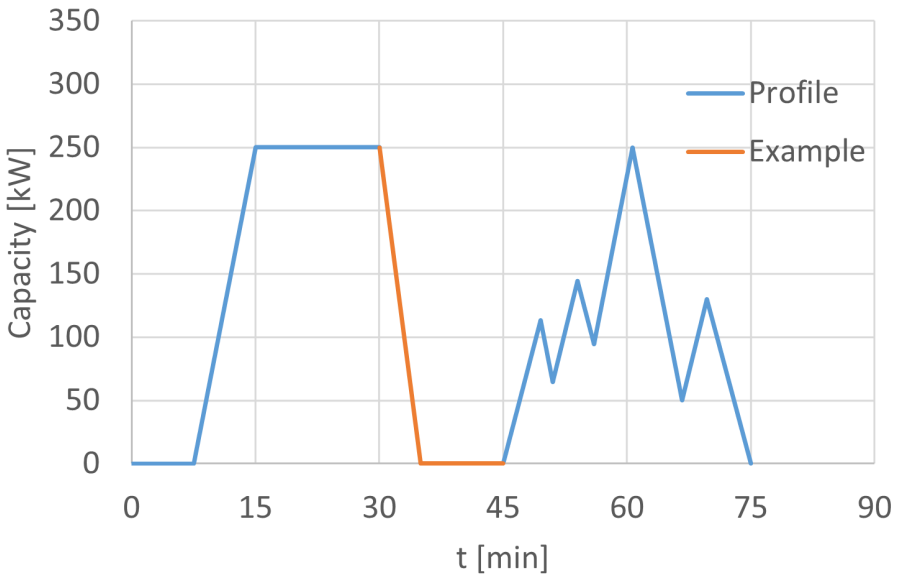

Figure 3.21: Required pattern to pre-qualify a pool for the aFRR [103]

Finally, Figure 3.22 shows the test profile for a system to qualify for the frequency containment reserve. It consists of 4 ramp-ups of 8 seconds with a 2 minute constant power in between, followed by a constant power during 22 minutes and a ramp down in 30 seconds.

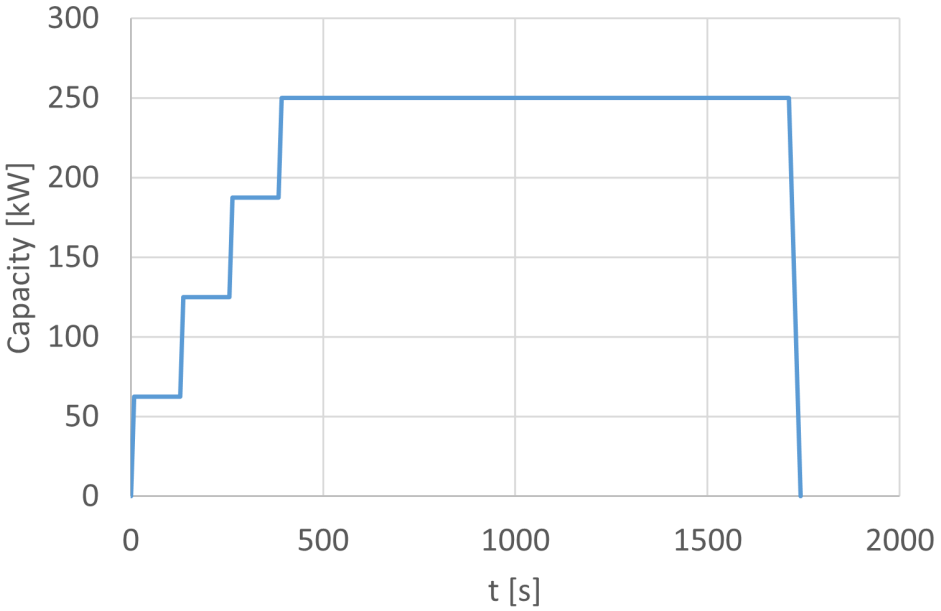

Figure 3.22: Required pattern to pre-qualify a pool for the FCR [104]

Once the dynamic model of the heat pump has been built, these test cases can be used to analyse the capability of the heat pump to deliver mFRR, aFRR or even FCR.

3.12 Simulation approach

To perform the simulations, first the system has to be intialized. The initialization requires the input of the temperatures, pressures and enthalpy in the heat exchangers. Furthermore it requires the initial mass flow rates of the refrigerant and the water in the source. Finally it also requires the initial values for the controllers (i.e. initial valve through flow area, initial compressor power and initial water mass flow rate in the sink). These values were all based on the nominal operating conditions calculated in section 3.2. Before conducting the ramping experiments, the model was simulated for 200 s before any changes were made. This ensures steady state operation before the experiments.

For this research, the steady state conditions will be on the nominal compressor power. Up-regulation will be provided by consuming less energy in the compressor. The maximum step in power uptake is the difference between the minimum and maximum achievable load. For aFRR as well as mFRR a system can qualify for upward and or downward regulation [102,103]. However, the frequency containment reserve (FCR) is a symmetric product, meaning that upward and downward capacity are procured together [105]. This study focuses on the upward regulation.

Chapter 4

Results

4.1 Introduction

In this section, the dynamic behaviour of the system will be evaluated. First of all, the heat exchanger is validated based on the heat transfer coefficients and a test with varying inputs. Next, the whole system is simulated in a steady state. Subsequently, the power is slowly ramped down to determine the maximum regulation capacity that can be delivered to the grid. Furthermore, a step is applied to understand the dynamic behaviour of the whole system and the controls. Finally, the model is tested with the prequalification profiles to evaluate the capability for delivering ancillary services.

4.2 Validation of heat exchanger model

It is concluded from Section 2.11.2 that the heat exchangers are of great importance when analysing the transient behaviour of the heat pump. Therefore the heat exchanger model is validated separately before placing it in the cycle model. First of all, the established heat transfer coefficients in the evaporator and the condenser are compared to the values available in literature. Next, the inertia is evaluated. Since the evaporator and condenser model are fairly similar, only the inertia of the evaporator is studied. Two tests are performed on the evaporator. In the first test, the heat exchanger is studied close to the nominal operating conditions. In a second test, liquid water is used on both sides of the heat exchanger to allow comparing the inertia to the available literature. Finally, the effect of the water pressure drop in the condenser is assessed.

Heat transfer coefficients

The heat transfer coefficients (HTC) of every cell in the heat exchanger can be extracted from Dymola. On the water side, the values are fairly constant along with the cells. On the refrigerant side, however, the HTC strongly depends on the quality of the refrigerant.

To improve the understanding of the HTC of the fluids along with the evaporator and condenser, two cases were looked into. One case corresponds to 100 % of the nominal compressor power, whereas the second case corresponds with part-load operation at 70 % of the nominal compressor power. In this part-load operation, the mass flow rate of the water in the sink decreases and the valve through-flow area is adapted by the controllers. The water mass flow rate in the source remains the same. The observations are discussed below.

In the nominal as well as the part-load conditions the HTC of the water in the evaporator is approximately 4700 W/(mK). In the condenser, the averaged HTC of the water in the nominal

conditions is 4640 W/(mK) and 3670 W/(mK) in the part-load conditions. The decrease in the part-load conditions is a consequence of the controller, which decreases the mass flow rate in the heat stink, to maintain a steady water outlet temperature of 125 °C.

In Figures 4.1 and 4.2, the HTC and the quality of the refrigerant is represented along the length of the evaporator and condenser. Every plot consists of two cases. One case corresponds to the nominal operating conditions, whereas the second case corresponds to part-load operation at 70 % of the nominal compressor power. In this part-load operation, the mass flow rate of the water in the sink decreases and the valve through-flow area is adapted by the controllers. The mass flow rate in the source remains the same.

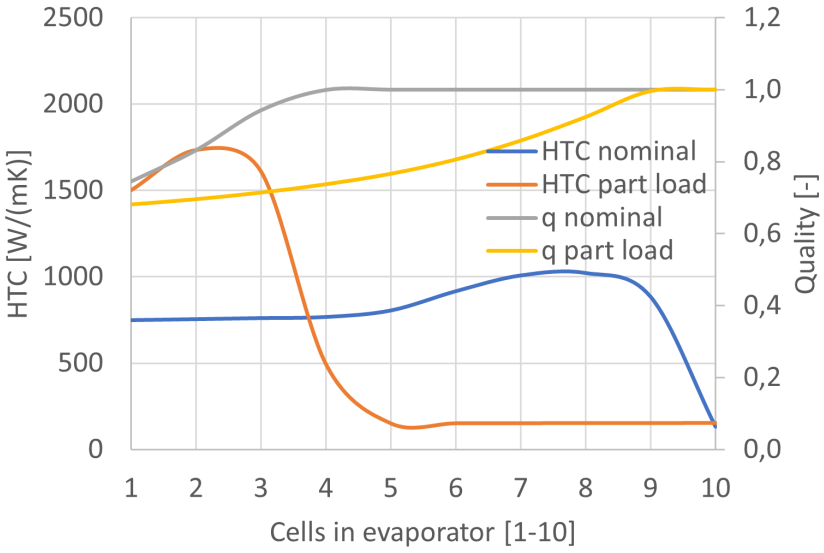

Figure 4.1: Heat transfer coefficient (HTC) and quality (q) of the refrigerant for nominal and part load conditions along the length of the evaporator

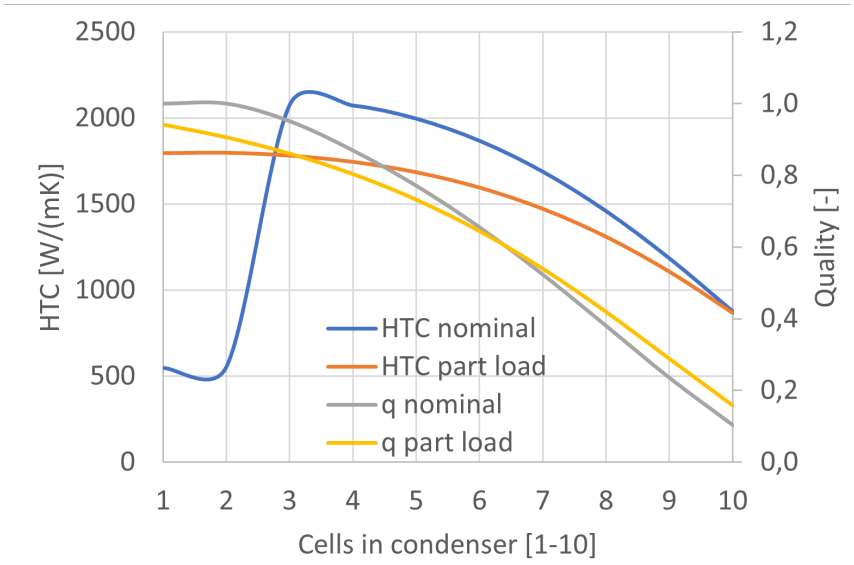

Figure 4.2: Heat transfer coefficient (HTC) and quality (q) of the refrigerant for nominal and part load conditions along the length of the condenser

From Figure 4.1 it is clear that the HTC is significantly lower in the section where q = 1, com-

pared to the section where q < 1. This can be explained by the phase change that is still in progress when the refrigerant is in the two-phase region. Figure 4.2 also shows low values of the HTC for the refrigerant with a low quality. The highest heat transfer coefficients are found for qualities in the order of 75 % to 90 %. This change in HTC is a consequence of several variables, for instance, the velocity, the heat capacity and the viscosity of the fluid.

To compare these values with literature and put things in perspective, also the velocities of the refrigerant and the water are looked into. The results are summarized in Table 4.1.

Table 4.1: Velocities and heat transfer coefficients of the evaporator and the condenser in nominal operating conditions

	Evaporator	**Condenser**
$w_{water}[m/s]$	0.09	0.12
$w_{refr,in}[m/s]$	1.87	1.23
$w_{refr,out}[m/s]$	3.11	0.26
$\alpha_{water,averaged}[W/(m^2K)]$	4769	4643
$\alpha_{refr,vapour}[W/(m^2K)]$	152	547
$\alpha_{refr,two\ phase}[W/(m^2K)]$	750 - 1750	1000 - 2100

Comparing to literature suggests that the heat transfer coefficients for water are acceptable, depending on the underlying assumptions. For water/water plate heat exchangers, AlfaLaval claims to achieve HTC of 6000-7500 W/(m²K) [106]. Based on Equation 4.1, with $\alpha_1 = \alpha_2$, $k = 7000\ W/(m^2K)$, $\delta = 0.45\ mm$, $\lambda = 16\ W/(m^2K)$ (316 stainless steel [107]), and $R_f = 0\ m^2K/W$, the HTC between the water and the wall can be calculated [106]. The obtained result is $\alpha_1 = \alpha_2$ between 14 436 and 19 010 $W/(m^2K)$, which is significantly higher than the modelled values.

$$\frac{1}{k} = \frac{1}{\alpha_1} + \frac{1}{\alpha_2} + \frac{\delta}{\lambda} + R_f \tag{4.1}$$

where k is the overall heat transfer coefficient in $W/(m^2K)$, α_1 and α_2 the HTC between respectively medium 1,2 and the surface in $W/(m^2K)$, δ the thickness of the heat transfer surface in m, λ the thermal conductivity of the wall material $W/(mK)$ and R_f the fouling factor in m^2K/W.

Based on the overall heat transfer coefficients presented in [108] ($k = 1000 - 4000\ W/(m^2K)$), a similar calculation can be performed. Once again, the same plate thickness and thermal conductivity are assumed: $\delta = 0.45\ mm$ and $\lambda = 16\ W/(m^2K)$. Putting these parameters in Equation 4.1 a heat transfer coefficient between the water and the wall of 2000 - 9000 W/(m²K) is calculated. This suggests that the $\alpha_{water,averaged}$ does fall within the expected values. In brief, the heat transfer coefficient between the water and the wall seems to be reasonable, depending on the underlying assumptions of the plate thickness, the conduction coefficient, and the velocity of the fluid.

Furthermore, the heat transfer coefficients of the refrigerant are compared to literature. According to Desideri et al. [109], the HTC of R-1233zd(E) in a plate heat exchanger is expected to be in the order of 3000 - 4500 W/(m²K). This indicates that the model in Dymola underestimates the actual values. Hence, the actual heat transfer between the refrigerant and the wall material is expected to be slightly faster than predicted by the model. Since the limits of the system's reaction time are tested, the results of the model will be on the conservative side.

Inertia

In the first test, the mass flow rates, temperatures and pressures of the water and the refrigerant are initialized on the nominal operating conditions. Since limited data is available on the dynamics of plate heat exchangers as an evaporator, also a second test was performed. This second test takes the same geometry as the evaporator but imposes a water flow on both sides of the heat exchanger. In this way, it is easier to compare the system to literature.

For the first test, the heat exchanger is initialized on the nominal operating conditions. The boundary conditions for the water are an inlet temperature of 65 °C and a water mass flow rate of 43.4 kg/s. For the refrigerant, an initial pressure of 2.93 bar, a mass flow rate of 23 kg/s and an initial enthalpy of 382 kJ/kg is imposed. During the test, a step in the mass flow rate of the refrigerant is imposed, from 23 kg/s to 19.75 kg/s. This step corresponds to the change in mass flow rate of the system when the compressor power is decreased from 1000 kW to 750 kW. In Figure 4.3 the water outlet temperature is plotted as a function of time. Next, the reaction time is defined as the time between the step and the point where the outlet temperature entered for the last time in the interval of the final temperature $\mp$ 1% of the covered temperature difference. In this case, the reaction time is about 25 s.

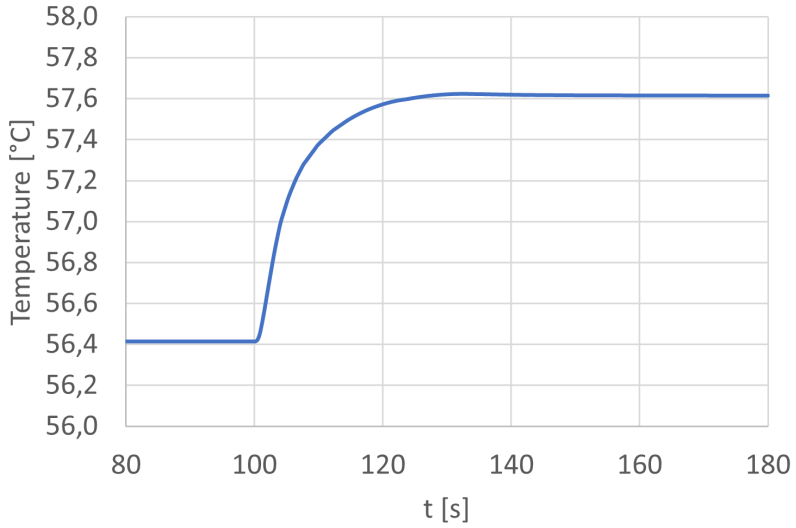

Figure 4.3: Cold water output temperature of the evaporator, with a step imposed on the enthalpy of the refrigerant at t = 100 s

In the second test, liquid water is used on both sides. Both flows have a mass flow rate of 43.4 kg/s. The hot water inlet temperature is 140 °C and is ramped down to 110 °C, whereas the cold water inlet temperature is 95 °C. The resulting temperatures are plotted in Figure 4.4. Here, the reaction time of the cold water outlet temperature and the hot water outlet temperature are respectively 56 s and 78 s. Moreover, a dead time of 6 s can be observed in the outlet temperature of the hot water.

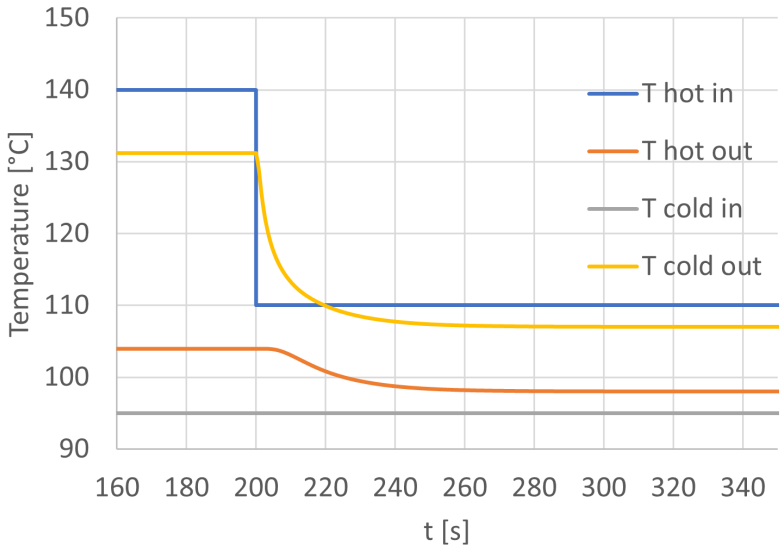

Figure 4.4: Temperature evolution of hot and cold water, with a step imposed on the hot water inlet temperature at t = 200 s

To verify this reaction time, the method of Srihari et al. [70] in section 2.11.3 can be employed. The variables are $\dot{m} = 43.3$ kg/s, a specific heat capacity $C_p = 4180$ J/kgK and the heat capacity of the resident fluid is $C = C_p \cdot V_{channels}$. Hence, the relative time constant can be calculated as follows:

$$\tau_{ra} = \frac{C}{\dot{w}_a} = \frac{C_p \cdot V_{channel} \cdot \rho_{water}}{\dot{m} \cdot C_p} = \frac{435\ kg}{43.4\ kg/s} \approx 10\ s \tag{4.2}$$

The research showed that in most test cases, the outlet temperature reached a steady state when the dimensionless time (z) reached a value of about 7. Hence, according to Equation 4.3 the expected reaction time of the model in this research is in the order of 70 s.

$$\tau = \tau_{ra} \cdot z = 10s \cdot 7 = 70\ s \tag{4.3}$$

The $\tau = 70\ s$ indeed corresponds very well to the reaction times calculated by the Dymola model. Hence, the inertia in the modelled system seems satisfactory. Furthermore, the results are also in the same order of magnitude as in the study by Dawery et al. [69].

Water pressure drop

Finally, the effect of the water pressure drop in the condenser is assessed. As mentioned in section 3.4.4, the Reynolds number of the water in the condenser is lower than 2300. This indicates that the flow is not sufficiently turbulent to use the quadratic mass flow dependence of the pressure drop. In part-load conditions, the pressure drop is lower compared to the nominal conditions. In nominal conditions the pressure drop in the model is equal to the pressure drop provided by the SWEP software, since these are input parameters for the pressure drop model. Hence, only the estimations of pressure drop lower than the nominal pressure drops are relevant to discuss. To verify the effect of inaccurate estimation of the pressure drop, two cases are compared. As a base, the condenser is initialized on its nominal operating conditions, including the pressure drop of the water. Next, the same simulation is used, with a pressure drop of 0 Pa, which is the most extreme case of an inaccurate estimation. For both cases, the temperatures, heat flows, inertia and mass flow rates are compared and no differences were noticeable. Therefore, it is safe to assume that this possibly inaccurate estimation of the pressure drop will not affect the final results of the simulation.

4.3 Heat pump model

4.3.1 Steady-state behaviour

First of all, the system is operated in steady-state conditions on the nominal operating point. The resulting pressures, temperatures and mass flow rates are presented in Figure 4.5. These values show good correspondence to the intended operating conditions defined in the model development.

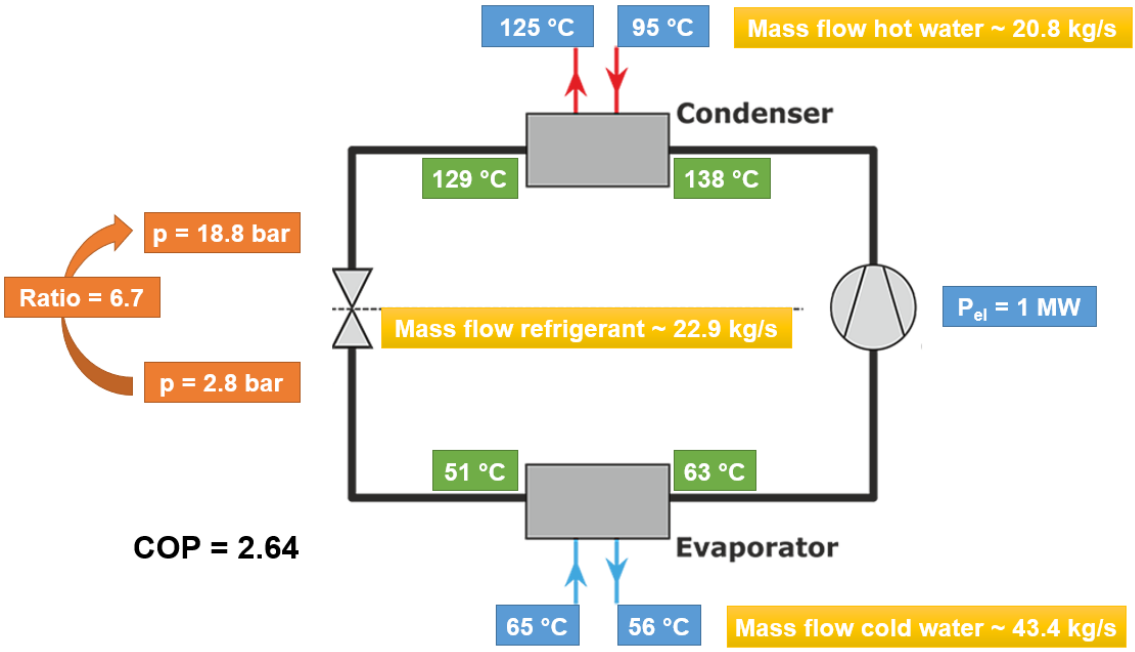

Figure 4.5: Overview of steady-state operating conditions

Next, the compressor power is decreased from 1 MW to 400 kW in order to understand how far it can be reduced before certain limitations are encountered. This ramp is performed very slowly such that it can be seen as a collection of steady-state operating points. This maximum decrease in compressor power will be called the capacity for the remainder of the research. The capacity can be limited by the operational region of the compressor (e.g. the rotational speed cannot go below 50 % of the nominal rotational speed [100]). A second limitation can be condensation before or during the compression, which can damage the compressor. Finally, the capacity can be limited if the condenser temperature decreases and the heat pump is not able to sustain a water outlet temperature to the storage tank of 125 °C.

The experiment showed once the compressor power decreased to 740 kW the quality at the outlet of the compressor became smaller than one. Hence, condensation occurred during the compression. Only when the compressor power decreased to 406 kW, the heat sink was not capable anymore of providing water at a temperature of 125 °C (with a minimum flow rate of 5 kg/s). Finally, at a compressor power of 400 kW, the rotational speed was still at 79 % of the nominal rotational speed. Hence, the rotational speed and the minimum operating power of the compressor are not the limiting factors for this system.

The limitation of the condensation during compression and the water temperature in the heat sink are inherent to the implemented control strategy. The valve controls the operating point of the compressor along the curve with the maximum efficiency, as shown in Figure 3.12. Therefore, if the compressor power and the rotational speed decrease, also the pressure ratio decreases. This

resulted in a pressure increase in the evaporator and a decrease in the condenser. The increased pressure in the evaporator also induced a higher saturation temperature. Hence, the temperature difference between the water from the source and the refrigerant was low and less heat was added. Consequently, the superheat was lower and condensation occurred in the compressor. Moreover, the decreased pressure ratio resulted in a decreased condenser pressure. Hence, also the saturation temperature in the condenser was lower. Again a lower temperature difference between the hot water and the refrigerant was established, which decreases the possible heat transfer. If this decrease in saturation pressure and temperature is continued even further, the water in the heat sink cannot be heated anymore up to 125 °C.

To increase the capacity, the valve control can be given a different operating curve where high pressure ratios are maintained for a decreasing mass flow rate. However, low mass flow rates and high pressure ratio causes the compressor to surge. One possible solution is to include the effect of inlet guide vanes, which delays the occurrence of rotating stall in compressors [110]. However, the effect of inlet guide vanes is not modelled in this research.

Finally, the COP is measured in steady-state conditions. At 100 % of the rotational speed, the COP is 2.64. Yet, the COP reaches a maximum value of 2.74 at a power of 750 kW, since this lower compressor power corresponds with a lower pressure ratio and temperature lift. This increase in COP can be related to the Carnot efficiency (Equation 4.4), which also increases with a decreasing temperature difference between the hot and the cold side.

$$COP_{heating} = \frac{T_H}{T_H - T_C} \tag{4.4}$$

4.3.2 Dynamic behaviour

The tests of the static operating conditions showed that the capacity (i.e. the maximum decrease in power, starting from the nominal 1 MW electric power) has to be limited to 250 kW in order to avoid condensation in the compressor. In the following experiments, the dynamics will be tested by imposing a power demand profile with a ramp down followed by a ramp-up. The ramp down decreases the requested power from 1 MW to 750 kW in 25 s and the ramp-up increases the power back to 1 MW in 25 s. In between the ramps, a fixed power is maintained for 100 s, to allow for the system to settle into a steady-state regime. This testing sequence will be referred to as the reference case in the remainder of this research. The goal of these experiments is to understand and evaluate the dynamic behaviour of the system. Furthermore, the limitations of the reaction speed are researched.

Throughout the following dynamic experiments, the limitation of the capacity is carefully observed. The maximum capacity of 250 kW was determined based on steady-state operating conditions. However, this limitations could behave differently in dynamic situations. Hence, the quality before and after the compressor is checked in every experiment and no condensation was observed. Therefore the maximum capacity of 250 kW is maintained for the remainder of the simulations.

Figure 4.6, presents the requested compressor power during the experiment. The graph shows an exact correspondence of the set compressor power ($P\ set$) and the measured compressor power ($P\ meas$). This exact correspondence can be explained by the quasi-steady-state model of the compressor. Since the compressor is a quasi-steady-state model, the power of the compressor changes instantly when the rotational speed is changed. Therefore no delay is present and the controller can exactly follow the requested profile.

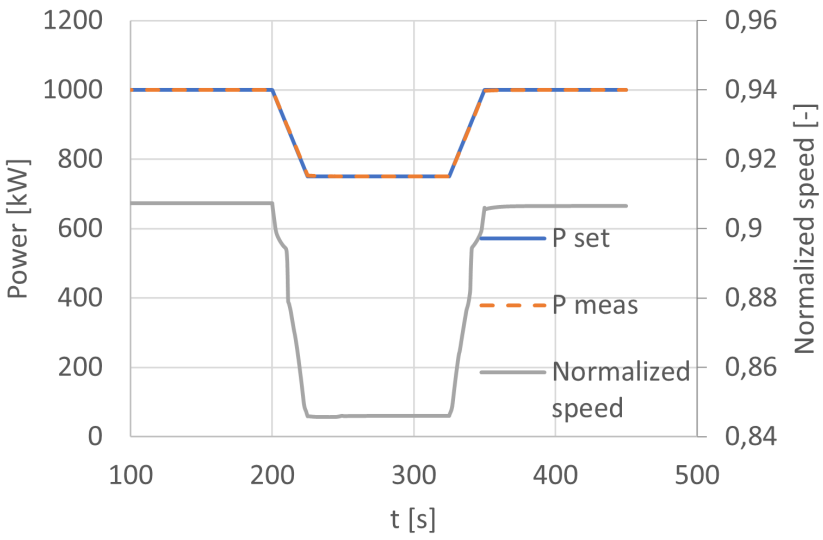

Figure 4.6: Reference case: imposed compressor power profile ($P\ set$), the measured compressor power ($P\ meas$) and the normalized speed of the compressor ($Normalizedspeed$) as a function of time

Furthermore, the input and output values of the valve controller are plotted in Figure 4.7. The controller adjusts the through-flow area of the valve in order to match the measured and the set mass flow rate of the refrigerant ($m\ flow\ set$ and $m\ flow\ meas$). Again, an almost exact match can be observed of the set and the measured mass flow. The main cause is again the steady-state model of the valve. It calculates the set mass flow rate based on the pressure ratio over the compressor. Since that pressure ratio is controlled instantaneously, also the set mass flow rate has no delay. Hence, the control of the mass flow rate is very rapid.

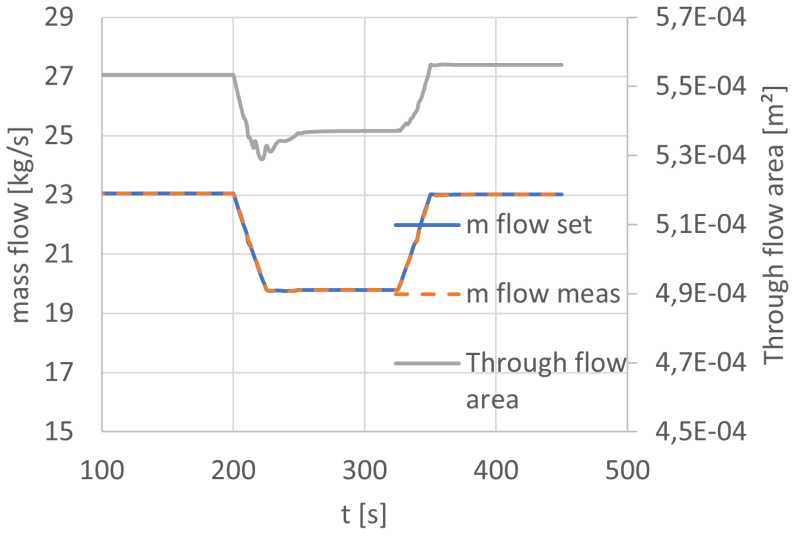

Figure 4.7: Evolution of the set and the measured mass flow rates ($m\ flow\ set$, $m\ flow\ meas$), as well as the through-flow area of the valve ($Through\ flow\ area$) as a function of time, for the reference case with 25 s ramps of the compressor power

In Figure 4.8, the variables of the PI-controller in the heat sink are represented. The water mass flow rate in the heat sink is controlled, to maintain an outlet temperature of 125 °C. During the

ramps, slight deviations can be observed in the set temperature. These deviations, however, are limited to ∓ 0.3 °C, which is acceptable.

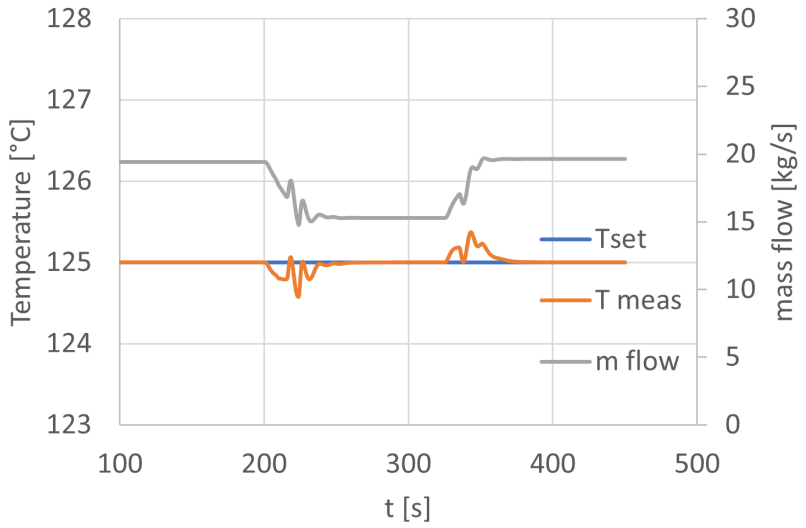

Figure 4.8: Evolution of the set and measured water outlet temperature of the sink ($T\ set$, $T\ meas$), as well as the controlled mass flow rate of the water ($m\ flow$) as a function of time, for the reference case

Next, the evolution of the pressure is represented in Figure 4.9. It shows the increase of the evaporator pressure ($p\ low$), the decrease of the condenser pressure ($p\ high$) and the corresponding decrease of the pressure ratio.

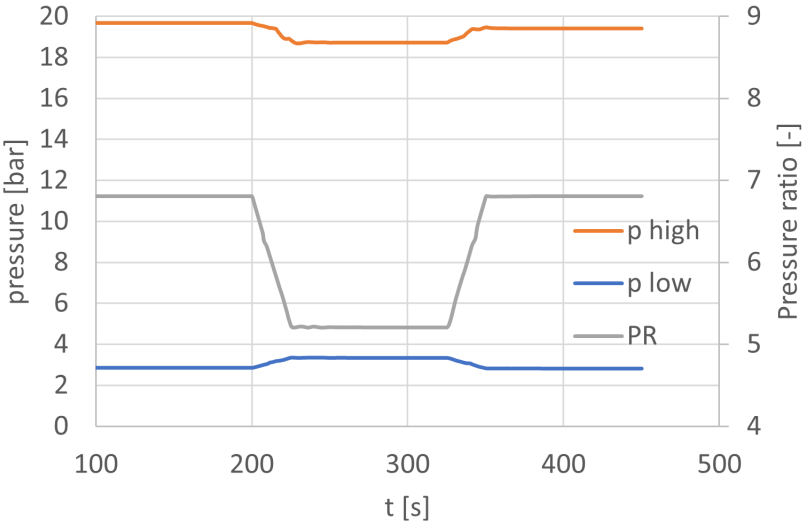

Figure 4.9: The evolution of the condenser pressure ($p\ high$), the evaporator pressure ($p\ low$) and the pressure ratio (PR) as a function of time, for the reference case with 25 s ramps of the compressor power

Finally, also the quality of the refrigerant was examined to see if condensation in the compressor would occur. The refrigerant indeed remained superheated at the inlet and outlet of the com-

pressor for the entire experiment.

Since the experiment did not reveal strong limitations in the reaction speed of the system, a new experiment was performed where the ramps only take 0.1 s instead of 25 s. This experiment showed very similar results as the experiment with the slower ramps. Again the profile of the compressor power is almost exactly followed. Also, the valve is being controlled without a significant delay. The major advantage is the water outlet temperature at the heat sink. Previously the observed deviation was limited to ∓ 0.3 °C, whereas the deviation with the faster ramp is ∓ 1 °C. These results suggest that the heat exchangers might not be the limiting factor for the dynamics in the system.

According to Meesenburg et al. [50], the maximum ramp rate of the compressor was limited by condensation. This condensation was located at the end of the evaporator or at the compressor inlet. This phenomenon was a consequence of pressure spikes in the evaporator, caused by quickly decreasing the compressor power. These pressure spikes increase the saturation temperature. Hence, if the temperature of the walls is lower than the saturation temperature, condensation can occur on these walls. To assess this risk, the saturation temperature in the evaporator was plotted, together with the wall temperature of the last cell in the evaporator. Only the last wall cell is plotted since condensation on the wall before the outlet of the evaporator would still have the time to evaporate, whereas condensation in the outlet of the evaporator is immediately be transported to the compressor. The result can be found in Figure 4.10

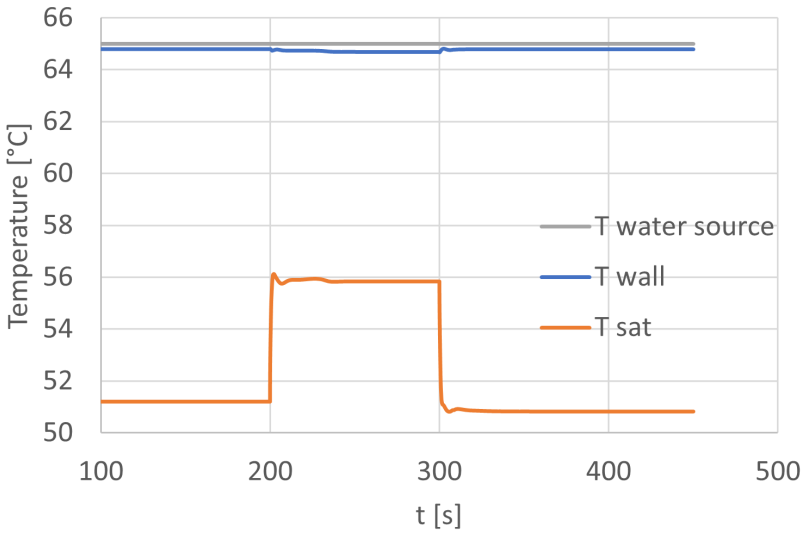

Figure 4.10: Evolution of wall and saturation temperature ($T\ wall$, $T\ sat$) as a function of time for a counter-current heat exchanger with fast compressor ramps in 0.1 s

From Figure 4.10 it is clear that no condensation occurs at the outlet of the evaporator since the wall temperature at the outlet of the refrigerant is directly located next to the inlet of the hot water (counter-current heat exchanger). Moreover, the heat transfer with the water is much higher than with the superheated vapour. As a consequence, the wall temperature at the outlet of the evaporator will always be close to the inlet water temperature of the source of 65 °C. This is a direct consequence of working with a counter-current heat exchanger. By contrast, in Meesenburg et al. [50] a co-current heat exchanger was implemented. For a co-current heat exchanger, the outlet of the refrigerant in the evaporator is not located at the inlet of the hot water from the source. Hence, this wall temperature will be lower which could indeed cause condensation on the colder walls during transients. As a matter of test, the flow rate of the

water in the evaporator was reversed to analyse the behaviour in a co-current heat exchanger. The result is plotted on Figure 4.11. Indeed, as expected, the condensation is more likely to occur. The difference between the saturation temperature and the wall temperature is significantly lower. Depending on the specific conditions (e.g. mass flow rates, the height of the ramp...) the saturation temperature could actually exceed the wall temperature.

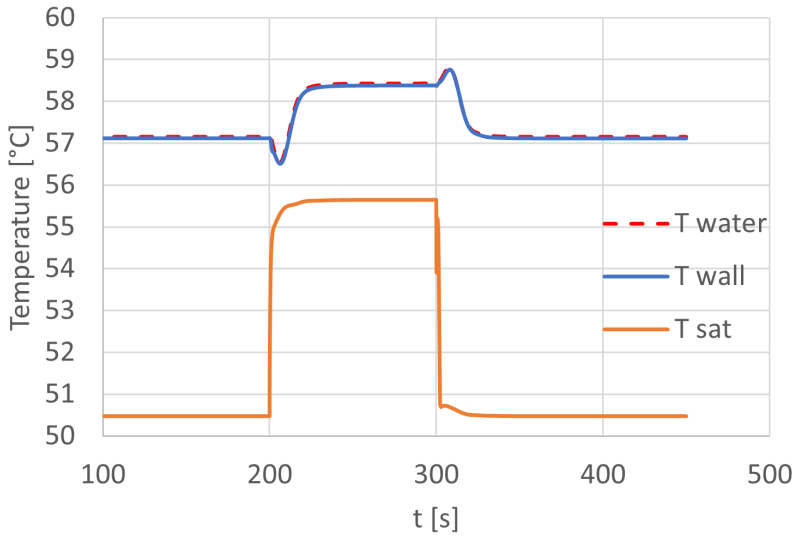

Figure 4.11: Evolution of wall and saturation temperature ($T\ wall$, $T\ sat$) as a function of time for a co-current heat exchanger with fast compressor ramps in 0.1 s

The previous experiments suggest that transients in the order of seconds are possible with this model. This gives confidence for the application of similar systems for balancing services.
As stated in literature, covering the dynamic modelling of heat pumps, the pumps compressors and valves in heat pumps typically have a lower time constant than the heat exchangers. Hence, the pumps, compressors and valves are usually represented by (quasi) steady-state models. Based on this information, all components except the heat exchangers are represented by a steady-state model in this research. However, the experiments previously discussed show that the inertia of the plate heat exchanger is rather low. Hence, the system has the potential to react to transients of the compressor power in the order of seconds. Physically, however, a finite time interval is required for these variations to manifest themselves. Compressors and pumps are physical components with a certain inertia. The acceleration and deceleration of these components can be limited by for instance the available driving power or the maximum torque applied to the axis. This inertia is not modelled in the quasi-steady-state models. Hence, this advocates for the implementation of dynamic models. These dynamic models should include the inertia of the system and the maximum acceleration/deceleration rate. Also, the addition of the thermal inertia of the compressor would be interesting, to further study the risk of condensation on the compressor walls.

4.3.3 Testing cycles

As can be expected from the previous dynamic tests, the prequalification profiles of the transmission system operator in Belgium (i.e. Elia) can be followed with great accuracy. Some of the results are plotted below. Similar to the previous tests, the capacity was limited to 250 kW in order to avoid condensation during compression. For every case the steady-state conditions are taken on the nominal compressor power of 1 MW. Up-regulation is provided by consuming less energy in the compressor. For aFRR as well as mFRR a system can qualify for upward

and/or downward regulation [102,103]. However, the frequency containment reserve (FCR) is a symmetric product, meaning that upward and downward capacity are procured together [105]. This research focuses on the upward part of the regulation.

The test results of the prequalification profile for the automatic frequency restoration reserve are shown in Figure 4.12.

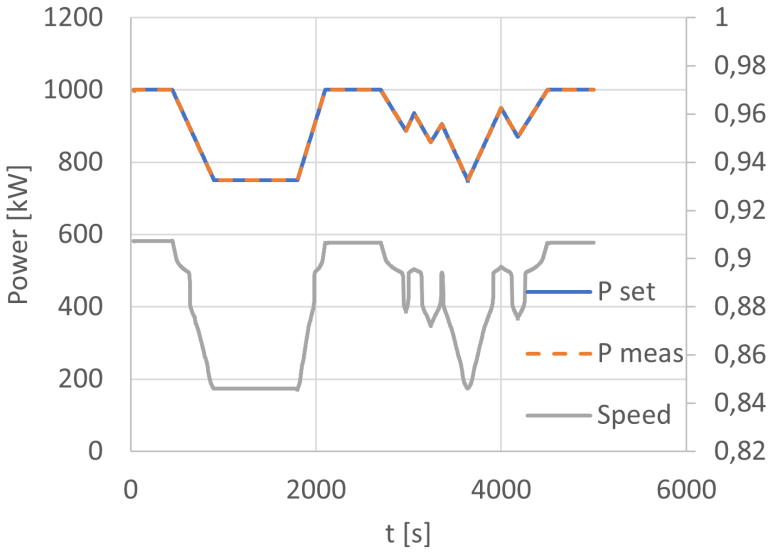

Figure 4.12: Results of the prequalification test for automatic frequency restoration reserve (aFRR), it shows the set and measured compressor power ($P\ set$, $P\ meas$) and the normalized speed as a function of time

The behaviour of the system when imposing the prequalification profile for the frequency containment reserve (FCR) is represented in Figure 4.13.

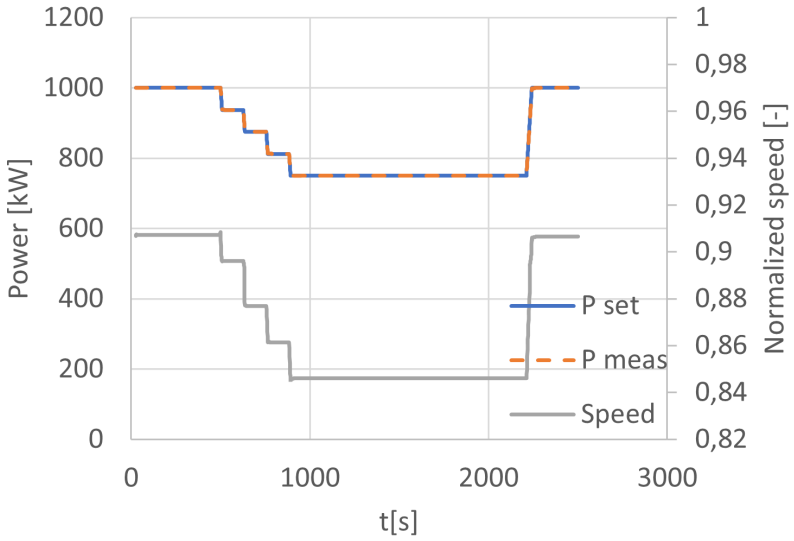

Figure 4.13: Results of the prequalification test for frequency containment reserve (FCR), it shows the set and measured compressor power ($P\ set$, $P\ meas$) and the normalized speed as a function of time

Also the response on the test profile for the manual frequency reserve was simulated. However, since this is the slowest of the three profiles it behaved as expected and perfectly followed the imposed characteristic.

Chapter 5

Conclusions

5.1 Conclusion

In this work, the transient behaviour and dynamic modelling of a high-temperature heat pump in a Carnot battery are studied. A dynamic heat pump model is developed in Dymola to achieve these objectives. A finite volume approach was used for the heat exchangers. For the evaporator and condenser, plate heat exchangers were selected for their high heat transfer coefficient and low thermal mass. The pumps and compressors on the other hand are modelled as quasi steady-state components. The compressor model is characterized by performance characteristics, representing the mass flow rate and isentropic efficiency as a function of the pressure ratio. Direct control of the compressor power was implemented to maximize the potential for fast reaction. Furthermore, control was added to the expansion valve and to the mass flow rate of the water in the heat sink.

First, the inertia and the heat transfer in the heat exchangers were studied, since literature suggests that the heat exchangers dominate the dynamic behaviour of heat pumps. The inertia and the heat transfer coefficient between the water and the wall showed satisfactory correspondence to literature. The heat transfer coefficient between the refrigerant and the wall, however, is slightly lower than expected.

Furthermore, the maximum capacity is observed to be 25 % of the nominal electrical compressor power. Hence, the electric compressor power can decrease from 1 MW down to 750 kW. The main factor limiting the capacity is the operating curve of the compressor. Since it is controlled along its maximal efficiency line, decreasing power will result in a decreasing pressure ratio. This decrease in pressure ratio also reduces the condenser temperature. Hence, the required water output temperature of 125 °C was not reached for compressor powers lower than 750 kW.

Another point of attention is the risk of condensation in the suction line of the compressor during fast load transients. However, because of the counter-flow heat exchanger and the fact that the evaporator output is always superheated, no condensation is expected.

Furthermore, a sensitivity analysis was performed on the proportional constants of the PI controller of the compressor and the heat sink water pump. Decreasing the proportional constant of the water pump increased the deviations in the water outlet temperature. For the compressor, the main influence was the prolonged reaction time, decreasing the capabilities of accurately following an imposed compressor power profile.

Finally, the main objective of this work was studied, namely the performance of heat pumps in Carnot batteries systems for grid balancing services. To study the response of the system,

prequalification profiles for different balancing services were imposed on the model. Literature suggests that heat exchangers typically have larger time constants compared to the other components in a heat pump. The experiments, however, showed that the inertia of the heat exchangers was rather low. The results in Chapter 4 even suggest that transients of the compressor power in the order of seconds are possible with this model. This gives confidence for the potential application of similar systems in balancing services. However, it also raises the question if the suggestion of literature to model the compressors and pumps as quasi-steady-state components is still valid.

From the results in Chapter 4 it is concluded that such heat pumps show great potential for delivering manual frequency restoration reserve (mFRR), automatic frequency restoration reserve (aFRR) and even the frequency containment reserve (FCR). However, important to mention is that only up-regulation has been evaluated and the current capacity is also limited to 250 kW. For actual applications the model needs up-scaling to even higher powers.

5.2 Recommendations for further research

Related to the dynamic modelling of heat pumps for balancing services, there are still some aspects which can be topics for further research.

The first key point for future research is the implementation of dynamic compressor and pump models. These dynamic models should include the inertia of the component and thus the maximum acceleration/deceleration rate. Also, the addition of the compressor's thermal inertia is interesting, to further study the risk of condensation on the compressor suction line and walls.

Secondly, much is still to learn about the dynamic interaction between the thermal energy storage and the heat pump. Moreover, the control strategy of the whole system as a balancing service provider is an interesting topic to study.

Another proposal is to implement a volumetric compressor and compare this to the current model. The advantage of the volumetric compressor is the ability to maintain a high-pressure ratio also for part-load conditions. Hence, when the power of the compressor is ramped down, the water outlet temperature in the sink (125 °C) can be maintained longer than in the case of the axial compressor. Maintaining this pressure ratio and hence the high condenser temperatures, even for lower compressor powers, would delay this constraint. As a consequence higher capacities can be achieved. Drawbacks of such volumetric compressors are the lower efficiency for screw compressors and the high maintenance and vibrations for reciprocating compressors.

Also an internal heat exchanger can be a valuable addition to the system. It recuperates part of the heat from the refrigerant at the outlet of the condenser. Comparing the coefficient of performance and the reaction time of the new system to the current system can provide interesting insights.

A final proposal is to adapt the control for the operating point of the compressor. Instead of controlling it along the maximal efficiency line, a different curve can be implemented. This curve can be tailored to aim for the lowest temperature lift (i.e. higher efficiency), while still being able to deliver the required water outlet temperature of 125 °C. However, the operational limits of the compressors (choking and surge) should be carefully observed.

Bibliography

[1] "World Energy Consumption Statistics — Enerdata." https://yearbook.enerdata.net/total-energy/world-consumption-statistics.html.

[2] European Commission, "Roadmap 2050," *Policy*, vol. 2, no. April, pp. 1–9, 2012.

[3] European Commission, "Roadmap 2050," *Policy*, vol. 1, no. April, pp. 1–9, 2012.

[4] P. Capros, M. Kannavou, S. Evangelopoulou, A. Petropoulos, P. Siskos, N. Tasios, G. Zazias, and A. DeVita, "Outlook of the EU energy system up to 2050: The case of scenarios prepared for European Commission's "clean energy for all Europeans" package using the PRIMES model," *Energy Strategy Reviews*, vol. 22, pp. 255–263, nov 2018.

[5] C. Chang, Z. Wu, H. Navarro, C. Li, G. Leng, X. Li, M. Yang, Z. Wang, and Y. Ding, "Comparative study of the transient natural convection in an underground water pit thermal storage," *Applied Energy*, vol. 208, pp. 1162–1173, dec 2017.

[6] Y. Deng, D. Sun, M. Niu, B. Yu, and R. Bian, "Performance assessment of a novel diffuser for stratified thermal energy storage tanks – The nonequal-diameter radial diffuser," 2021.

[7] L. Bird, J. Cochran, and X. Wang, "Wind and Solar Energy Curtailment: Experience and Practices in the United States," 2014.

[8] SBC Energy institute, "Electricity Storage," *Lecture Notes in Energy*, vol. 3, no. September, pp. 307–333, 2013.

[9] P. Gardner, F. Jones, M. Rowe, A. Nouri, H. van de Vegte, V. Breisig, C. Linden, and T. Pütz, "WORLD ENERGY COUNCIL World Energy Resources," 2016.

[10] P. Medina, A. W. Bizuayehu, J. P. Catalão, E. M. Rodrigues, and J. Contreras, "Electrical energy storage systems: Technologies' state-of-the-art, techno-economic benefits and applications analysis," *Proceedings of the Annual Hawaii International Conference on System Sciences*, pp. 2295–2304, 2014.

[11] International Renewable Energy Agency, *Electricity storage and renewables: Costs and markets to 2030*. No. October, 2017.

[12] J. P. Deane, B. P. Ó Gallachóir, and E. J. McKeogh, "Techno-economic review of existing and new pumped hydro energy storage plant," *Renewable and Sustainable Energy Reviews*, vol. 14, no. 4, pp. 1293–1302, 2010.

[13] E. Hossain, H. M. R. Faruque, M. S. H. Sunny, N. Mohammad, and N. Nawar, "A comprehensive review on energy storage systems: Types, comparison, current scenario, applications, barriers, and potential solutions, policies, and future prospects," *Energies*, vol. 13, no. 14, pp. 1–127, 2020.

[14] X. Luo, J. Wang, M. Dooner, and J. Clarke, "Overview of current development in electrical energy storage technologies and the application potential in power system operation," *Applied Energy*, vol. 137, pp. 511–536, 2015.

[15] H. Chen, T. N. Cong, W. Yang, C. Tan, Y. Li, and Y. Ding, "Progress in electrical energy storage system: A critical review," *Progress in Natural Science*, vol. 19, no. 3, pp. 291–312, 2009.

[16] "Crescent Dunes Solar Energy Project — Concentrating Solar Power Projects — NREL." https://solarpaces.nrel.gov/project/crescent-dunes-solar-energy-project.

[17] M. Morandin, F. Maréchal, M. Mercangöz, and F. Buchter, "Conceptual design of a thermo-electrical energy storage system based on heat integration of thermodynamic cycles - Part A: Methodology and base case," *Energy*, vol. 45, no. 1, pp. 375–385, 2012.

[18] A. Benato, "Performance and cost evaluation of an innovative Pumped Thermal Electricity Storage power system," *Energy*, vol. 138, pp. 419–436, 2017.

[19] A. Benato and A. Stoppato, "Pumped Thermal Electricity Storage: A technology overview," *Thermal Science and Engineering Progress*, vol. 6, pp. 301–315, 2018.

[20] "Balancing Services: Definition, Background & why we need it." https://www.next-kraftwerke.com/knowledge/balancing-services.

[21] Entso-e, "AN OVERVIEW OF THE EUROPEAN BALANCING MARKET AND ELECTRICITY BALANCING GUIDELINE,"

[22] "Stabilizing the grid with ancillary services." https://www.next-kraftwerke.com/knowledge/ancillary-services#frequency-control-balancing-energy.

[23] O. Dumont, G. F. Frate, A. Pillai, S. Lecompte, M. De paepe, and V. Lemort, "Carnot battery technology: A state-of-the-art review," *Journal of Energy Storage*, vol. 32, no. September, 2020.

[24] A. H. Hassan, L. O'Donoghue, V. Sánchez-Canales, J. M. Corberán, J. Payá, and H. Jockenhöfer, "Thermodynamic analysis of high-temperature pumped thermal energy storage systems: Refrigerant selection, performance and limitations," *Energy Reports*, vol. 6, pp. 147–159, dec 2020.

[25] G. F. Frate, M. Antonelli, and U. Desideri, "A novel Pumped Thermal Electricity Storage (PTES) system with thermal integration," *Applied Thermal Engineering*, vol. 121, pp. 1051–1058, jul 2017.

[26] T. Desrues, J. Ruer, P. Marty, and J. F. Fourmigué, "A thermal energy storage process for large scale electric applications," *Applied Thermal Engineering*, vol. 30, no. 5, pp. 425–432, 2010.

[27] J. Howes, "Concept and development of a pumped heat electricity storage device," *Proceedings of the IEEE*, vol. 100, no. 2, pp. 493–503, 2012.

[28] M. B. B. Michael J. Moran, Howard N. Shapiro, Daisie D. Boettner, "Principles of Engineering Thermodynamics," *Principles of Engineering Thermodynamics*, p. 867, 2015.

[29] A. White, G. Parks, and C. N. Markides, "Thermodynamic analysis of pumped thermal electricity storage," *Applied Thermal Engineering*, vol. 53, no. 2, pp. 291–298, 2013.

[30] J. D. McTigue, A. J. White, and C. N. Markides, "Parametric studies and optimisation of pumped thermal electricity storage," *Applied Energy*, vol. 137, pp. 800–811, 2015.

[31] O. Dumont and V. Lemort, "Mapping of performance of pumped thermal energy storage (Carnot battery) using waste heat recovery," *Energy*, vol. 211, p. 118963, 2020.

[32] G. F. Frate, L. Ferrari, and U. Desideri, "Multi-criteria investigation of a pumped thermal electricity storage (PTES) system with thermal integration and sensible heat storage," *Energy Conversion and Management*, vol. 208, p. 112530, mar 2020.

[33] S. Henchoz, F. Buchter, D. Favrat, M. Morandin, and M. Mercangöz, "Thermoeconomic analysis of a solar enhanced energy storage concept based on thermodynamic cycles," *Energy*, vol. 45, no. 1, pp. 358–365, 2012.

[34] "HeatStorE - 247Solar, Inc.." https://247solar.com/sustainable-solar-solutions-products/heatstore/.

[35] V. Novotny, V. Basta, P. Smola, and J. Spale, "Review of Carnot Battery Technology Commercial Development," *Energies*, vol. 15, no. 2, 2022.

[36] O. Dumont and V. Lemort, "Thermo-technical approach to characterize the performance of a reversible heat pump/organic Rankine cycle power system depending on its operational conditions," *ECOS 2019 - Proceedings of the 32nd International Conference on Efficiency, Cost, Optimization, Simulation and Environmental Impact of Energy Systems*, pp. 1863–1873, 2019.

[37] J. Dawes, "Solar Assisted Heat Pumps," *Heating and Air Conditioning Journal*, vol. 50, pp. 553–589, jan 2022.

[38] W. D. Steinmann, "The CHEST (Compressed Heat Energy STorage) concept for facility scale thermo mechanical energy storage," *Energy*, vol. 69, pp. 543–552, may 2014.

[39] A. Marina, S. Spoelstra, H. A. Zondag, and A. K. Wemmers, "An estimation of the European industrial heat pump market potential," *Renewable and Sustainable Energy Reviews*, vol. 139, p. 110545, apr 2021.

[40] C. Arpagaus, F. Bless, M. Uhlmann, J. Schiffmann, and S. S. Bertsch, "High temperature heat pumps: Market overview, state of the art, research status, refrigerants, and application potentials," *Energy*, vol. 152, pp. 985–1010, 2018.

[41] J. M. Corberán, A. H. Hassan, and J. Payá, "Thermodynamic analysis and selection of refrigerants for high-temperature heat pumps," *Refrigeration Science and Technology*, vol. 2019-August, no. August, pp. 4705–4712, 2019.

[42] G. F. Frate, L. Ferrari, and U. Desideri, "Analysis of suitability ranges of high temperature heat pump working fluids," *Applied Thermal Engineering*, vol. 150, pp. 628–640, mar 2019.

[43] "Chillers and heat pumps." https://www.sabroe.com/en/products/chillers-and-heat-pumps/.

[44] H. Jockenhöfer, W. D. Steinmann, and D. Bauer, "Detailed numerical investigation of a pumped thermal energy storage with low temperature heat integration," *Energy*, vol. 145, pp. 665–676, 2018.

[45] A. Hassan, J.-M. Corberán, and V. Sanchez, "Detailed Design of the High Temperature Heat Pump Laboratory Prototype (CHESTER, D3.2)," no. 27, 2019.

[46] M. O. M. Eric W. Lemmon, Marcia L. Huber, "NIST Standard Reference Database 23: Reference Fluid Thermodynamic and Transport Properties-REFPROP.," 2018.

[47] T. Weller, H. Jockenhöfer, M. Fiss, and D. Bauer, "Detailed design of the ORC laboratory prototype Type," no. 27, 2020.

[48] B. Eppinger, L. Zigan, J. Karl, and S. Will, "Pumped thermal energy storage with heat pump-ORC-systems : Comparison of latent and sensible thermal storages for various fluids," *Applied Energy*, vol. 280, no. October, p. 115940, 2020.

[49] G. F. Frate, L. Ferrari, and U. Desideri, "Rankine carnot batteries with the integration of thermal energy sources: A review," *Energies*, vol. 13, no. 18, 2020.

[50] W. Meesenburg, W. B. Markussen, T. Ommen, and B. Elmegaard, "Optimizing control of two-stage ammonia heat pump for fast regulation of power uptake," *Applied Energy*, vol. 271, no. December 2019, p. 115126, 2020.

[51] "Refrigeration compressor types: which is the best solution?." https://www.araner.com/blog/refrigeration-compressor-types.

[52] K. Hoopes, T. C. Allison, and R. Kurz, "Oil and gas compressor basics," *Compression Machinery for Oil and Gas*, pp. 3–11, jan 2018.

[53] D. Walraven, B. Laenen, and W. D'Haeseleer, "Comparison of shell-and-tube with plate heat exchangers for the use in low-temperature organic Rankine cycles," *Energy Conversion and Management*, vol. 87, pp. 227–237, 2014.

[54] D. Steger, C. Regensburger, B. Eppinger, S. Will, J. Karl, and E. Schlücker, "Design aspects of a reversible heat pump - Organic rankine cycle pilot plant for energy storage," *Energy*, vol. 208, oct 2020.

[55] K. Thulukkanam, *Heat Exchanger Design Handbook*. 2013.

[56] I. Sarbu and C. Sebarchievici, "A comprehensive review of thermal energy storage," *Sustainability (Switzerland)*, vol. 10, no. 1, 2018.

[57] W. D. Steinmann, D. Bauer, H. Jockenhöfer, and M. Johnson, "Pumped thermal energy storage (PTES) as smart sector-coupling technology for heat and electricity," *Energy*, vol. 183, pp. 185–190, sep 2019.

[58] D. Roskosch and B. Atakan, "Pumped heat electricity storage: Potential analysis and orc requirements," *Energy Procedia*, vol. 129, pp. 1026–1033, 2017.

[59] F. Levihn, "CHP and heat pumps to balance renewable power production: Lessons from the district heating network in Stockholm," *Energy*, vol. 137, pp. 670–678, 2017.

[60] H. Averfalk, P. Ingvarsson, U. Persson, M. Gong, and S. Werner, "Large heat pumps in Swedish district heating systems," *Renewable and Sustainable Energy Reviews*, vol. 79, no. June 2016, pp. 1275–1284, 2017.

[61] H. Averfalk, P. Ingvarsson, U. Persson, and S. Werner, "On the use of surplus electricity in district heating systems," *The 14th International Symposium on District Heating and Cooling*, pp. 7–12, 2014.

[62] A. David, B. V. Mathiesen, H. Averfalk, S. Werner, and H. Lund, "Heat Roadmap Europe: Large-scale electric heat pumps in district heating systems," *Energies*, vol. 10, no. 4, pp. 1–18, 2017.

[63] G. Carraro, S. Rech, A. Lazzaretto, G. Toniato, and P. Danieli, "Dynamic simulation and experiments of a low-cost small ORC unit for market applications," *Energy Conversion and Management*, vol. 197, no. June, p. 111863, 2019.

[64] A. T. Baheta, M. Sidahmed, S. A. Suleiman, A. D. Fentaye, and S. A. S. Ghazali, "Development and validation of a twin shaft industrial gas turbine performance model," *ARPN Journal of Engineering and Applied Sciences*, vol. 11, no. 22, pp. 13365–13371, 2016.

[65] B. Hu, Y. Li, F. Cao, and Z. Xing, "Extremum seeking control of COP optimization for air-source transcritical CO 2 heat pump water heater system," *Applied Energy*, vol. 147, pp. 361–372, 2015.

[66] "Thermodynamic simulation with TIL I TLK Energy." https://tlk-energy.de/en/software/til-suite.

[67] "Dymola and Modelica." https://tlk-energy.de/blog-en/dymola-modelica.

[68] O. Dumont, C. Carmo, F. Randaxhe, Q. Sylvain, and L. Vincent, "Simulation of a passive house coupled with a heat pump/organic Rankine cycle reversible unit," 2014.

[69] S. K. Al-Dawery, A. M. Alrahawi, and K. M. Al-Zobai, "Dynamic modeling and control of plate heat exchanger," *International Journal of Heat and Mass Transfer*, vol. 55, no. 23-24, pp. 6873–6880, 2012.

[70] N. Srihari, B. Prabhakara Rao, B. Sunden, and S. K. Das, "Transient response of plate heat exchangers considering effect of flow maldistribution," *International Journal of Heat and Mass Transfer*, vol. 48, no. 15, pp. 3231–3243, 2005.

[71] H. S. K. Aminian, L. English, D. Patchen, "Thermoacoustic liquefaction of coal mine methane to produce LNG for heavy vehicle applications,," 1999.

[72] M. Ghanim, "Dynamics of plate heat exchangers," *M.Sc. Thesis, University of Baghdad, Iraq*, 1982.

[73] F. Liu, W. Zhu, and J. Zhao, "Model-based dynamic optimal control of a CO 2 heat pump coupled with hot and cold thermal storages," *Applied Thermal Engineering*, vol. 128, pp. 1116–1125, 2018.

[74] H. Wan, Y. Hwang, S. Oh, and R. Radermacher, "A Review of Electronic Expansion Valve Correlations for Air-conditioning and Heat Pump Systems,"

[75] M. Shanwei, Z. Chuan, C. Jiangping, and C. Zhiujiu, "Experimental research on refrigerant mass flow coefficient of electronic expansion valve," *Applied Thermal Engineering*, vol. 25, no. 14-15, pp. 2351–2366, 2005.

[76] S. Wang, Y. He, H. Tuo, F. Cao, and Z. Xing, "Effect of heat transfer area and refrigerant mass flux in a gas cooler on heating performance of air-source transcritical CO2 heat pump water heater system," *Energy and Buildings*, vol. 67, pp. 1–10, 2013.

[77] H. Van De Velde, S. Lecompte, M. De Paepe, R. Tassenoy, and K. Couvreur, "Performance analysis of organic Rankine cycles in Carnot battery systems for grid balancing services," 2022.

[78] "GitHub - squoilin/NextGenerationHeatPumps: Python toolbox to model advanced heat pump concepts (high temperature heat pumps, zeotropic, transcritical, ...)." https://github.com/squoilin/NextGenerationHeatPumps.

[79] "About REFPROP — REFPROP 10.0 documentation." https://refprop-docs.readthedocs.io/en/latest/GUI/GeneralInformation/aboutrefprop.html.

[80] F. Reißner, "Development of a Novel High Temperature Heat Pump System, Entwicklung eines neuartigen Hochtemperatur-Wärmepumpensystems, PhD Thesis, Friedrich-Alexander University Erlangen-Nürnberg," pp. 1–149, 2015.

[81] "Products - SWEP." https://www.swep.net/products/.

[82] "Alfa Laval - heat transfer, separation, fluid handling." https://www.alfalaval.com/.

[83] D. Wei, X. Lu, Z. Lu, and J. Gu, "Dynamic modeling and simulation of an Organic Rankine Cycle (ORC) system for waste heat recovery," *Applied Thermal Engineering*, vol. 28, no. 10, pp. 1216–1224, 2008.

[84] A. Hernandez, A. Desideri, C. Ionescu, R. De Keyser, V. Lemort, and S. Quoilin, "Real-time optimization of organic Rankine cycle systems by extremum-seeking control," *Energies*, vol. 9, no. 5, pp. 1–18, 2016.

[85] M. Jiménez-Arreola, R. Pili, C. Wieland, and A. Romagnoli, "Analysis and comparison of dynamic behavior of heat exchangers for direct evaporation in ORC waste heat recovery applications from fluctuating sources," *Applied Energy*, vol. 216, no. January, pp. 724–740, 2018.

[86] X. Yu, Y. Huang, Z. Li, R. Huang, J. Chang, and L. Wang, "Characterization analysis of dynamic behavior of basic ORC under fluctuating heat source," *Applied Thermal Engineering*, vol. 189, no. August 2020, p. 116695, 2021.

[87] M. Kind and H. Martin, *Verein Deutscher Ingenieure (VDI) - Heat Atlas*. 2010.

[88] K. Baehr H.D., Stephan, "Wärme- und Stoffübertragung," 1996.

[89] G. C. John and R. T. John, "Convective boiling and condensation," *Oxford Engineering Science Series*, p. 644, 1994.

[90] C. C. Richter, "Proposal of New Object-Oriented Equation-Based Model Libraries for Thermodynamic Systems. PhD Thesis.," *PhD Thesis*, pp. 1–157, 2008.

[91] J. G. J. G. Collier and J. R. Thome, "Convective boiling and condensation," p. 596, 1994.

[92] M. M. Shah, "A general correlation for heat transfer during film condensation inside pipes," *International Journal of Heat and Mass Transfer*, vol. 22, no. 4, pp. 547–556, 1979.

[93] D. A. Snow, "Plant Engineer's Reference book," no. 2, pp. 26/1–26/13, 2002.

[94] A. Fioravanti, G. De Simone, A. Carpignano, A. Ruzzone, G. Mortarino, and M. Piccini, *Compressor Station Facility Failure Modes: Causes, Taxonomy and Effects*. 2020.

[95] G. Phillippi, T. Manthey, J. Sutter, B. Williams, and B. Mccain, "Your Gas Compression Application - Reciprocating, Centrifugal, or Screw?," *Proceedings of the Forty-Fifth Turbomachinery Symposium*, no. 2008, pp. 1–26, 2016.

[96] "Petrosadid: Compressor." https://www.petrosadid.com/machinery/compressor/compressor.php.

[97] C. John M., *Gas conditioning and processing*, vol. 2. 2013.

[98] "The Different Types of Compressors used in a Refrigeration System — Process Solutions, Inc.." https://processsolutions.com/the-different-types-of-compressors-used-in-a-refrigeration-system/.

[99] "CAREL - Reciprocating compressors." https://www.carel.com/reciprocating-compressors.

[100] "GasTurb - Download." https://www.gasturb.com/download.html.

[101] P. J. Roache, "Roache$_1$994.*pdf*,″ 1994.

[102] "mFRR." https://www.elia.be/nl/elektriciteitsmarkt-en-systeem/systeemdiensten/het-evenwicht-behouden/mfrr.

[103] "aFRR." https://www.elia.be/nl/elektriciteitsmarkt-en-systeem/systeemdiensten/het-evenwicht-behouden/afrr.

[104] "FCR service design note," no. April, 2019.

[105] "Frequency Containment Reserves (FCR)." https://www.entsoe.eu/network_codes/eb/fcr/.

[106] "The theory behind heat transfer - Plate heat exchangers." https://www.alfalaval.com/globalassets/documents/microsites/heating-and-cooling-hub/alfa_laval_heating_and_cooling_hub_the_theory_behind_heat_transfer.pdf.

[107] "Stainless Steel Alloy 316 Tubes — Fine Tubes." https://www.finetubes.co.uk/products/materials/stainless-steel-tubes/alloy-316-uns-s31600-wnr-14401.

[108] E. ToolBox, "Heat Exchangers - Heat Transfer Coefficients." https://www.engineeringtoolbox.com/heat-transfer-coefficients-exchangers-d_450.html, 2003.

[109] A. Desideri, J. Zhang, M. R. Kærn, T. S. Ommen, J. Wronski, V. Lemort, and F. Haglind, "An experimental analysis of flow boiling and pressure drop in a brazed plate heat exchanger for organic Rankine cycle power systems," *International Journal of Heat and Mass Transfer*, vol. 113, pp. 6–21, 2017.

[110] M. K. Khalil, K. M. Almudahka, A. M. Elzahaby, A. F. Nemnem, and N. A. Elqussas, "Enhancement Of the Surge Margin Of An Axial-Flow Fan Using Inlet Guide Vanes (IGV)," *RESEARCH JOURNAL (ERJ)*, vol. 1, no. 39, pp. 23–31, 2019.